

**WA School of Mines: Minerals, Energy and Chemical Engineering**

**Faculty of Science and Engineering**

**CO<sub>2</sub> Storage Characterization Driven by Images of a Prior  
Injection: CO2CRC's Otway Project**

**Mohammed Aldakheel**

**0000-0002-7182-0044**

**This thesis is presented for the Degree of**

**Master of Philosophy (Geophysics)**

**of**

**Curtin University**

**December 2020**

# Abstract

To optimise a geological CO<sub>2</sub> storage and ensure its safety, it is necessary to demonstrate conformance between reservoir simulations and geophysical monitoring such as Time-Lapse (TL) seismic. This process, a type of history-matching, often relies on the judgement and intuition of a reservoir modelling team because a direct examination of the multitude of plausible geological scenarios is prohibitively expensive.

To characterise geological features that control the fluid flow in the subsurface from seismic data, a multi-attribute analysis has been developed using an artificial neural network (ANN). The network is trained on the plume of CO<sub>2</sub> injected into a saline aquifer as part of the CO<sub>2</sub>CRC Otway Project, using the plume's time-lapse seismic image as ground truth.

The ANN algorithm aims to reconstruct the observed plume based on a set of seismic attribute maps. Through a randomised test, the trained model then provides an estimate of the importance of each attribute according to the attribute's contribution to the accuracy of the plume prediction. This same test is also used to identify specific geological controls for each part of the CO<sub>2</sub> plume. The developed ANN is then used to forecast a CO<sub>2</sub> plume that will likely arise from a future injection into the same formation 700 m away from the previous injection. The predicted map of the probability of the occurrence of CO<sub>2</sub> after the future injection

appears to be reasonable and agrees with existing reservoir simulations. At the same time, the neural network predicts some potential risks (e.g., across the fault migration) that have not been previously considered in the fluid flow simulations. Neural network is not a replacement for high-fidelity fluid flow simulations; however, it can highlight geological and petrophysical scenarios that should be simulated. Hence, the proposed workflow may improve significantly both efficiency and accuracy of manual history-matching.

# Acknowledgements

First, I would like to thank my family for their support and patience.

I would like to thank my supervisor Dr. Stanislav Glubokovskikh for his continuous support and guidance during my studies. He helped me in shaping my ideas in a proper scientific form.

I also would like to thank my thesis committee: Prof Boris Gurevich, Prof Andrej Bona, Prof Roman Pevzner and Dr Sinem Yavuz for their guidance and support.

I am also grateful to Saudi Aramco for giving me the opportunity to pursue my higher education.

I would like to extend my gratitude to CO2CRC for giving me permission to work on the Otway project data. The Otway Project received CO2CRC funding through its industry members and research partners, the Australian Government under the CCS Flagships Programme, the Victorian State Government, and the Global CCS Institute. The authors wish to acknowledge financial assistance provided through Australian National Low Emissions Coal Research and Development (ANLEC R\&D). ANLEC R\&D is supported by COAL21 Ltd and the Australian Government through the Clean Energy Initiative. PAWSEY supercomputing centre provided us with access to their high-performance computing facilities, which made this work possible.

# Contents

<b>Abstract.....</b>	<b>I</b>
<b>Acknowledgements .....</b>	<b>III</b>
<b>Contents .....</b>	<b>IV</b>
<b>1 List of figures.....</b>	<b>VII</b>
<b>1 Chapter 1 Introduction.....</b>	<b>1</b>
1.1 Carbon capture and storage .....	1
1.2 Seismic monitoring for CO <sub>2</sub> storage in saline aquifers .....	2
1.3 Problem statements and motivation .....	3
1.4 Objectives.....	5
1.5 Methodology .....	6
1.5.1 Phase 1: Process preparation:.....	6
1.5.2 Phase 2: Process component identification.....	6
1.5.3 Phase 3: Process optimization.....	6
1.5.4 Phase 4: Process application .....	7
<b>2 Chapter 2 CO<sub>2</sub>CRC Otway Project in-situ laboratory.....</b>	<b>9</b>
2.1 Summary of geophysical surveys conducted for the Otway Project.....	10
2.1.1 Stage 1.....	11

2.1.2	Stage 2 .....	12
2.1.3	Stage 3 .....	14
2.2	Geological controls on CO <sub>2</sub> migration .....	16
2.3	Reservoir model for Stage 2C injection .....	19
2.4	Summary .....	24
<b>3</b>	<b>Chapter 3 Data QC and seismic interpretation.....</b>	<b>26</b>
3.1	Convolutional model .....	27
3.2	Data quality .....	29
3.2.1	Seismic data .....	29
3.2.2	Well data .....	34
3.3	Seismic to well ties.....	35
3.4	Structural interpretation.....	39
3.5	Summary .....	40
<b>4</b>	<b>Chapter 4 Seismic attributes relevant for the Otway site .....</b>	<b>43</b>
4.1	Visualization techniques.....	44
4.2	Structural attributes .....	45
4.2.1	Horizon curvature .....	45
4.2.2	Fault Detect.....	47
4.2.3	Coherence attributes.....	48
4.3	Frequency-based attributes.....	53
4.3.1	Instantaneous frequency.....	53
4.3.2	Reflector isochrons.....	54
4.3.3	Spectral decomposition .....	54
4.4	Seismic amplitude .....	55
4.5	Summary .....	56
<b>5</b>	<b>Chapter 5 Neural network model building for CO<sub>2</sub> plume characterisation</b>	<b>57</b>

5.1	Artificial Neural Network .....	58
5.2	Ground truth: the seismic image of the Stage 2C plume.....	59
5.3	Input data: a set of predictive features .....	61
5.3.1	Structural attributes .....	61
5.3.2	Amplitude-based attributes .....	63
5.3.3	Seismic frequency-based attributes.....	63
5.3.4	Non-seismic attributes .....	64
5.3.5	Input data selection .....	66
5.4	The architecture of the prediction algorithm.....	68
5.5	Summary .....	70
<b>6</b>	<b>Chapter 6 Artificial Neural Network model analysis and application.....</b>	<b>72</b>
6.1	Information value of the attributes .....	72
6.1.1	Leave-one-out .....	73
6.1.2	Permutation test .....	73
6.1.3	Input data categories .....	74
6.1.4	Capturing the CO <sub>2</sub> migration process .....	75
6.1.5	ANN model implications and geological interpretation .....	80
6.2	Application to reservoir simulations .....	80
6.3	Summary .....	82
<b>7</b>	<b>Chapter 7 Discussion and conclusion.....</b>	<b>84</b>
7.1	Discussion .....	84
7.2	Conclusions .....	87
<b>8</b>	<b>References.....</b>	<b>90</b>
<b>9</b>	<b>Appendix: Copyright Clearance.....</b>	<b>97</b>

# List of figures

<b>Figure 1.1</b> Pre-injection reservoir simulation prediction overlaid by the seismically imaged CO <sub>2</sub> plume. ....	5
<b>Figure 1.2</b> progression of the proposed seismic characterization workflow.....	8
<b>Figure 2.1</b> Location map of CO <sub>2</sub> CRC project (CO <sub>2</sub> CRC, 2020). ....	11
<b>Figure 2.2</b> A schematic illustration of CO <sub>2</sub> CRC Otway project stages (Courtesy to CO <sub>2</sub> CRC).....	14
<b>Figure 2.3</b> The SOV and the downhole DAS receivers intended to continuously monitor the Stage 3 injection modified after (Isaenkov et al., 2021).....	15
<b>Figure 2.4</b> A depth map of the target reservoir ( PS1) with the regionally detected faults (Dance et al., 2019). ....	17
<b>Figure 2.5</b> A geological cross-section with the main wells in this project (Glubokovskikh et al., 2016).....	18
<b>Figure 2.6</b> Sedimentological discription of a core taken from the injection interval at CRC-3 and the facies associated with each interval (Dance, 2019) .....	19
<b>Figure 2.7</b> TL seismic response to the Stage 2C CO <sub>2</sub> injection. ....	22



**Figure 2.8** Post-injection reservoir simulation prediction overlaid by the seismically imaged CO<sub>2</sub> plume reservoir after the injection..... 23

**Figure 2.9** Cross-section of the target reservoir to demonstrate the CO<sub>2</sub> migration between the injection well and an observation well (Dance et al., 2019)..... 24

**Figure 3.1** Graphical representation of the convolutional model (Simm and Bacon, 2014). ..... 27

**Figure 3.2** Base map of the available seismic vintages and wells. .... 30

**Figure 3.3** Acquisition geometry for the Stage 2C baseline survey and the Extended M5 survey (Popik et al., 2020)..... 32

**Figure 3.4** Frequency spectra of all three analysed seismic surveys. .... 33

**Figure 3.5** Seismic miss-tie analysis. .... 33

**Figure 3.6** Quality control of the well logs. .... 35

**Figure 3.7** Seismic well-tie for Nirranda 3D survey. .... 37

**Figure 3.8** Seismic well-tie for the Stage 2C baseline survey. .... 38

**Figure 3.9** Seismic well-tie for the Extended M5 survey for Stage 2C. .... 39

**Figure 3.10** Structure map of Paaratte Formation with two composite lines (a) ..... 42

**Figure 4.1** Time slice from Stage 2c baseline (a). Map (b-d) horizon slices within PS1 at different levels. .... 44

**Figure 4.2** Explanatory graph to show the different curvature values (Chopra and Marfurt, 2007)..... 45

**Figure 4.3** 3D curvatures Calculation plane to highlight the maximum and minimum curvature ( $K_{min}$  and  $K_{max}$ ) (Roberts, 2001). .... 46

**Figure 4.4** The maximum curvature attribute of PS1..... 47

**Figure 4.5** Fault Detect map calculated on PS1..... 47

**Figure 4.6** A seismic section taken from a coherence volume calculated using cross-correlation (to the left) and a time slice across the same coherence volume (to the right).....48

**Figure 4.7** Horizon slice extracted at PS1 from the Cross-correlation method to eliminate any structural footprint overlayed by the detected plume to find any correlation. ....49

**Figure 4.8** Horizon slice extracted at PS1 from the semblance method to eliminate any structural footprint overlayed by the detected plume to find any correlation. ....50

**Figure 4.9** Horizon slice extracted at PS1 from the eigenstructure method to eliminate any structural footprint overlayed by the detected plume to find any correlation. ....51

**Figure 4.10** Horizon slice extracted at PS1 from the fault likelihood method to eliminate any structural footprint overlayed by the detected plume to find any correlation. ....51

**Figure 4.11** Maps of the discontinuities in the seismic data .....52

**Figure 4.12** An instantaneous frequency map extracted at the top of PS1 overlayed by the border of the mapped CO<sub>2</sub> plume. ....53

**Figure 4.13** Isochrons thickness map from the upper the lower zero crossing of PS1 reflector (a), Seismic section across to show the thinning of the reflector. ....54

**Figure 4.14** A horizon slice across PS1 using an RGB blend volume of 40, 50, 60 Hz tuning cubes (to the left) and a horizon slice across PS1 using amplitude volume (to the right). ....55

**Figure 4.15** Amplitude maps extracted from the Stage 2C baseline seismic vintage at the top (a) and the base (b) of the injection interval (Aldakheel et al., 2021).....56

**Figure 5.1** Two-layer feed-forward Network used in this study .....59

**Figure 5.2** CO<sub>2</sub> plume shape in the last monitoring seismic survey .....61

**Figure 5.3** Relative two-way travel time (relative to the injection point at the injection well) of the top seal TWT topography..... 62

**Figure 5.4** Seismic attributes controlled by the thickness of the injection interval .. 64

**Figure 5.5** Distance from the splay fault (a) aims to compensate the seismic imaging issues..... 65

**Figure 5.6** Nine attribute maps that are used as predictive features in the neural network, which is trained to reconstruct the plume shape (Aldakheel et al., 2021). 66

**Figure 5.7** Optimisation of the neural network algorithm ..... 69

**Figure 5.8** Spatial distribution of the prediction errors by the neural network..... 70

**Figure 5.9** Distribution of the prediction error relative to the distance to the CO<sub>2</sub> plume edge (Aldakheel et al., 2021). ..... 70

**Figure 6.1** Predictive feature importance. .... 73

**Figure 6.2** Spatial error distribution for the permutation test. .... 75

**Figure 6.3** CO<sub>2</sub> reconstruction after the randomisation of the top topography. .... 76

**Figure 6.4** CO<sub>2</sub> reconstruction after the randomisation of the frequency-based attribute (PS1 reflector isochron). .... 77

**Figure 6.5** CO<sub>2</sub> reconstruction after the randomisation of the seismic amplitude at the top of the reservoir (a) and the base (b). .... 78

**Figure 6.6** CO<sub>2</sub> reconstruction after the randomisation of fault-block identifier. .... 79

**Figure 6.7** CO<sub>2</sub> reconstruction after the randomisation of the fault transmissivity attribute. .... 80

**Figure 6.8** Spatial distribution of the attribute importance. Areas, where the physics-based reservoir simulation deviate from the actual plume shape ..... 81

**Figure 6.9** Application of the trained neural network to the prediction of the plume shape in Stage 3 of the Otway Project ..... 82

1. <b>Figure 2.1</b> Location map of CO2CRC project (CO2CRC, 2020) .....	97
2. <b>Figure 2.3</b> The SOV and the downhole DAS receivers intended to continuously monitor the Stage 3 injection modified after (Isaenkov et al., 2021).....	98
3. <b>Figure 2.4</b> A depth map of the target reservoir ( PS1) with the regionally detected faults (Dance et al., 2019). .....	101
4. <b>Figure 2.5</b> A geological cross-section with the main wells in this project (Glubokovskikh et al., 2016).....	104
5. <b>Figure 2.6</b> Sedimentological discription of a core taken from the injection interval at CRC-3 and the facies associated with each interval (Dance, 2019).....	107
6. <b>Figure 2.9</b> Cross-section of the target reservoir to demonstrate the CO <sub>2</sub> migration between the injection well and an observation well (Dance et al., 2019).....	109
7. <b>Figure 3.3</b> Acquisition geometry for the Stage 2C baseline survey and the Extended M5 survey (Popik et al., 2020).....	112
8. <b>Figure 4.2</b> Explanatory graph to show the different curvature values (Chopra and Marfurt, 2007). .....	113
9. <b>Figure 4.3</b> 3D curvatures Calculation plane to highlight the maximum and minimum curvature ( $K_{min}$ and $K_{max}$ ) (Roberts, 2001). .....	114



# Chapter 1

## Introduction

### 1.1 Carbon capture and storage

As a Successful mitigation strategy for the greenhouse gas effect is crucial for Australia, as a country who is stably ranked among the world leaders in CO<sub>2</sub> emission per capita

(<http://publications.jrc.ec.europa.eu/repository/handle/JRC117610>). One of the important mitigation strategies is carbon capture and storage (CCS), which refers to a group of technologies that aim to reduce the emission of greenhouse gases to the atmosphere via geological sequestration of CO<sub>2</sub> captured at an industrial site, for example, a power plant or chemical factory. To audit and ensure the safety of a CO<sub>2</sub> storage project, and to increase its efficacy, a storage operator must monitor the injection and subsequent distribution of CO<sub>2</sub>. CO<sub>2</sub> containment monitoring aims to ensure that CO<sub>2</sub> is located within a dedicated geological formation (Wildenborg et al., 2014). Relevant techniques range from large repeat geophysical surveys at the surface to atmospheric monitoring and fluid sampling in boreholes. Another objective of a monitoring program for CO<sub>2</sub> storage is conformance monitoring, which aims to validate current reservoir models and thus ensures that a site operator can predict future behaviour of the injection (Oldenburg et al., 2016; Lumley, 2019). Geophysical techniques play an important role in the conformance monitoring because their ability to track the spatial distribution of the injected gas in 3D, away

from the injection and any monitoring wells. Many monitoring techniques are being implemented in the industry, such as seismic, gravity, and electromagnetic (Davis et al., 2019). An appropriate monitoring strategy depends on the geological properties of the storage reservoir (Chadwick et al., 2009).

### **1.2 Seismic monitoring for CO<sub>2</sub> storage in saline aquifers**

Among the types of geological formations, depleted hydrocarbon reservoirs, saline aquifers, and coal seams have the largest potential for CO<sub>2</sub> storage (Coninck et al., 2005). In the case of saline aquifers, the presence of CO<sub>2</sub> changes the stiffness and density of the reservoir rock significantly, as the supercritical CO<sub>2</sub> is much more compressible and less dense than water (Lumley, 2019; Mavko et al., 2020). Seismic reflection from any reservoir depends on the contrast in density and rock stiffness between the reservoir itself and the surrounding rocks. Also, seismic velocities, and hence travel-times, depend on the stiffness and density. Therefore, CO<sub>2</sub> can be detected by the interpretation of the difference between the seismic surveys with repeated acquisition geometry known as Time-Lapse (TL) seismic (Lumley, 2001). The simplest TL signal is the difference in the seismic amplitudes between the monitoring and baseline surveys (Lumley, 2019). A number of CO<sub>2</sub> storage projects around the world have reported confident TL difference anomalies, e.g. Sleipner, Aquistore and Decatur projects (Lumley, 2019).

Sleipner is the earliest, largest and longest-running CO<sub>2</sub> storage project in the world (Eiken, 2019). The storage reservoir is an extensive saline aquifer of the Utsira sandstone in the northern part of the North Sea (Chadwick et al., 2004), where around 17 Mtonnes of CO<sub>2</sub> were injected as of 2017 (Eiken, 2019). Among many monitoring technologies, TL seismic was by far the most effective tool, which was able to detect as low as 1 meter thick plume (Eiken, 2019). Reservoir simulations for the conformance verification revealed two essential issues for each project: (1) a very complex physics of CO<sub>2</sub> flow through the reservoir (Zhu et al., 2015) and (2) the sensitivity of the CO<sub>2</sub> plume shape to the subtle geological features that are much finer than the seismic resolution (Eiken, 2019). The latter issue caused significant uncertainty in the pre-injection predictions of the shape of the CO<sub>2</sub> plume, which is split between several thin layers at Sleipner, and each of which has a highly irregular shape. Then, the fluid flow physics affects the rate of the plume evolution, which

tends to be much faster than the pre-injection simulations. However, after a few TL seismic images of the injection, the Sleipner reservoir model provided a satisfactory agreement with the integral parameters of the observed seismic plumes (Chadwick and Noy, 2015).

Several other CCS projects e.g. Aquistore (Canada) and Ketzin (Germany) exhibit a similar issues, where conformance between the seismically observed CO<sub>2</sub> plume and the reservoir simulation model is insufficient due to the uncertain reservoir models (Lüth et al., 2015; Jiang et al., 2017). In the Decatur project (Illinois Basin, USA), this discrepancy has led to further investigation into the baseline seismic data, where several seismic attributes revealed a possible flow barrier, which is consistent with the observed seismic time-lapse image of the CO<sub>2</sub> plume. The observed barrier had not been considered in the geological model, which caused the lack of conformance. After updating the geological model with the seismic attributes observation, the conformance has greatly improved (Davis et al., 2019).

### **1.3 Problem statements and motivation**

The above examples highlight a general issue of CCS projects: calibration of the reservoir models to the shape of TL seismic anomalies (often called history-matching) is a challenging task in petroleum production (Oliver et al., 2008) and even more so for CO<sub>2</sub> storage projects (Ma et al., 2019). This discrepancy is often attributed to the uncertainty in geological models rather than the dynamic parameters in reservoir simulation models (Davis et al., 2019). The migration of supercritical CO<sub>2</sub> is usually driven by buoyancy, and hence the injected gas follows the dip of a reservoir until it reaches an impermeable barrier no matter how small it is (Bryant et al., 2006). Seismic resolution is often insufficient to accurately image or even detect those barriers: faults, porosity deterioration due to diagenetic alteration of the reservoir rocks and/or lithological changes. On the other hand, time-lapse data often illuminates geological features and formation properties invisible or unquantifiable from pre-injection data only. Thus, it is important to use time-lapse data to inform the geological model, which can then be used as a reference model for the history matching process (Bauer et al., 2019; Dance et al., 2019; White, 2019). Besides the insufficient seismic resolution, history-matching suffers from high computational cost of physics-based fluid flow simulations (Ghasemi et al., 2014). Hence, the range



of geological models that can conceivably be simulated is limited. Thus, both pre-injection and history-matched reservoir simulations aim to match only some integral parameters of the plume, such as an aerial footprint or the maximum distance from an injector (Chadwick and Noy, 2015; Lüth et al., 2015).

The study area is the site of the CO<sub>2</sub>CRC Otway Project in the Australian State of Victoria, Australia's first CCS project. Stage 2 of the Project has confirmed the TL seismic can detect as low as 5,000 tonnes of supercritical CO<sub>2</sub> injected into a brine-saturated clastic formation (Pevzner et al., 2017a). Similarly, to other CO<sub>2</sub> storage projects, observed TL seismic anomalies differ significantly from the pre-injection predictions (**Figure 1.1**). The target reservoir, the Lower Paaratte Formation, is very complex, with numerous relatively small vertical and lateral baffles to the flow of the injected supercritical CO<sub>2</sub>, so quantitative interpretation of the observed TL seismic anomalies and history-matching are challenging (Dance et al., 2019). Currently, the Otway Project enters its Stage 3, where a small CO<sub>2</sub> injection into the Paaratte Formation will be monitored using a relatively sparse set of boreholes (Jenkins et al., 2017; Pevzner et al., 2020a), so interpretation of the borehole seismic data may benefit greatly from an in-depth analysis of the legacy seismic data from Stage 2C.

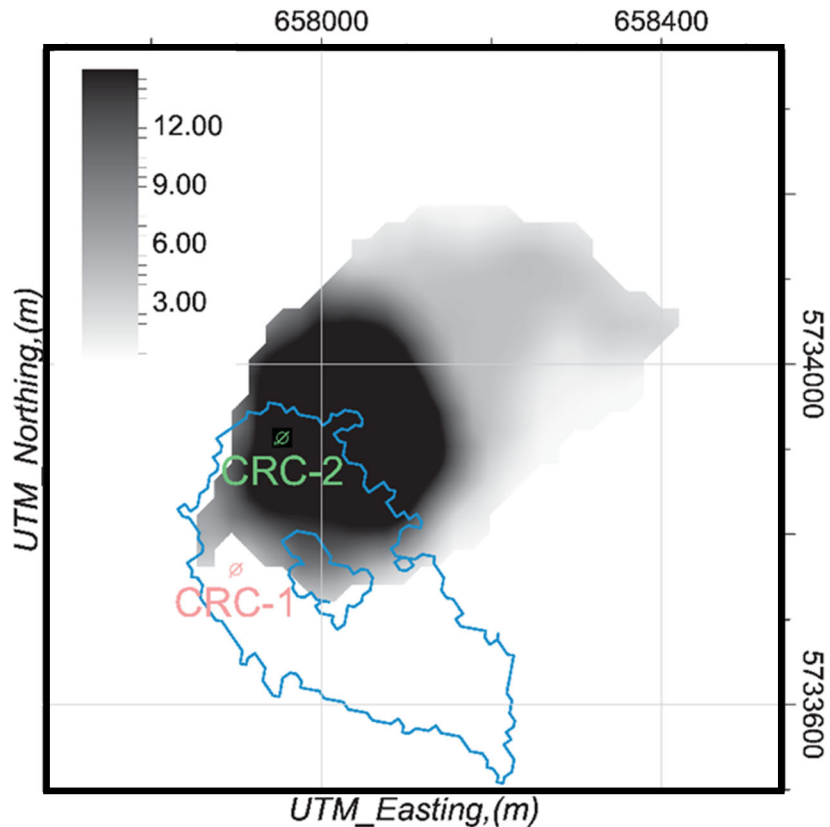


**Figure 1.1** Pre-injection reservoir simulation prediction overlaid by the seismically imaged CO<sub>2</sub> plume.

## 1.4 Objectives

The main objective of this study is to develop a seismic characterization workflow to highlight geological features (expressed quantitatively through seismic attributes measured on baseline data) which control the CO<sub>2</sub> migration process. The scarcity of well data common for many CCS projects can decrease the value of these attributes in building geological models since a comprehensive relationship between seismic attributes, and geological features may have large uncertainty. Hence, it is aimed to establish these relationships using the TL anomalies caused by the CO<sub>2</sub> injection. This method will exploit the extensive lateral coverage of the seismic data. To establish a direct link between the observed seismic plume shapes and baseline seismic attributes, an approach to the post-injection seismic characterisation is proposed to utilize a simple Artificial Neural Network (ANN). ANN is an effective tool for learning complex relationships between phenomena of diverse nature from big data sets (Goodfellow et al., 2016). This workflow can be utilized in two different ways:

1. It will highlight the controlling factors that govern the CO<sub>2</sub> migration process, which should be considered to improve the geological model.
2. It can be used as a proxy for physics-based fluid flow simulations (Schenck and Fox, 2018; Yoon, 2019).

## 1.5 Methodology

The progression of this workflow can be divided into four phases (**Figure 1.2**):

### 1.5.1 Phase 1: Process preparation:

Seismic reflections occur at lithological boundaries. The reflection strength is proportional to the contrast of seismic properties of the adjacent rock types. Hence, the distribution of the seismic amplitudes reflects the petrophysical properties of the subsurface. The quantitative interpretation of the amplitudes is ambiguous unless it is calibrated to detailed petrophysical information available in wells. At the first step, both the seismic and well data should be subjected to a quality control procedure to ensure that each geological unit observed in well data is identified in the seismic data – the process is called seismic to well tie. Once the tie is established, the clearest spatially coherent seismic events are used to map lithological boundaries and sharp discontinuities to create a structural framework used for seismic attribute extraction. This process is detailed in Chapter 3 and Chapter 4.

### 1.5.2 Phase 2: Process component identification

In this phase, we identify the components of the ANN operator: input, and output. The first component is the input; a set of attributes which potentially can capture the CO<sub>2</sub> migration process. These attributes can be divided into two categories. First, seismic attributes which represent geological features of the subsurface including topography, lithology, or porosity. The second category includes non-seismic attributes that integrate our understanding of the CO<sub>2</sub> migration process such as the distance from the injection well. The second component is the output which is the TL response due to the CO<sub>2</sub> injection. Chapter 5 has a detailed description of the creation of attributes.

### 1.5.3 Phase 3: Process optimization

After identifying the components of the ANN operator, we start the model optimization process by adjusting its parameters such as the number of neurons to

drive the error associated with the model down. To estimate the prediction error for a trained ANN, we develop a methodology that accounts for the spatial correlation of the seismic data and geological features by removing part of the data. This process is detailed in Chapter 6.

### **1.5.4 Phase 4: Process application**

Once a satisfactory estimated error is achieved, the importance of an input predictive power is evaluated by the accuracy reduction when this attribute is excluded from the input. Spatial distribution of the area with a substantial accuracy reduction provides insight into the geological features underlying the investigated attributes. ultimately, the proposed workflow can be used to refine a geological model before performing costly physics-based simulation. Moreover, the trained ANN can be used as a proxy for the fluid flow simulator to predict a stabilised CO<sub>2</sub> plume for Stage 3. This phase is described in Chapter 7.

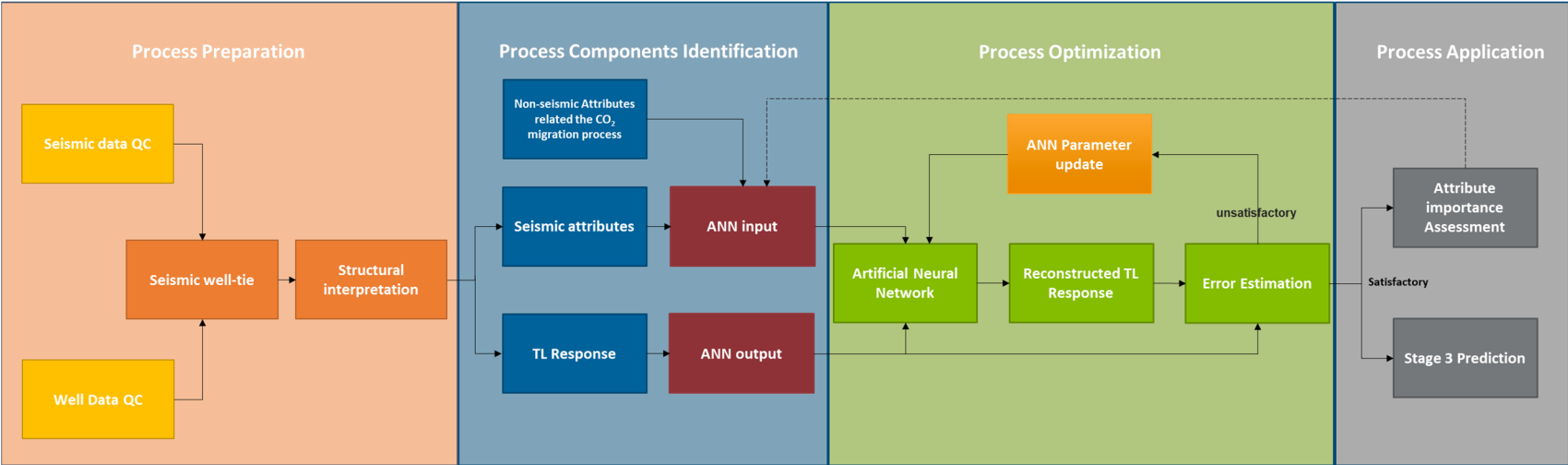


Figure 1.2 progression of the proposed seismic characterization workflow.

## **Chapter 2**

# **CO2CRC Otway Project in-situ laboratory**

As discussed in the introduction, this thesis aims to develop a seismic characterisation workflow for the Stage 2C and Stage 3 of the Otway Project, both of which involve injections of supercritical CO<sub>2</sub>-rich gas into the same saline aquifer, the Lower Paaratte Formation. This chapter describes the geological model of this highly heterogeneous clastic reservoir and identifies key geological features that control the CO<sub>2</sub> flow through the subsurface, and hence form the focus for the seismic interpretation. First, this chapter briefly summarises the stages of the Otway Project and the geological and geophysical data sets that were generated during these stages. Then, it outlines the regional sedimentological trends and large-scale geological features. Finally, the current reservoir model for the Lower Paaratte Formation is presented, which was established using the post-injection geological modelling and reservoir simulations. In addition to the facts that are related to the geology of the Lower Paaratte Formation and available seismic surveys, this chapter introduces some fundamental facts about the CO<sub>2</sub> behaviour in this saline aquifer.

## 2.1 Summary of geophysical surveys conducted for the Otway Project

The CO2CRC Otway Project is a leading Australian research initiative for testing and development of technologies for a safe and cost-effective carbon capture and storage (CCS) projects. Geophysical monitoring has always been among the main objectives of the Otway Project, as this is an important component of any CO<sub>2</sub> storage monitoring system required by Australian regulations (Sharma et al., 2009). A big advantage of the Otway Project is its in-situ laboratory – a field site located on the south-western coast of Victoria (**Figure 2.1**) in the Otway Basin. In this region, a variety of hydrocarbon gas fields have been discovered and produced, although some reservoirs turned out to be non-economical due to their high concentration of CO<sub>2</sub> (Woollands and Wong, 2001). The Otway site is situated at such a depleted gas field (Naylor Field) in a proximity of a CO<sub>2</sub>-rich accumulation penetrated by the Buttress-1 well, which provides the experimental source of CO<sub>2</sub> (Sharma et al., 2009). The original gas reservoir in the Naylor Field is the Warrre C Formation, which was produced in the 1990s and early 2000s, and ceased production in 2003 after an increase in water production due to depletion (Underschultz et al., 2011).

Past hydrocarbon exploration provided a relatively comprehensive geophysical data set that includes a large commercial 3D seismic survey and eight petroleum wells. Later, the CO<sub>2</sub> extracted from the Buttress-1 well (75% CO<sub>2</sub>, 21% CH<sub>4</sub> and 4% heavier Hydrocarbons (Jenkins et al., 2011)) was injected in supercritical form in the geological formation used for three different pilot project experiments and is scheduled to be injected again in December 2020; in the rest of the thesis the injected supercritical fluid mixture is referred to as CO<sub>2</sub> for brevity. All these stages of the Otway Project were accompanied by new subsurface characterisation efforts, which is briefly summarised in the following.

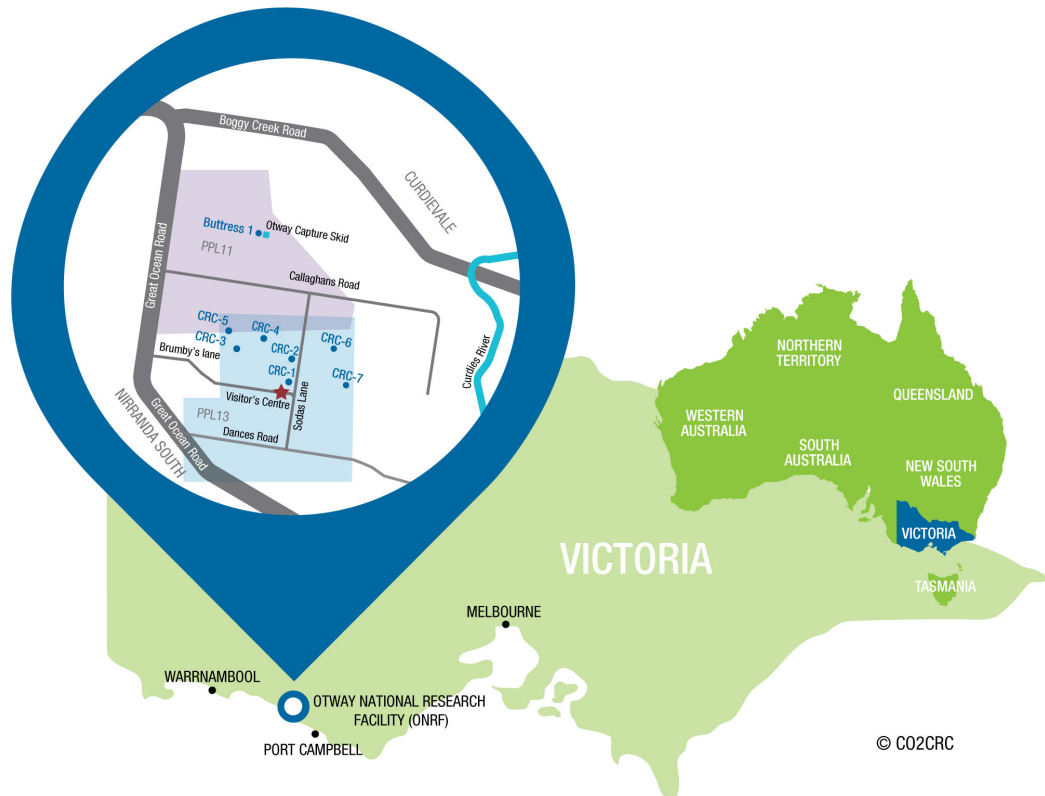


**Figure 2.1** Location map of CO2CRC project (CO2CRC, 2020).

### 2.1.1 Stage 1

Stage 1 of the Otway Project involved an injection of 66,000 tonnes of CO<sub>2</sub> into the depleted gas reservoir Warre C through a newly drilled CRC-1 well. A legacy petroleum well Naylor-1 was utilised to monitor the injection process (Cook, 2014).

The monitoring program in this stage can be divided into three components:

- Atmospheric monitoring, which aimed at detection of any abnormal concentration CO<sub>2</sub> at the site.
- Near-surface monitoring, e.g. monitoring the concentration of CO<sub>2</sub> in the freshwater aquifers.
- Geophysical monitoring of the injection interval, which involved the acquisition of TL surface and borehole seismic surveys (Sharma et al., 2009).

The TL seismic program in Stage 1 included a conventional 3D surface seismic and vertical seismic profiling (VSP): a baseline in 2007-2008 followed by two monitoring surveys after the injection, in 2009 and 2010. The TL data showed no reliable TL signal at the injection interval. The suspected TL response was at the



same level as TL noise, because the CO<sub>2</sub> injection occurred into a deep depleted gas reservoir, where the elastic properties of these gases are similar (Jenkins et al., 2011). The TL survey analysis has also suggested that there is no leakage in the overlaying aquifers, where the effect of CO<sub>2</sub> saturation would be much stronger, and hence easily detectable. This observation was confirmed by numerical seismic modelling of the TL response for a leakage of 7000 tonnes of gas with the signal-to-noise ratio (SNR) level typical for the field data in the overlaying aquifer (Cook, 2014).

### **2.1.2 Stage 2**

Stage 1 established the infrastructure for injecting CO<sub>2</sub> at the Otway site and outlined some future research directions, such as the behaviour of supercritical CO<sub>2</sub> in brine-saturated reservoirs and geophysical monitoring of the plume containment. Such focus on storage in saline aquifers is due to the higher storage capacity of such reservoirs compared to a depleted gas reservoir (Metz, 2006). Stage 2 of the Otway Project was designed to understand the trapping mechanisms in saline aquifers and benchmark the sensitivity of conventional geophysical monitoring techniques to detect a minor CO<sub>2</sub> leakage, simulated by a low-overpressure injection of 15,000 tonnes of CO<sub>2</sub> into the Lower Paaratte Formation at 1500 m depth (Cook, 2014). This stage included three parts that gradually covered all aspects of demonstrating safe injection into the saline aquifer: The Lower Paaratte Formation.

#### **2.1.2.1 Stage 2A**

The Lower Paaratte Formation is located well above the target depths for hydrocarbon exploration at the Naylor Field, and hence the formation had not been studied in detail. To fill this gap, Stage 2A involved drilling of a new appraisal well, CRC-2, that would become the injector well for the project. The well has a comprehensive data set: over 100 m of core scrutinised in petrophysical and rock physics laboratories (Lebedev et al., 2013), and a suite of advanced logs for formation evaluation and geophysical properties estimation from core samples (Dance et al., 2012).

#### **2.1.2.2 Stage 2B**

Once the rock properties and the static model of the Lower Paaratte Formation became well understood based on CRC-2 data, the focus of Stage 2 shifted towards

the CO<sub>2</sub> trapping mechanism. CO<sub>2</sub> is lighter than water. Therefore, its migration is driven by buoyancy away from the injection well. Thus, the main trapping mechanism is structural, where the gas is just surrounded by impermeable fluid flow baffles composed by either top-seal trapping structure or lateral discontinuities in geology, e.g., faults or lithological changes. In addition, a significant part of the CO<sub>2</sub> can be trapped by other mechanisms, such as residual trapping inside sufficiently thin pores and solubility trapping (the injected gas dissolved in the formation brine) (Metz, 2006). Stage 2B was designed to measure the residual and dissolution trapping capacity of the Lower Paaratte Formation along with the relative permeability of the reservoir rock. To this end, 150 tonnes of pure supercritical CO<sub>2</sub> was injected into the storage reservoir (see **Figure 2.2**) followed by the injection of 454 tonnes of formation water to displace the injected CO<sub>2</sub> away from the well. Then, an extensive downhole monitoring program provided an estimate of the residual saturation of CO<sub>2</sub> in the Lower Paaratte Formation (Paterson et al., 2013). One of the key practical outcomes of this stage was that the CO<sub>2</sub> plume injected into this interval of the Lower Paaratte Formation is likely to be very thin and moving too quickly to resemble a leakage into an overburden. Thus, the main injection was moved to a different interval within the same formation that is less permeable and more heterogeneous.

### ***2.1.2.3 Stage 2C***

Stage 2C was the final part of the Stage 2 experiment and featured injection of 15,000 tonnes of CO<sub>2</sub> into the Lower Paaratte Formation. As indicated previously, the objective of this experiment was to quantify the detection limits of the surface TL seismic to detect a minor leakage (Pevzner et al., 2017b). Stage 1 showed that the CO<sub>2</sub> remained undetected in the depleted gas reservoir, Waarre C, but the modelling suggested that 7,000 tonnes leaked into the overburden should be clearly visible. Extensive seismic modelling preceded the execution of the injection to determine both the ability of surface seismic to detect the TL signal and the optimal interval for the injection. Pevzner et al. (2013) have compared two possible injection intervals, the Stage 2B injection interval with an anticipated plume thickness of around 4 m and a lower interval with heterogeneous sandstone that is likely to form up to 15 m thick CO<sub>2</sub> plume. The study suggested that the lower and thicker column of CO<sub>2</sub> is more likely to be observed even though it produced a lower acoustic impedance

contrast as thickness appeared to be the main controlling factor in this setting (Pevzner et al., 2015).

TL surface seismic for Stage 2C consisted of six repeated surveys: a baseline in March 2015, Monitor 1 in January 2016 after injection of 5,000 tonnes, Monitor 2 in early March 2016 after injection of 10,000 tonnes, Monitor 3 in April 2016 at the end of injection, and Monitor 4 Monitor 5 after 9 and 23 months after the end of injection, respectively (Popik et al., 2020). Besides the TL surface seismic, several repeated offset VSPs and 3D VSPs were acquired concurrently with the surface acquisition. Pevzner et al. (2020b) presented a detailed summary of the seismic monitoring program. Due to the high SNR provided by the buried surface geophone array, TL seismic detected clearly as low as 5,000 tonnes of the injected CO<sub>2</sub>.

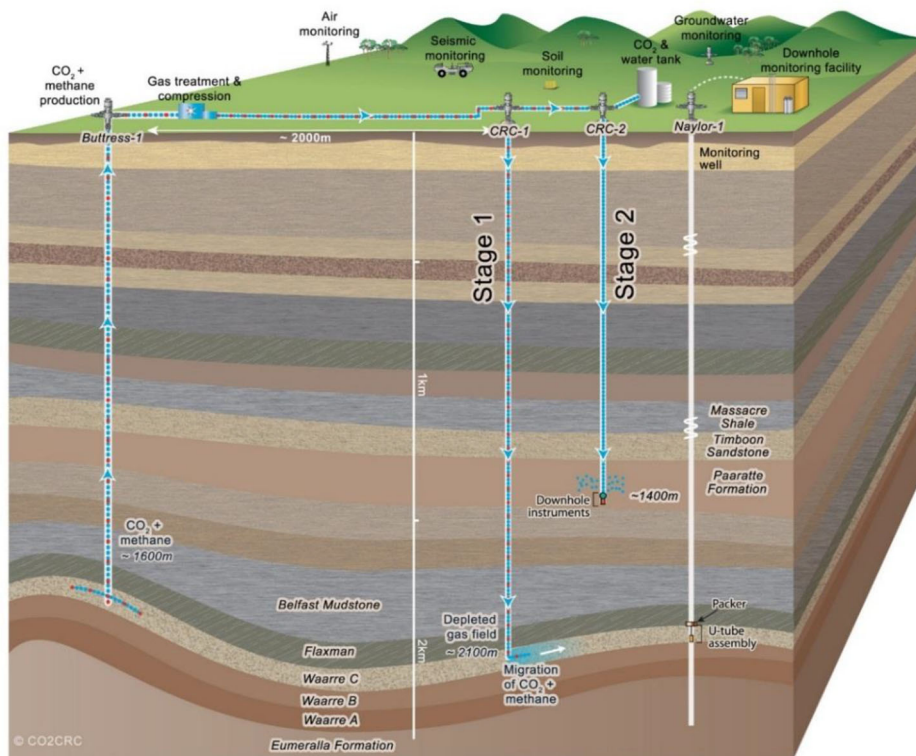


**Figure 2.2** A schematic illustration of CO2CRC Otway project stages (Courtesy to CO2CRC).

### 2.1.3 Stage 3

The success of the borehole seismic monitoring in Stage 2C was the main drive behind the design of Stage 3, which develops downhole technologies for continuous

containment monitoring of CO<sub>2</sub> storage (Jenkins et al., 2017). Unlike surface time-lapse seismic monitoring which was utilised in the previous stages, this method has a minimal disturbance to the land use, and it could be a cost-effective monitoring solution (Jenkins et al., 2018). The Stage 3 seismic monitoring program includes multi-well offset VSPs with permanently installed seismic sources - surface orbital vibrators (SOVs) - and TL multi-well 3D VSP. Since Stage 3 operates permanently installed instrumentation with limited coverage, accurate pre-injection reservoir simulations were vital for designing the monitoring array. In preparation for this project, a new well was drilled, CRC-3, that is - similarly to CRC-2 for Stage 2C – an appraisal well and injector for Stage 3 (Dance and Glubokovskikh, 2017). Bagheri et al. (2020) completed a set of de-risking reservoir simulations to determine the most probable scenario of the Stage 3 plume evolution. Only after this extensive modelling work had been completed, more monitoring wells - CRC-4, CRC-5, CRC-6 and CRC-7 - were drilled (Pevzner et al., 2020a). **Figure 2.3** shows the final configuration of the monitoring array.

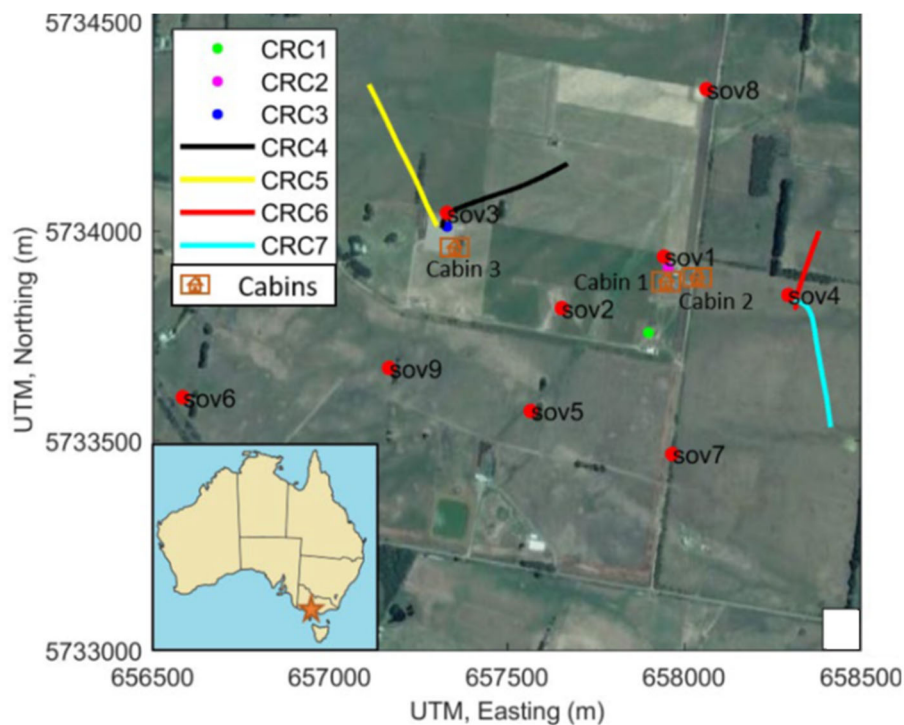


**Figure 2.3** The SOV and the downhole DAS receivers intended to continuously monitor the Stage 3 injection modified after (Isaenkov et al., 2021).

## 2.2 Geological controls on CO<sub>2</sub> migration

The Lower Paaratte Formation, the storage reservoir for Stage 2C and Stage 3, is a high-quality clastic reservoir, hence highly mobile supercritical CO<sub>2</sub> is predicted to propagate rapidly through the permeable sandstones following the dip the reservoir until a flow barrier is encountered. Hence, the plume shape in both Stage 2C and Stage 3 depends mainly on the geological understanding of the reservoir.

The Lower Paaratte Formation is of Campanian to Maastrichtian age (66-84 Ma). During that time, the Otway Basin underwent a rifting phase, which created multiple half-grabens and transfer fault zones throughout the entire basin **Figure 2.4**. The Otway site is located in one of these half-grabens between Naylor South fault to the south and Buttress and Boggy Creek faults to the north. The injection well (CRC-2) is located to the north of a small splay fault with a throw of around 15-30 m (Dance et al., 2019). CO<sub>2</sub> is expected to migrate up dip from the injection well towards the observation well (CRC-1) where it is expected to be trapped by the splay fault (Dance et al., 2019). Because buoyancy is the driving force of CO<sub>2</sub> migration (Bryant et al., 2006), it is crucial to define the geometry of the storage reservoir's top surface and any existing faults which may act as flow barriers are with the lowest error margin.

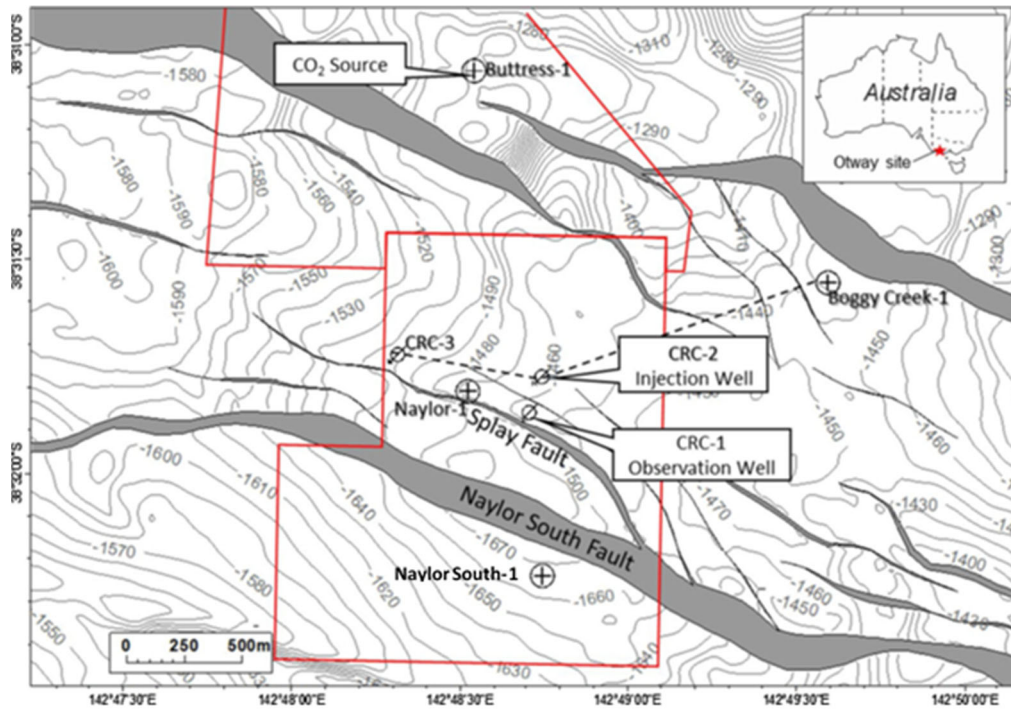


**Figure 2.4** A depth map of the target reservoir ( PS1) with the regionally detected faults (Dance et al., 2019).

Another type of a flow barrier for CO<sub>2</sub> is an abrupt lateral change in lithology when a reservoir sandstone is substituted by an impermeable facies (Dance and Glubokovskikh, 2017). General trends in lateral lithological variations are controlled by the depositional environment of the Lower Paaratte Formation along with subsequent diagenesis. The formation corresponds to a shallow marine environment overlain by a deltaic system (Krassay et al., 2004). This formation can be divided into three units A, B and C based on palynology (fossils correlation) and correlation to the major regional unconformity. These units are separated by multiple flooding surfaces (Partridge, 2011). The target reservoir in this study is unit A, which is capped by a shale zone deposited during one of the flooding cycles, which acts as the top seal **Figure 2.5**. A detailed sequence stratigraphic study conducted by Dance et al. (2012) has divided unit A into three parasequences, which, represent three transgression-regression cycles that created similar lithology.

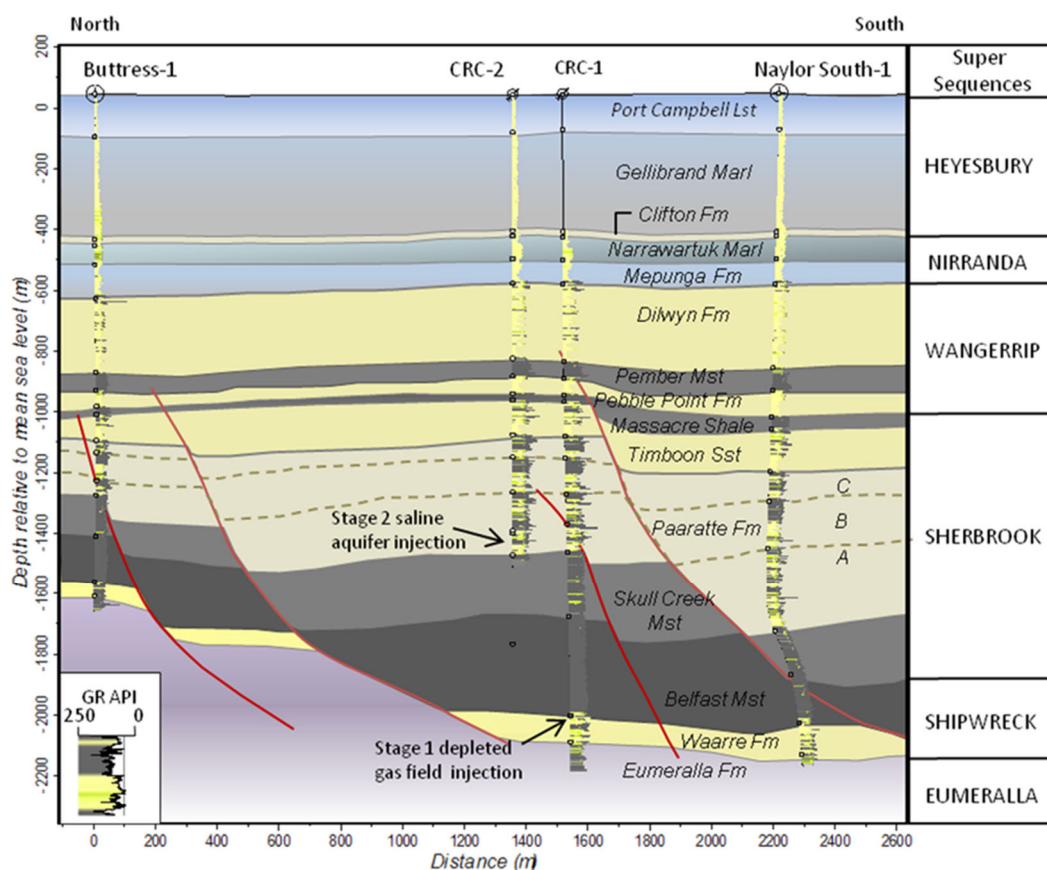


**Figure 2.5** A geological cross-section with the main wells in this project (Glubokovskikh et al., 2016).

The CO<sub>2</sub> injection for Stage 2C and Stage 3 occurs in the Lower Paaratte Formation Unit A, parasequence 1 (PS1). PS1 is a heterogeneous interval, which consists of high to medium permeability sandstone interbedded with impermeable rocks. Key lithological facies are identified in the extensive core samples extracted from CRC-2 and CRC-3 (Dance and Glubokovskikh, 2017):

- Delta Front, Distal Mouthbar: impermeable shales;
- Cements: dolomitised low-porosity impermeable sandstones; and
- Proximal Mouth bar, Distributary Channel: from clean to shaley sandstones with relatively good reservoir quality.

**Figure 2.6** presents a schematic distribution of these facies (Dance and Glubokovskikh, 2017). The distributary channels, which have high porosity and permeability, form a path for the migration of CO<sub>2</sub>, as illustrated in **Figure 2.9**. Minor faults are expected to be the main lateral boundaries for CO<sub>2</sub> migration. The sealing capacity of the faults depends on the vertical offset along a given fault: distributary channels may remain in contact at the opposite sides of a fault, and

therefore CO<sub>2</sub> may penetrate through such a fault. A probability of vertical migration of CO<sub>2</sub> along the faults is minimal (Tenthorey et al., 2014).

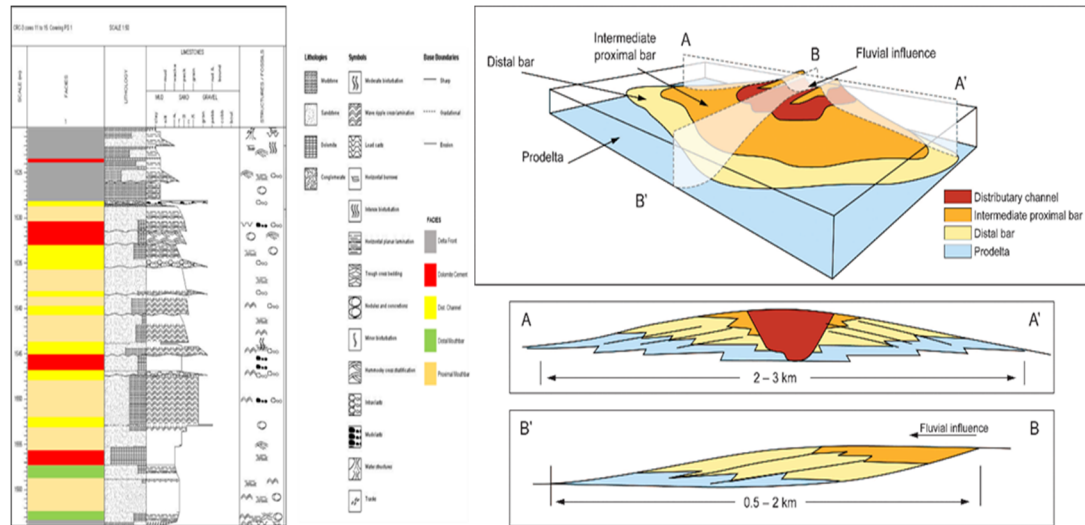


**Figure 2.6** Sedimentological description of a core taken from the injection interval at CRC-3 and the facies associated with each interval (Dance, 2019) (to the left) and the geometry of a shallow marine/delta environment Longitudinal section (AA0) and a transverse section (BB0) (to the right) (Martinius et al., 2013)

### 2.3 Reservoir model for Stage 2C injection

The previous section outlined regional geological trends and basin-scale characteristics of the Lower Paaratte Formation. This conceptual geological schema has been fully developed prior to the injection and remained almost unchanged since then. However, accurate modelling of an injection of high mobility CO<sub>2</sub> is extremely challenging for the Lower Paaratte Formation, because of its heterogeneity. Moreover, the shape of such a small injection is very sensitive to subtle variations in the reservoir properties, which would have been less important if the injection pressure and total CO<sub>2</sub> mass could overcome local fluid flow baffles. Supercritical CO<sub>2</sub> is ~30% lighter than brine, and thus the CO<sub>2</sub> migration follows the structural dip to fill in the top of the storage formation (Bryant et al., 2006). Due to its high mobility, the injected CO<sub>2</sub> filtrates through the reservoir rocks if its amount is sufficient unless the filtration hits a flow boundary: sealing faults or an abrupt change in lithology. These boundaries may be well below the seismic resolution, and hence they may only be highlighted by TL images of CO<sub>2</sub> injection. This section presents the current geological model for parasequence 1 of the Lower Paaratte Formation that was calibrated to the Stage 2C monitoring data.



The pre-injection model relied on four wells: Naylor-1, CRC-1, CRC-2 and CRC-3 (Dance et al., 2019; Glubokovskikh et al., 2020). All these wells have a comprehensive suite of well logs, in addition, CRC-2 and CRC-3 have more than fifty meters of core extracted from the target formation and examined in a rock physics laboratory (Lebedev et al., 2013; Lebedev and Mikhaltsevitch, 2017). Such a rich data set from four closely-spaced wells allowed the project to constrain the potential seismic response to changes in the properties of the reservoir rocks, such as porosity, the volume of clay and cementation. Lebedev et al. (2013) measured the elastic properties of core samples from the Lower Paaratte Formation versus pore pressure and CO<sub>2</sub> saturation. The dependence on pore pressure is sufficiently small to disregard associated effects in the TL seismic. On the other hand, the compressional velocity rapidly decreased with a small increase of CO<sub>2</sub> saturation and reached the values that are typical for fully dry rocks, values which are in full agreement with Gassmann's fluid substitution (e.g., Smith et al., 2003). Thus, it is assumed that the TL seismic signal arises only when CO<sub>2</sub> is present in pore space (Caspari et al., 2015; Pevzner et al., 2017a), and hence the observed TL anomalies can be considered as a proxy for the plume thickness maps (Glubokovskikh et al., 2020), which is referred to as the seismic plume.

The Stage 2C seismic plumes (**Figure 2.7**) contributed greatly to refinement of the geological model for the Lower Paaratte Formation. Due to the reservoir complexity and reservoir characterisation uncertainty, pre-injection reservoir simulations differ significantly from the observed plumes (**Figure 1.1**). Dance et al. (2019) performed a thorough post-injection analysis to identify geological features that could be responsible for the mismatch and then updated the geological model accordingly (**Figure 2.8**). The most important changes are an updated top seal topography of the PS1 and the introduction of secondary splay faults: one fault is located between the CRC-1 and CRC-2 wells and another one - on the north from CRC-2. **Figure 2.9** presents a schematic diagram of the CO<sub>2</sub> migration between the two wells developed on the basis of the history-matching:

- CO<sub>2</sub> moves away from the injection well driven by buoyancy and injection pressure, where the high-permeability distributary channels feature a much quicker rate of propagation than the proximal mouth bar.

- A slight vertical offset at the secondary spay fault slows down the CO<sub>2</sub> movement. However, the high-permeability distributary channels are adjacent to each other at fault, and hence the CO<sub>2</sub> can penetrate the fault.
- CO<sub>2</sub> stops at the primary splay fault and propagates along this barrier towards the south-east.

The new geological model improved the reservoir simulations; however, the simulations still could not explain some characteristic features of the observed plume: (1) the TL images doesn't detect any CO<sub>2</sub> presence in the middle part; (2) CO<sub>2</sub> migrates towards CRC-1 though a narrow corridor (**Figure 2.7a**) and finally, (3) the CO<sub>2</sub> plume seems to be bounded to the northeast. Some significant geological features of the Lower Paaratte Formation are not well understood, and consequently, the static model misses some important structural components. Otherwise, numerous runs of the Eclipse simulator (Schlumberger, 2020) with perturbed reservoir models would be able to reconstruct these plume features.

It is a known problem in reservoir engineering that history-matching requires an accurate initial model, otherwise, the process will not converge (Oliver et al., 2008). Hence, history-matching often relies on judgement and intuition of a reservoir modelling team because a direct examination of the multitude of plausible geological scenarios is prohibitively expensive. In the following, a semi-supervised quantitative interpretation of the Otway seismic data is developed to use the power of the seismic attributes and Artificial Neural Networks to gain new insights into the geological structure of the Lower Paaratte Formation.

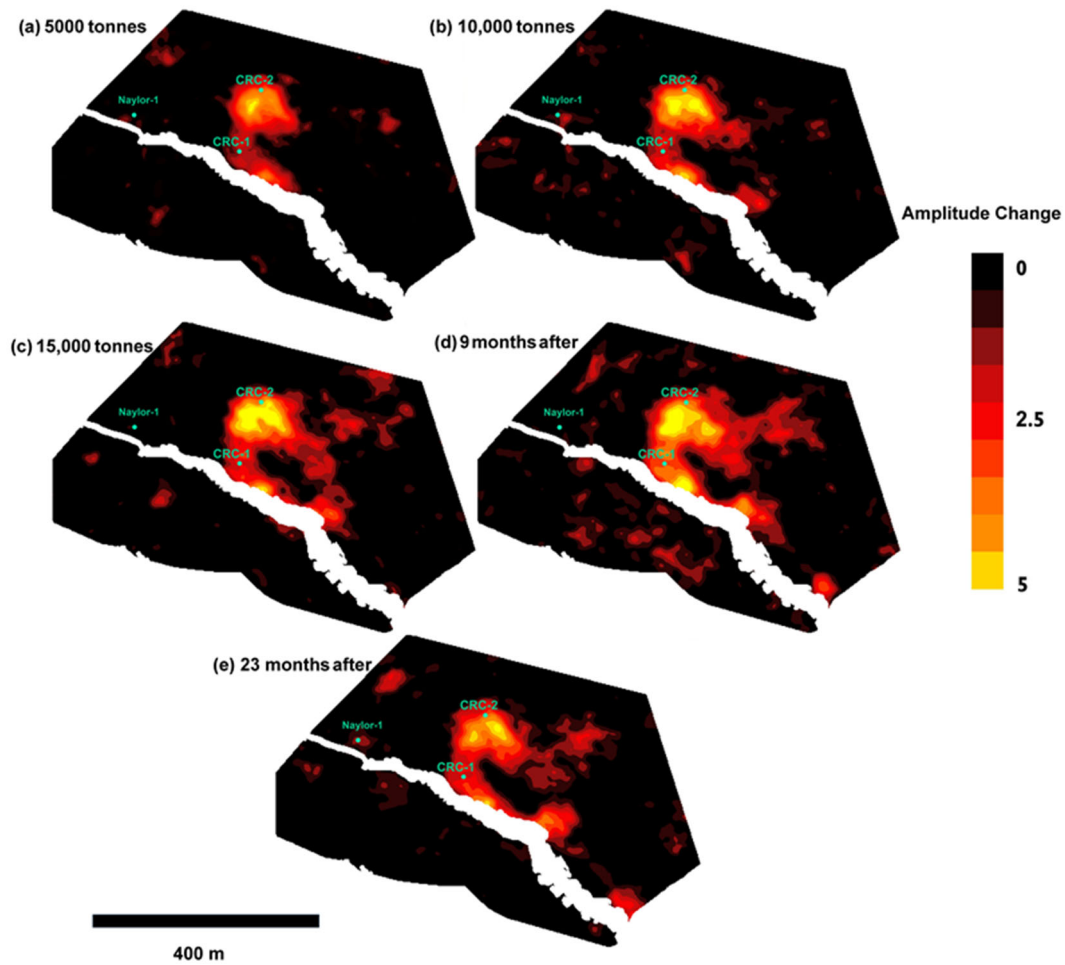


**Figure 2.7** TL seismic response to the Stage 2C CO<sub>2</sub> injection. The colour corresponds to the amplitude change along the top of the injection reservoir after the injection of 5,000 tonnes (a); 10,000 tonnes (b); 15,000 tonnes (c); nine months (d) and 23 months (e) after the end of injection (Aldakheel et al., 2021).

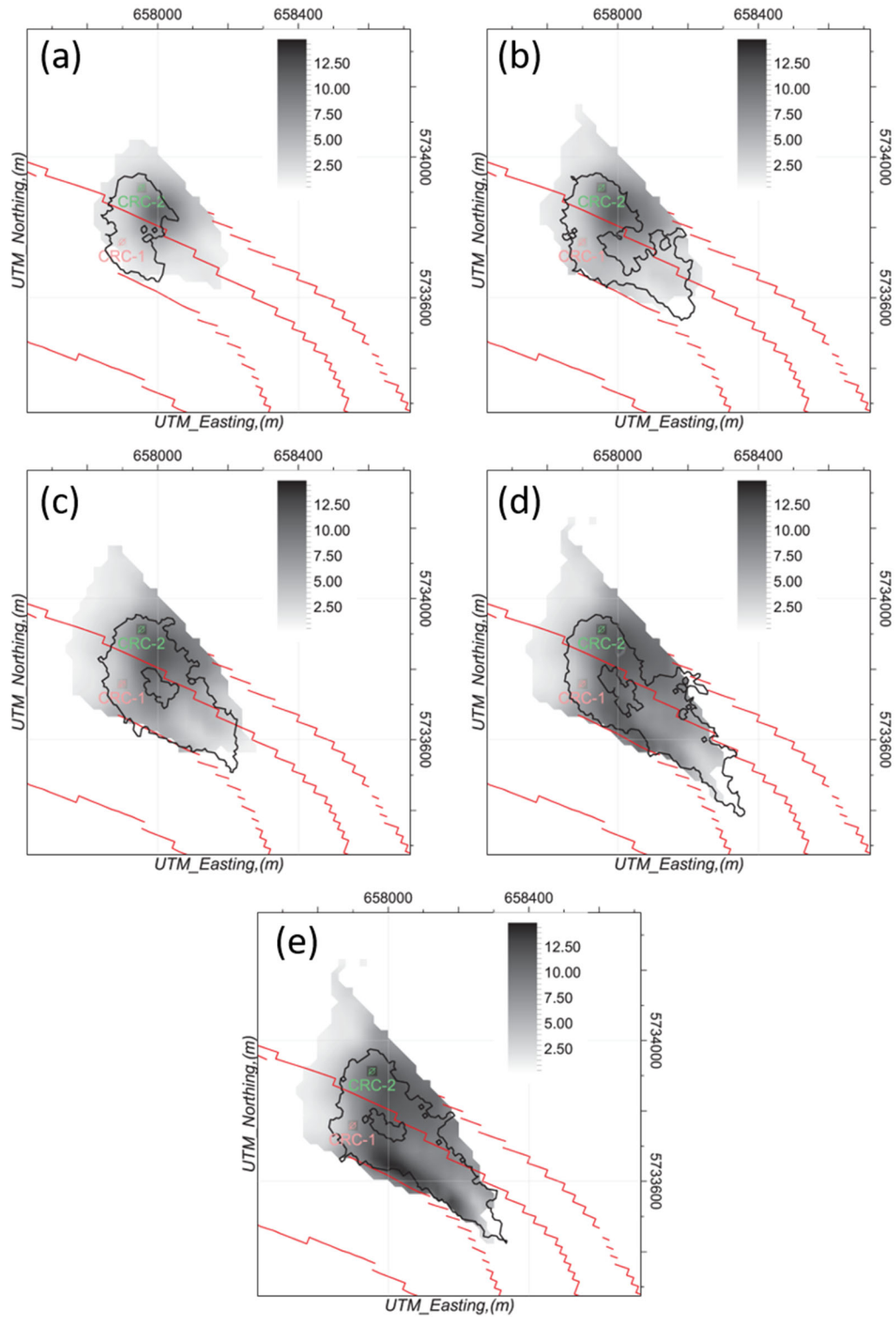


**Figure 2.8** Post-injection reservoir simulation prediction overlaid by the seismically imaged CO<sub>2</sub> plume reservoir after the injection of 5,000 tonnes (a); 10,000 tonnes (b); 15,000 tonnes (c); nine months (d) and 23 months (e) after the end of injection.

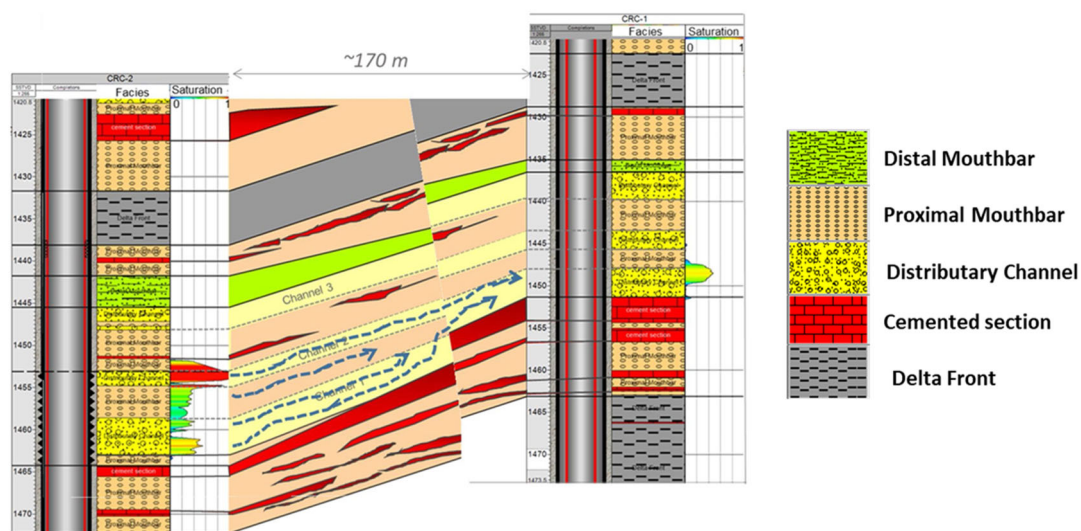


**Figure 2.9** Cross-section of the target reservoir to demonstrate the CO<sub>2</sub> migration between the injection well and an observation well (Dance et al., 2019).

## 2.4 Summary

This chapter summarised the existing geophysical and geological interpretation accumulated by the Otway Project over the last two decades. The main results relevant to the CO<sub>2</sub> plume behaviour in the Lower Paaratte Formation are the following:

1. CO<sub>2</sub> is extracted from the Buttress-1 well (75% CO<sub>2</sub>, 21% CH<sub>4</sub> and 4% heavier Hydrocarbons) is high-mobility fluid, which tends to occupy all accessible reservoir rocks, limited by either discontinuity in geology or the total mass of the injection only. This gas composition is injected in Stage 2C and will be injected in Stage 3.
2. The geology of the Otway Basin and the Lower Paaratte Formation is relatively well-known due to the past hydrocarbon exploration and geophysical monitoring for the Otway Project.
3. As seismic methods are very sensitive to the presence of the CO<sub>2</sub>, the time-lapse anomalies may be considered a proxy for the plume thickness maps due to the tuning effect.
4. The injection interval is heterogeneous both vertically and laterally, which causes a relatively high uncertainty in the CO<sub>2</sub> plume shape prediction using reservoir simulation.

5. The monitoring data from Stage 2C highlighted some sub-seismic faults and lithological boundaries at the injection interval, which improved the match between the reservoir simulations and the observed seismic plume.
6. The history-matched reservoir simulation could not reconstruct several characteristic features of the observed CO<sub>2</sub> plume, which is explained by an in-depth analysis of the seismic attributes in the following sections.

## Chapter 3

### Data QC and seismic interpretation

To compute a set of seismic attributes which may potentially be related to the reservoir properties relevant to the CO<sub>2</sub> migration process in Stage 2C, the first step is identifying the geological units in the seismic data– the process is called seismic to well tie. This analysis is based on a 1D model of seismic wave propagation (the convolutional model) as shown graphically in **Figure 3.1** (Simm and Bacon, 2014), which approximates the seismic trace as a superposition of identical seismic wavelets distributed in time according to the subsurface reflectivity estimated from well logs. Then, structural interpretation extrapolates geological markers identified in the wells by tracing coherent seismic events in a 3D seismic survey. Seismic reflections occur at lithological boundaries with intensity proportional to the contrast of seismic properties of the adjacent layers. Therefore, analysis of the spatial distribution of the seismic amplitudes – seismic Quantitative Interpretation (QI) – provides petrophysical properties of the subsurface. Hence, one may see the quantitative interpretation as seismic-guided interpolation of the well data into a 3D volume.

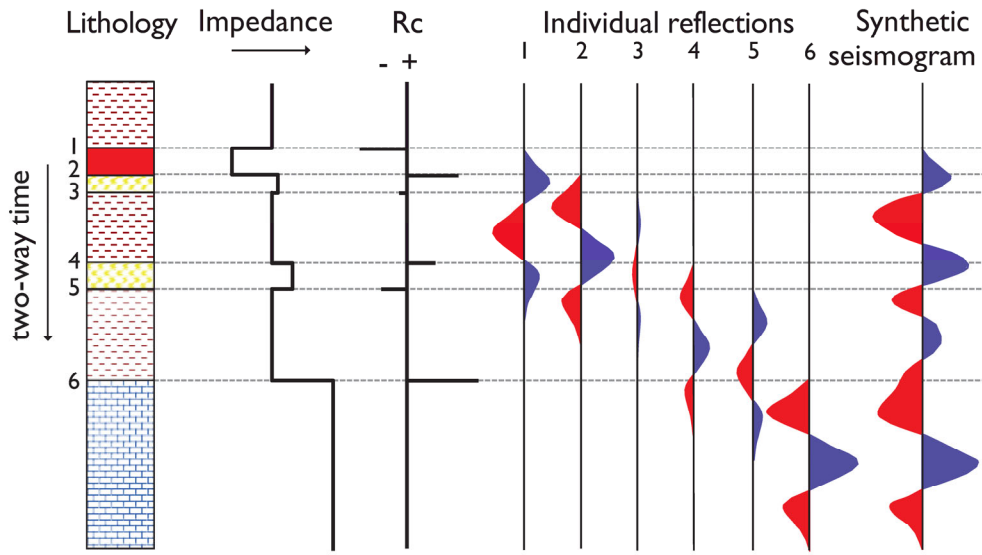


Figure 3.1 Graphical representation of the convolutional model (Simm and Bacon, 2014).

### 3.1 Convolutional model

In the two-way travel time (TWT) domain, the seismic trace  $S[t]$  for a normal incident P-wave can be expressed mathematically as a convolution of a source wavelet  $W[t]$  and the subsurface reflectivity  $R[t]$  plus noise  $n[t]$  (Russell, 1988) :

$$S[t] = W[t] * R[t] + n[t], \quad (1)$$

where the noise term is assumed to aggregate all relevant sources of noise: ambient noise, 3D wave propagation effects, imperfect processing workflow and imaging artefacts. While an additive model of seismic noise is likely to be a simplification for the Otway seismic, synthetic simulations by Glubokovskikh et al. (2020) proved the applicability of this model.

The reflection coefficient at the  $i^{\text{th}}$  geological boundary  $R(t_i)$  for normal incidence is equal to

$$R_i = \frac{I_{i1} - I_{i2}}{I_{i1} + I_{i2}}, \quad (2)$$

where subscripts 1 and 2 denote overlaying and underlying layers, respectively, and  $I = \rho V_p$  is the so-called acoustic impedance. In the case of reflection from a thin layer in a homogeneous background, the convolutional model equations (1) and (2) yield the following expression



$$S_L[t] = (W[t - t_{L1}] - W[t - t_{L2}])R_{L1} + n[t] \quad (3)$$

where index  $L$  denotes the layer parameters and  $t_{L1}$  and  $t_{L2}$  correspond to the time location of the layer's top and bottom boundaries, respectively. If the layer thickness  $h$  is small compared to the characteristic seismic wavelength  $\lambda_L$ , the difference in the brackets in equation (3) approximates the time derivative of the wavelet (Widess, 1973).

$$S_L[t] = (W[t - (t_{L2} + t_{L1})/2])' \cdot \left(\frac{4\pi \cdot R_{L1} \cdot h}{\lambda_L}\right) + n[t] \quad (4)$$

where  $(W[t - (t_{L2} + t_{L1})/2])'$  is a derivative of the original wavelet and  $R_L = \left(\frac{4\pi \cdot R_{L1} \cdot h}{\lambda_L}\right)$  can be seen as an effective reflection coefficient from the layer.

Equation (4) has two important implications for our study. First, it shows that the apparent frequency of seismic signals in seismic images is related to a characteristic thickness of geological layers. Secondly, the equation provides a suitable approximation for the TL seismic signal from a thin plume obtained by subtraction of a monitor and baseline vintages.  $R_{L1}$  should be replaced by an apparent TL change of the reflection coefficient at the plume top. Hence, the interpretation of the TL signal has two main constraints:

- a. The top and bottom of the plume may not be distinguished with the given seismic resolution; and
- b. The amplitude of the TL signal depends on both the change of reflectivity due to the presence of CO<sub>2</sub> and plume thickness.

To illustrate (a) and (b) above, the rock physics modelling by Caspari et al. (2015) provided the following estimates for Stage 2C injection:  $\lambda_L = 60$  m and  $R_{L1} = 0.05$ . For a 3m thick plume, the TL response is 60% of the reflection from an infinitely thick plume. Glubokovskikh et al. (2020) used extensive 3D numerical simulations to show that the Stage 2C plume is likely to be detectable for the plume thicker than 4 m. This explains the clear TL anomaly in the monitoring vintages. The stronger the TL signal, the thicker the plume. Hence, the trough amplitude of the TL signal can be a proxy for plume thickness (**Figure 2.7**).

## 3.2 Data quality

Data preparation and quality control are essential steps for this study because they aim to integrate several data sets generated by various projects over four decades. Although all the data have already been fully processed and interpreted prior to the commencement of this study, differences in the data acquisition and/or processing workflow may become a challenge for a joint analysis. Petrel was the main platform for data systematisation and analysis.

### 3.2.1 Seismic data

Seismic amplitudes bear an overprint of the seismic survey design: acquisition geometry and seismic instrumentation (types of the source and receivers)(Evans, 1997; Chopra and Marfurt, 2007). These effects contribute to the magnitude of noise in the convolutional model. For an inappropriate survey design, these effects may distort a simple link between the seismic rock properties and seismic amplitudes in the convolutional model. The quality of the seismic image at a given point is mainly controlled by three factors:

1. Seismic fold - number of the source/receiver pairs which contribute to the seismic image at this point.
2. Types of seismic source and receivers.
3. Quality of the seismic processing/imaging workflow.

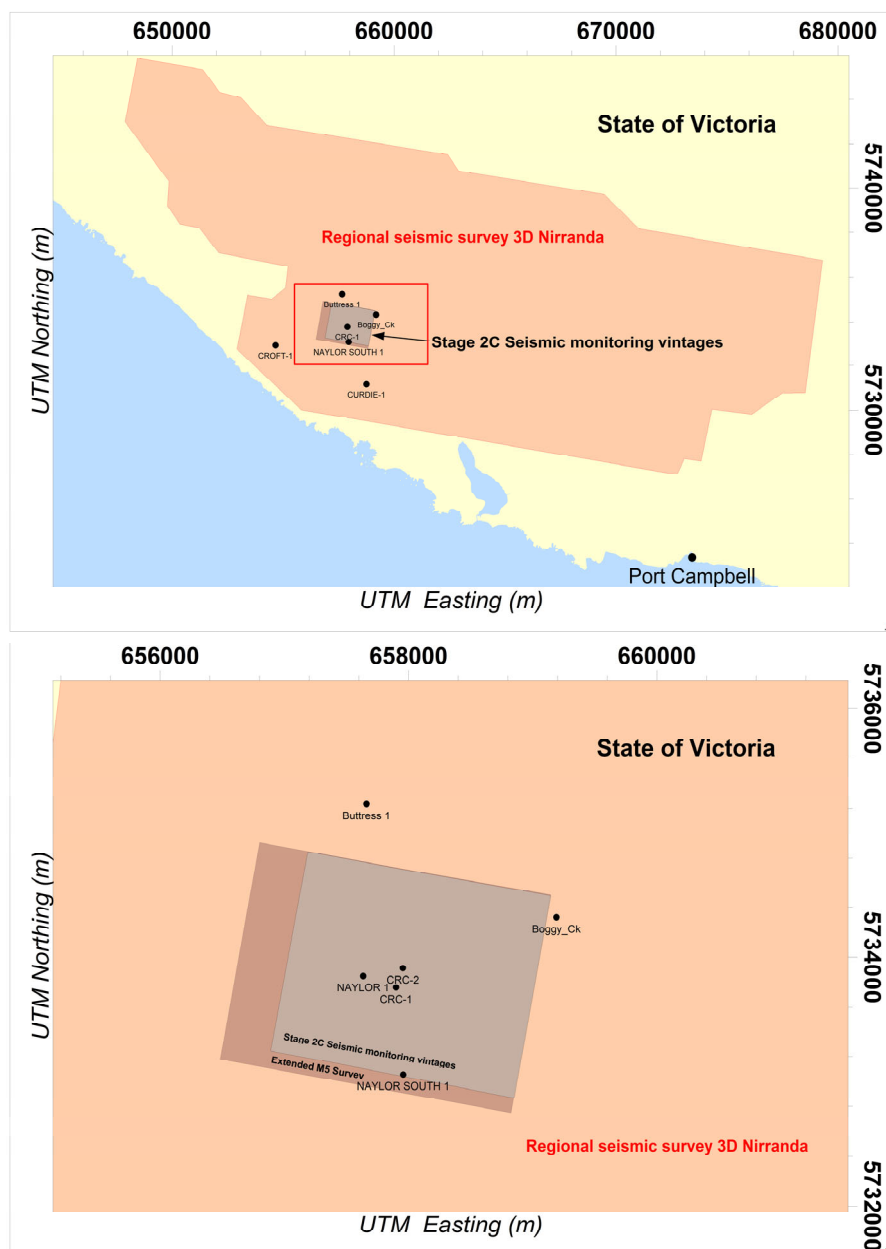


**Figure 3.2** Base map of the available seismic vintages and wells. Regional seismic survey (a) covers a large area and features a large range of the source-receiver offsets. Stage 2C monitoring vintages (b) have a similar seismic fold which is achieved by the high density of the inlines/crosslines.

While the Otway site is covered by several seismic surveys, only three have sufficient quality for quantitative analysis of the seismic attributes (**Figure 3.2**):

1. Nirranda 3D regional seismic survey was mostly acquired using a large vibroseis truck, except two small patches near Curdie river, where the source was dynamite:

- i. Relatively sparse acquisition geometry - inline/crossline spacing is 20m. However, seismic fold is relatively high due to large offset range.
  - ii. All processing procedures are amplitude-preserving.
  - iii. Seismic imaging is done using post-stack time migration.
2. Stage 2C seismic monitoring vintages were acquired using a 15 klbs vibroseis truck and meticulously designed buried receiver geophone array which guarantees low ambient noise (Pevzner et al., 2020b):
- i. Dense acquisition geometry – inline/crossline spacing is 7.5 m, but the nominal fold is comparable with Nirranda 3D due to small offset range ( **Figure 3.3**).
  - ii. All processing procedures are amplitude-preserving.
  - iii. Seismic imaging is done using pre-stack time migration.
3. Stage2C Monitor 5 (Extended M5) survey acquired with an extended source network ( **Figure 3.3**) was designed to improve the seismic image in the vicinity of CRC-3 and refine the geological model for Stage 3:
- i. Dense acquisition geometry – inline/crossline spacing is 7.5m, but the nominal fold is comparable with Nirranda 3D due to small offset range.
  - ii. All processing procedures are amplitude-preserving.
  - iii. Seismic imaging is done using pre-stack time migration.

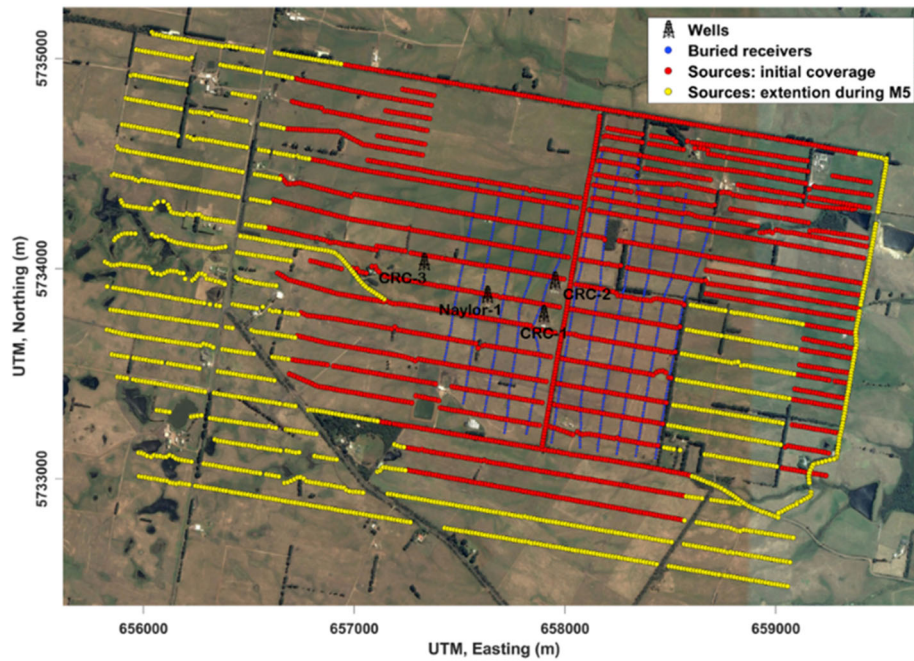


**Figure 3.3** Acquisition geometry for the Stage 2C baseline survey and the Extended M5 survey (Popik et al., 2020).

**Figure 3.4** shows the frequency spectra of all three seismic surveys. The dominant frequency is around 20-30 Hz, although the Stage 2C data feature a wider bandwidth. According to the convolutional model (equation 1), such dominant frequency implies that any two events which are separated by less than 30 m will experience interference and may not be confidently discriminated.

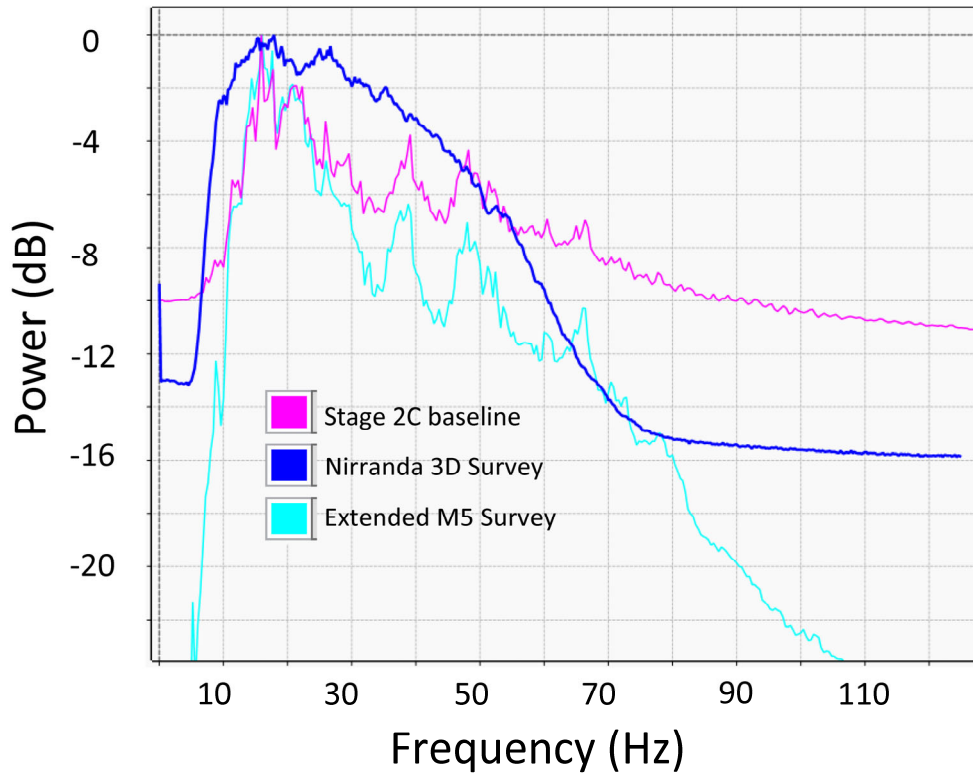


**Figure 3.4** Frequency spectra of all three analysed seismic surveys.

The difference in the seismic processing and survey design results in systematic discrepancies between the three seismic vintages. To analyse them collaboratively, a seismic miss-tie analysis in Petrel is performed, which provides an amplitude gain correction and time shift (**Figure 3.5**).

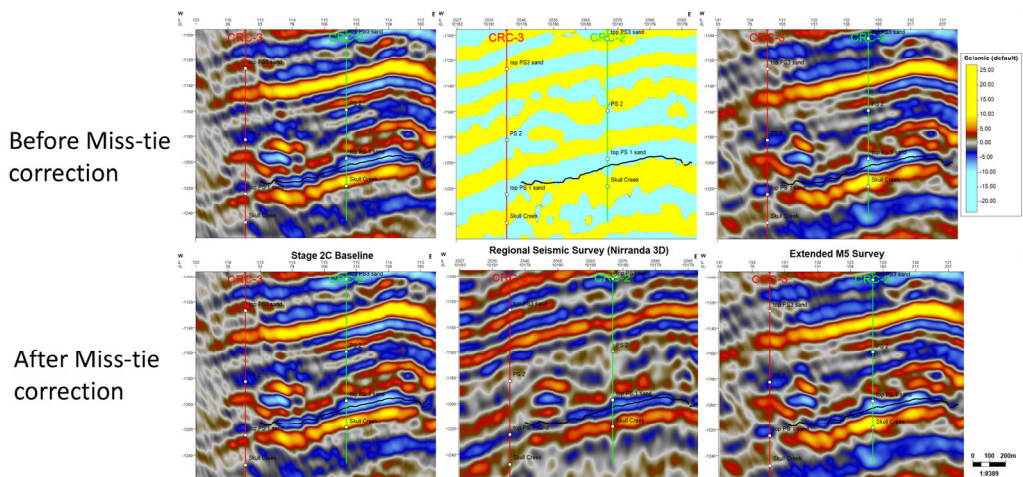


**Figure 3.5** Seismic miss-tie analysis. Due to the difference in acquisition geometry and instrumentation and processing graph, the three seismic surveys have drastically different amplitudes and slightly different shapes of the seismic horizons (top row). a Petrel miss-tie plugin is applied to introduce a single amplitude scalar and time shift (bottom row).

### 3.2.2 Well data

The current geological model for the Otway site (~3 km×3 km) relies on seven CRC wells drilled for Stages 1, 2 and 3 of the Otway Project and eight legacy petroleum wells (Bagheri et al., 2020). In this study, I analysed only four wells which lie within the area of nominal seismic fold for the Stage 2C seismic: CRC-1, CRC-2, CRC-3, and Naylor-1 wells. However, the remaining wells facilitated a better understanding of the regional geological trends.

To assess the quality, I compared the cross-plots between the geophysical logs (sonic velocities and density) and some petrophysical interpretations (neutron porosity, gamma-ray and such) in the wells. Density and compressional velocity are used to calculate the acoustic impedance and reflection coefficients for the seismic to well tie; hence, these measurements are of critical importance. However, stratigraphic correlation and facies schema rely on the petrophysical logs, and hence these are of critical importance as well. Other important components are the check-shot and the interval seismic velocity obtained from the zero-offset VSP, which provides an initial well-tie.

**Figure 3.6** shows a cross-plot between the density and compressional sonic in CRC-1, -2 and -3 and Naylor-1. Naylor-1 appears to behave differently, and it is not following the density-velocity general trend. This discrepancy in the general trend raises a red flag on the quality of the logs acquired in Naylor-1. This well is a legacy petroleum well which was drilled to a target formation at 2000 m depth, so the values in the Lower Paaratte Formation are likely to be computed using some regression equations rather than measured directly. Hence, Naylor-1 well is excluded from our analysis.

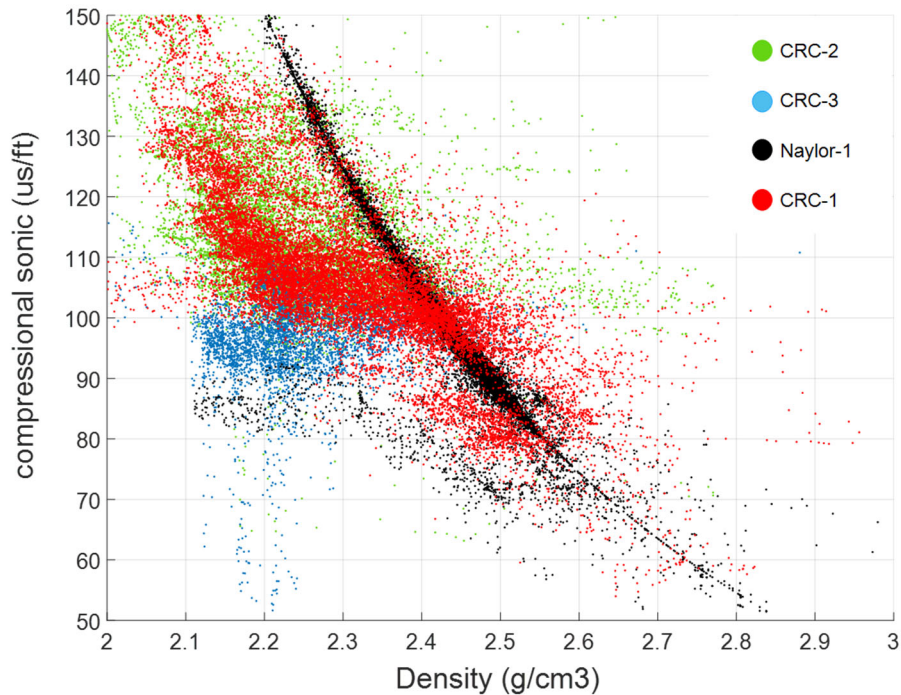


**Figure 3.6** Quality control of the well logs. Compositional cross-plot of the log density vs. sonic interval time for all four available wells indicate that the Naylor-1 logs should be excluded from the study.

### 3.3 Seismic to well ties

As discussed at the beginning of this chapter, the seismic to well tie is a key step in any seismic reservoir characterisation project. Essentially, this procedure applies the convolutional model (equation 1) to establish a link between the amplitudes in a seismic image in the time domain and well measurements in the depth domain. To this end, sonic and density logs are used to compute the subsurface reflectivity  $r[t]$ . The seismic wavelet  $w[t]$  can be obtained by minimising the mismatch between the synthetic trace and the trace extracted from the seismic image (Simm and Bacon, 2014).

The quality of the seismic to well tie is crucial for several reasons. First, it is critical for the time-to-depth conversion of the seismic image. Moreover, the stratigraphic markers identified in the well logs and/or core data can be associated with coherent seismic events (seismic horizons) in the seismic image, and thus extrapolated away from the wells. Second, analysis of the seismic attributes may extrapolate the 3D petrophysical relationships established in the wells such as porosity trends and relationships to the clay content if the link between the rock parameters and seismic properties is sufficiently strong. In the following, we focus on yet another application



of the seismic to well tie: assessment of the feasibility of seismic QI. The convolutional model may result in significant errors due to the following main reasons:

1. Complex subsurface which feature rapid lateral variations of the seismic properties and sub-vertical geological features, so that the wave propagation may not be reduced to a 1D model.
2. Poor well log quality, so that the reflectivity is incorrect.
3. Inadequate imaging workflow which cannot focus the seismic energy back to the reflection points.
4. Complex surface conditions and/or issues with seismic instrumentation which can cause strong overprint on the seismic amplitudes in the raw seismograms.

For the Stage 2C data set, Glubokovskikh et al. (2020) examined in detail the issues associated with (1) and (3) using extensive numerical simulations by Glubokovskikh et al. (2016). The authors concluded that the convolutional model is appropriate for the analysis of the Stage 2C seismic data. Thus, low quality of field data, either well logs or seismic, should be the only reason for the well-tie to fail.

The well-tie workflow applied to CRC-1, CRC-2 and CRC-3 wells include three steps:

1. Initial correction of compressional velocity from sonic logs based on the interval time from zero-offset VSP.
2. A refinement of the time-depth relationship using a statistical wavelet – a zero-phase wavelet, whose amplitude spectrum equals to the total spectrum of the seismic image in the target interval.
3. Estimation of the deterministic wavelet for the time-depth relationship obtained at the previous step. We use the algorithm of Walden and White (1998) implemented in Petrel, which provides valuable statistics to the goodness-of-fit for seismic to well-tie, such as predictability of the seismic trace, the confidence of the estimated wavelet and SNR of the seismic data.

This workflow may be applied to all available wells independently, but the obtained wavelets may be quite different from each other because the wavelet estimation algorithm is susceptible to noise in the data. On the other hand, the wavelets are

expected to be relatively stable spatially within each seismic survey: the surface conditions are very similar across the Otway site, and instrumentation remained the same throughout each survey. Hence, we assume that the estimated wavelet should be the same in the CRC-1, CRC-2, and CRC-3 wells. First, the wavelet is estimated in CRC-2 well, tested in other wells and updated if the observed mismatch is strong. The final wavelet is a result of several iterations of slight refinements of the time-depth relationships and wavelet spectra in all three wells.

The seismic to well tie in the Nirranda 3D (**Figure 3.7**) is good. Both statistical and deterministic wavelets allowed to match the main reflectors in the seismic image. The maximum correlation coefficient between the synthetic and the seismic data has improved from 0.67 for the statistical wavelet to 0.73 for the deterministic wavelet. The wavelet is stable, which was established by testing it in CRC-3 with a maximum correlation of 0.79. The well-tie in CRC-1 is problematic due to the proximity to a fault. The predictability for the deterministic wavelet is ~70%, and the SNR is 2.4.

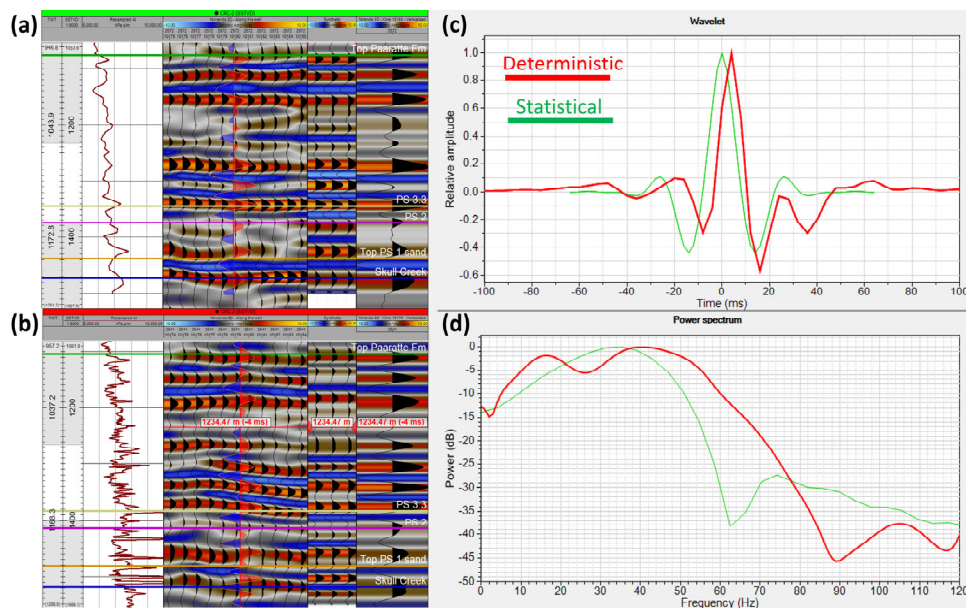


**Figure 3.7** Seismic well-tie for Nirranda 3D survey. The time-to-depth relationship provides a good agreement between the remarkable features in the acoustic impedance estimated from logs and major seismic horizons in CRC-2 (a) and CRC-3 (b). The extracted statistical and deterministic wavelets are shown in time (c) and frequency (d) domains.

The baseline survey for Stage 2C provides a better correlation to the well data (**Figure 3.8**). The correlation has improved from 0.72 for the statistical wavelet to 0.80 for the deterministic wavelet. In CRC-3 the wavelet provides correlation is 0.72 in CRC-3, which is likely to be affected by the reduced seismic fold in the vicinity of

this well. CRC-1 is problematic due to the intersection with a fault. The predictability of this wavelet is 71% and the SNR is  $\sim 2.5$ .

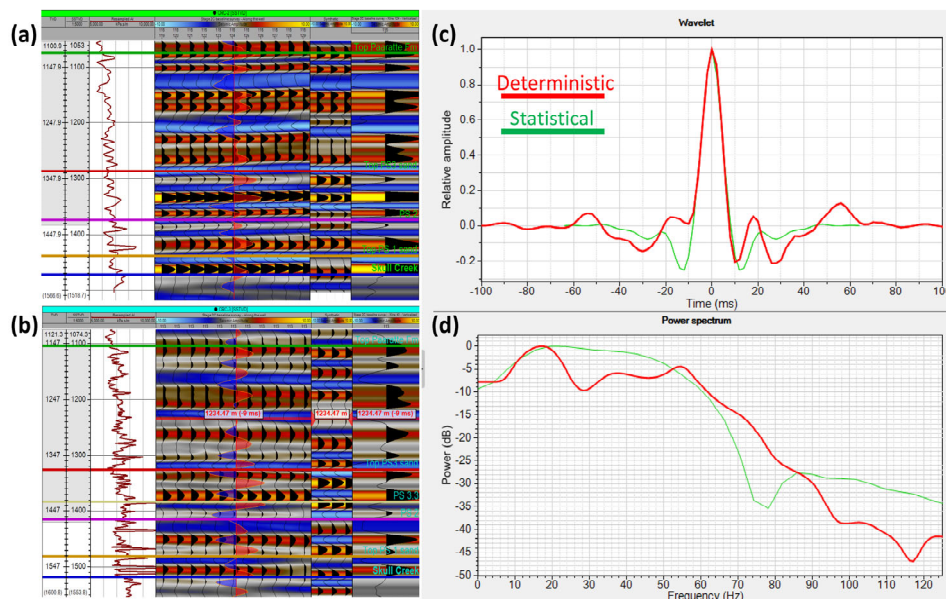


**Figure 3.8** Seismic well-tie for the Stage 2C baseline survey. The time-to-depth relationship provides a good agreement between the remarkable features in the acoustic impedance estimated from logs and major seismic horizons in CRC-2 (a) and CRC-3 (b). The extracted statistical and deterministic wavelets are shown in time (c) and frequency (d) domains.

Extended M5 provides poor correlation in the target interval in CRC-2 because this survey was acquired after the injection while the logs correspond to the pre-injection formation properties. I focused the well-tie on a 40ms interval above the injection interval. As a result, the well-tie provides correlation coefficient 0.7. However, this wavelet gives a correlation coefficient of 0.57 at the target interval in CRC3. This is a relatively poor match, but we could not improve it without introducing unrealistic changes in the time-depth relationship and wavelet spectra. The predictability of the final wavelet is 63%, and SNR is 1.7 (**Figure 3.9**).

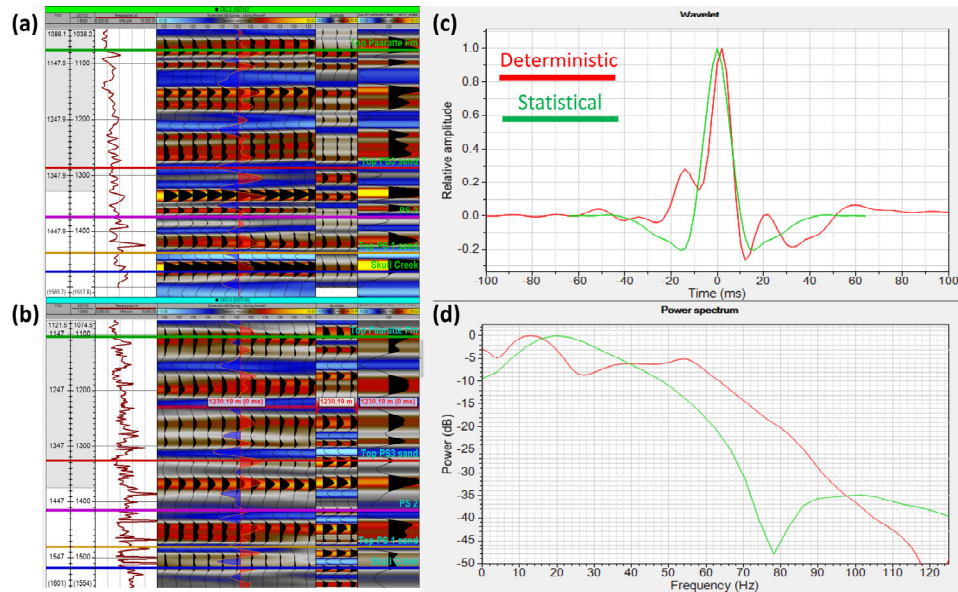


**Figure 3.9** Seismic well-tie for the Extended M5 survey for Stage 2C. The time-to-depth relationship provides a good agreement between the remarkable features in the acoustic impedance estimated from logs and major seismic horizons in CRC-2 (a). However, in CRC-3 (b) the agreement is clearly worse because the wavelet is estimated above the target interval in CRC-2 to avoid the TL seismic signal to the injection. The extracted statistical and deterministic wavelets are shown in time (c) and frequency (d) domains.

### 3.4 Structural interpretation

Building the structural framework concludes the preparatory work for the seismic QI analysis. First, we pick spatially consistent events in the seismic vintages, based on the main stratigraphic boundaries identified in the wells. We focus on five main reflectors in the target interval (**Figure 3.10**):

1. **Paaratte Formation:** top of the Paaratte Formation is a shaly unit where the acoustic impedance increases, and hence the seismic horizon corresponds to peak response. The two-way travel time ranges from -960 to -1080 ms.
2. **PS3 Sand:** top of parasequence 3 within the Lower Paaratte Formation. This boundary corresponds to the beginning of a sandstone section with reduced values of acoustic impedance, and hence we trace a trough. The two-way travel time ranges from -1090 to -1210 ms.
3. **PS2 Sand:** top of parasequence 2 within the Lower Paaratte Formation. A sandstone section with reduced values of acoustic impedance, and hence we trace a trough. This is generally a weak

reflector, and hence picking it is a challenging task in all surveys. The two-way travel time ranges from -1150 to -1205 ms.

4. **PS1 Sand:** top of parasequence 1, which includes the injection interval for Stage 2C and Stage 3. A sandstone section with reduced values of acoustic impedance, and hence we trace a trough. The two-way travel time ranges from -1188 to -1245 ms.
5. **Skull Creek:** top of a thick mudstone section which underlies the CO<sub>2</sub> injection interval. Acoustic impedance increases in this impermeable low-porosity mudstone, and hence the horizon corresponds to peak response. The two-way travel time ranges from -1194 to -11260 ms.

Overall, four out of the five horizons are clear on all seismic vintages, and their signatures are spatially consistent. The surfaces can be picked using a supervised auto-picker implemented in Petrel. Near the splay fault, the horizons are picked manually. Also, the top and bottom of the storage reservoir are picked manually at every crossline and inline because the topography of the formation is known to control the buoyancy-driven CO<sub>2</sub> migration. Every inline and crossline near the fault was manually picked for both PS1 sand and Skull Creek horizons.

### 3.5 Summary

This chapter examined the quality of the seismic and well data suitable for seismic characterisation of the injection formation for Stage 2C experiment. In the following, I will use post-stack time-migrated seismic images provided by a large regional 3D seismic (Nirrandra 3D), Stage 2C monitoring vintages and Extended M5. I used seismic convolutional modelling to correlate the seismic images to the well data from CRC-1, CRC-2 and CRC-3 (Naylor-1 has bad logs), and subsequently picked main seismic reflectors within the target reservoir, Lower Paaratte Formation.

The main findings are:

- The dominant frequency is between 20-30 Hz, which implies that any two seismic reflectors separated by less than 25 m will be smeared by the tuning effect.

- The seismic to well-tie suggests relatively high quality of all three vintages with maximum correlation coefficient between the synthetic and field seismograms  $> 0.7$  and minimum SNR of  $\sim 1.7$ .
- The bandwidth of the Stage 2C seismic is much wider, which, along with a meticulously designed geophone array, improved the ‘sharpness’ of the seismic images and the SNR.
- The TL response at the top of the storage reservoir can be proxy for the CO<sub>2</sub> plume thickness.
- The top and base of the target interval (PS1 sand and Skull Creek) may be traced throughout the seismic volumes, future seismic attribute analysis will be restricted to these two surfaces.

### Chapter 3: Data QC and Seismic interpretation

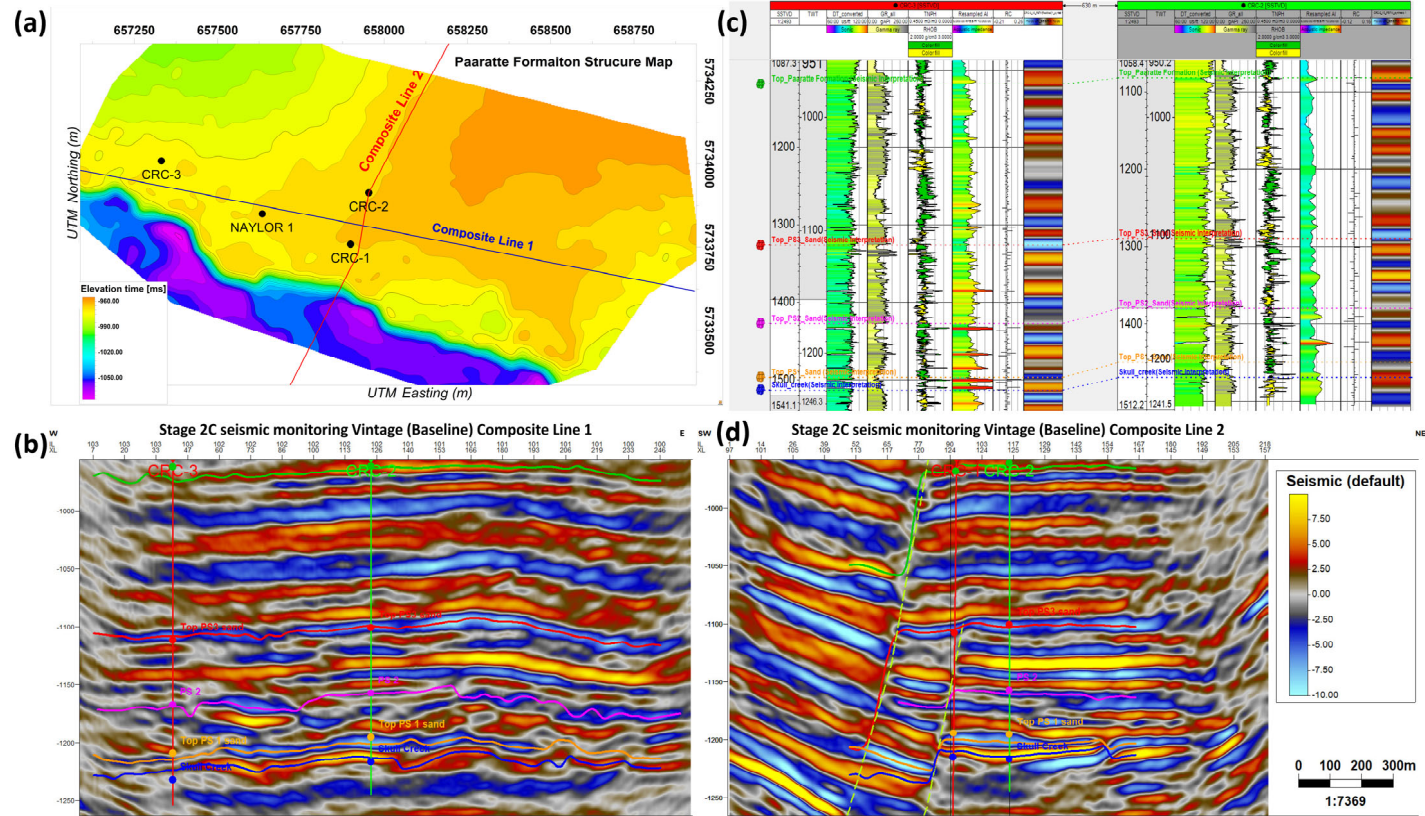


**Figure 3.10** Structure map of Paaratte Formation with two composite lines (a) :CRC2 and CRC3 well logs and the generated synthetic seismogram marked with the main horizons (c) seismic Composite line 1 across the baseline of Stage 2C seismic (b) seismic Composite line 2 across the baseline of Stage 2C seismic monitoring vintages with the main horizons posted and the synthetic seismogram of CRC-1 and CRC-2 (d).

## Chapter 4

# Seismic attributes relevant for the Otway site

As discussed in the Introduction, the identification of the geological features controlling the fluid flow is based on a neural network analysis of seismic attributes. *“A seismic attribute is any measure of seismic data that helps us visually enhance or quantify features of interpretation interest”* (Chopra and Marfurt, 2007). One may split seismic attributes into two big groups: multi-trace and single-trace attributes. Multi-trace attributes usually scan for the similarity between adjacent traces to retrieve the sub-seismic scale geometrical features of the subsurface. Single-trace attributes aim to retrieve the patterns in the vertical distribution of seismic amplitudes, which is often related to reservoir properties, such as porosity, net-to-gross etc. However, simple interpretation models behind the attributes are not strictly valid; hence one needs to test multiple attributes to find those that are most informative in a particular geological situation. Such testing is the focus of this chapter. Below, a description of several attributes relevant to the Otway site is provided and their significance for CO<sub>2</sub> migration discussed. The proposed attributes will be calculated using stage 2C baseline vintage.



## 4.1 Visualization techniques

Prior to the creation of several potential seismic attributes, it is important to discuss how the seismic attributes can be visualized. One way to scan the data for lateral heterogeneity is time slicing. This method enables the interpreter to observe morphological features such as channels and lobes that can indicate a certain depositional system. However, the structural footprint of the basin can mask the sought seismic markers. To overcome this, one needs to flatten the seismic volume to a horizon of interest. This method is called horizon slicing. To demonstrate the power of horizon slicing, **Figure 4.1** shows an example of both a time slice and horizon slices at the PS1 level. The first map (a) shows a time slice at 1210 ms where no stratigraphic features can be recognized due to the structural overprint of the basin. After flattening the volume, some elongated features appeared on the maps, which may be interpreted as channels (b). The third map (c) corresponds to a horizon slice within PS1, where some compartmentalization within PS1 can be observed. The last map (d) shows an elongated body crossing and then opening up; this can be interpreted as a distributary channel dispersing onto a delta. These are just a few examples of how powerful horizon slicing can be, not a conclusion about the depositional system.

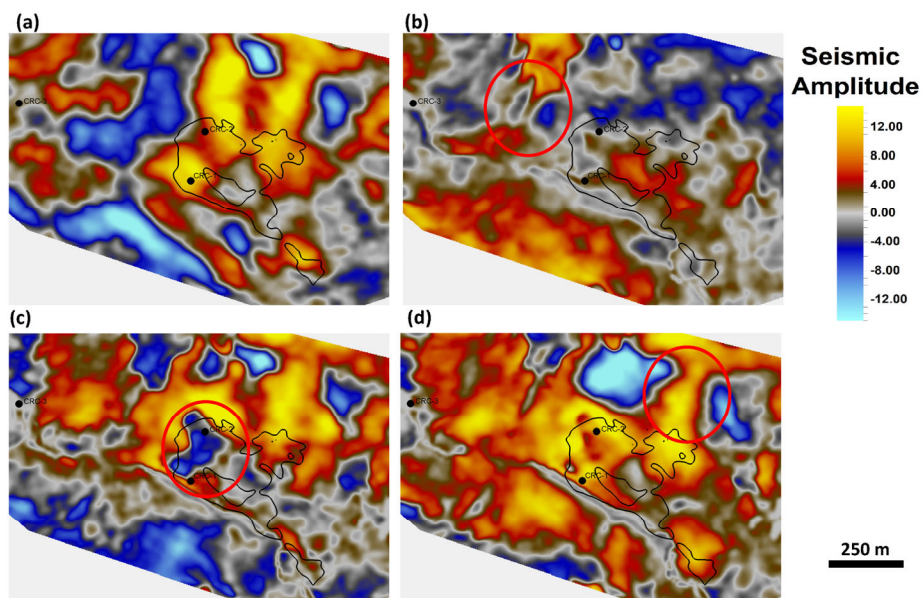


**Figure 4.1** Time slice from Stage 2c baseline (a). Map (b-d) horizon slices within PS1 at different levels.

## 4.2 Structural attributes

### 4.2.1 Horizon curvature

Horizon curvature is a measure of the deformation that a particular horizon exhibits. In two-dimensional settings, the curvature of a particular curve is measured by calculating the reciprocal of the radius of a circle that is tangent to an observed curve. The higher the curvature, the smaller the circle that can be tangent to that curve which will yield high value for the reciprocal of the radius. To distinguish anticlines from synclines, curvature values can be positive to represent anticlines and negative to represent synclines. The straight segment has zero curvature **Figure 4.2** (Chopra and Marfurt, 2007).

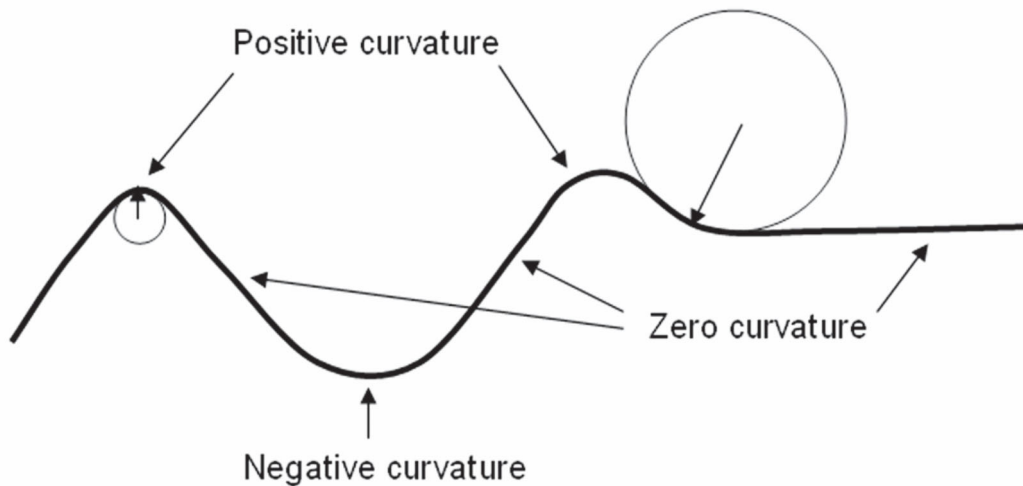


**Figure 4.2** Explanatory graph to show the different curvature values (Chopra and Marfurt, 2007).

In a three-dimensional setting, the curvature of any point on the observed horizon is calculated on its intersection with an orthogonal plane perpendicular to that point on the surface which is called normal curvature (**Figure 4.3**). There are an infinite number of normal curvature values that can be extracted depending on the choice of the intersected plane. There are many ways to characterise the curvature of a given surface. For instance, the plane that has the highest curvature value is called the maximum curvature whereas the curvature on the plane that is perpendicular to it is called the minimum curvature. These values are called the principal curvatures. The average curvature of two orthogonal planes is always constant, which is called the mean curvature (Roberts, 2001).

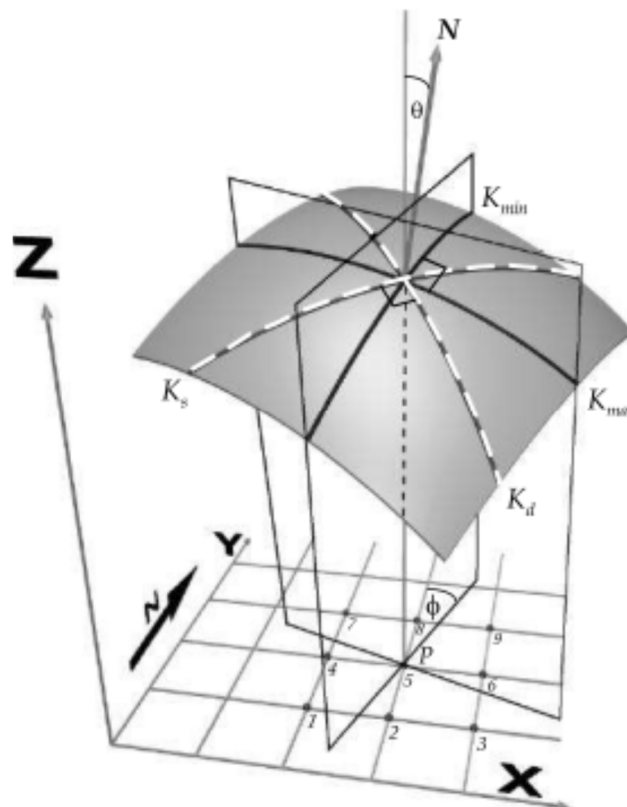


**Figure 4.3** 3D curvatures Calculation plane to highlight the maximum and minimum curvature ( $K_{\min}$  and  $K_{\max}$ ) (Roberts, 2001).

Horizon curvature can identify the existence of faults and fractures. Fractures are effective secondary pores that can serve as conduits for  $\text{CO}_2$ . **Figure 4.4** shows the maximum curvature attribute of PS1 which is commonly used to detect faults (Chopra and Marfurt, 2007). This variation can be an indication of curvature induced fractures. This map can help in predicting the secondary pores in the reservoir to host the injected  $\text{CO}_2$  and highlights fluid flow paths through monolithic rock.

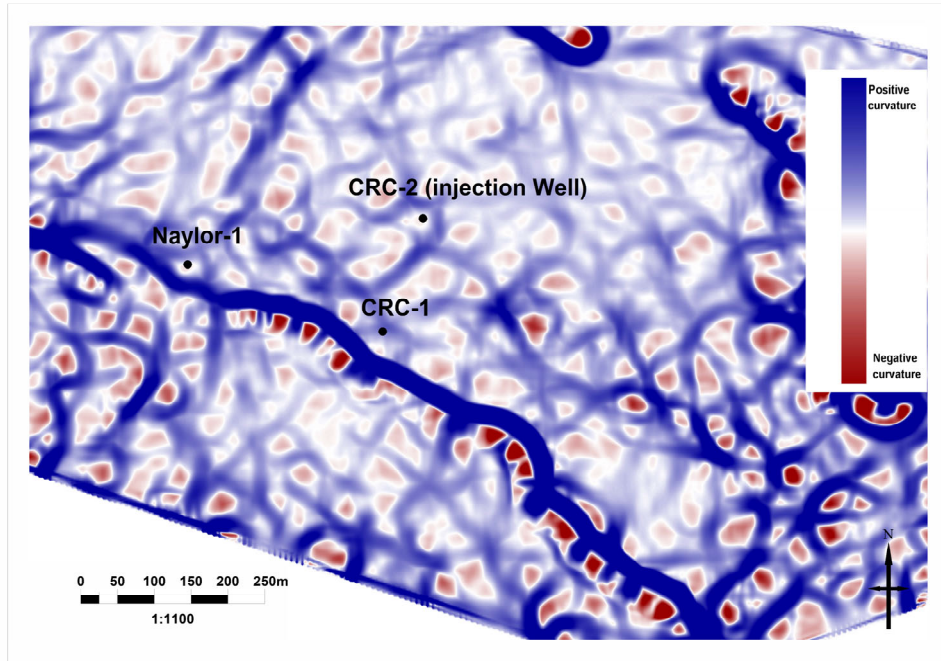


Figure 4.4 The maximum curvature attribute of PS1.

## 4.2.2 Fault Detect

Fault detect is an attribute that takes the difference between the surface and a smoothed version of the same surface. This attribute can highlight discontinuities within any surfaces of interest. **Figure 4.5** shows the PS1 fault detect map. The splay fault in the area is illuminated, which can create an area of fault induced fractures.

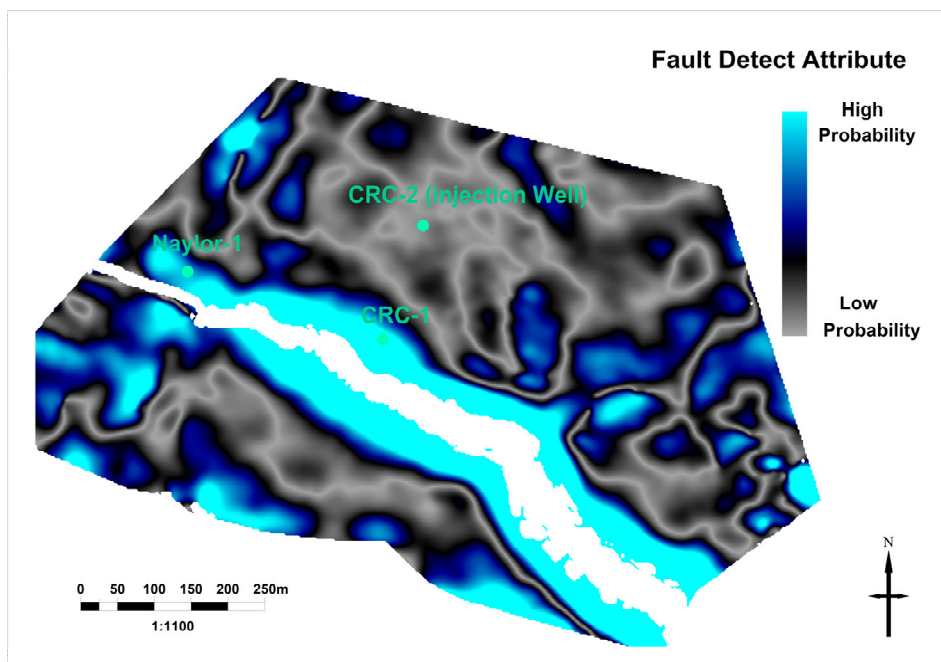


Figure 4.5 Fault Detect map calculated on PS1.

### 4.2.3 Coherence attributes

Coherence is a measure of the similarity between the waveforms of adjacent seismic traces. The seismic waveform is a representation of the response of the source wavelet convolving with the subsurface geology in term of amplitude, phase and frequency (Chopra and Marfurt, 2007). Measuring coherence between traces can highlight subtle lateral changes that are either structurally induced such as faults and fracture zones or stratigraphically induced such as channel systems. Many algorithms have been developed over the years to measure coherency. In this section, coherence is measured using cross-correlation, semblance and eigenstructure methods to find the best approach to highlight the structural and stratigraphic changes within PS1 (the target reservoir).

#### 4.2.3.1 Cross-correlation

This method starts with calculating the maximum positive normalized cross-correlation (MPNXC) over a pre-set time window with an adjacent trace in both the inline and crossline directions. Those maxima are then combined using the formula of Bahorich and Farmer (1995)

$$x = \sqrt{\text{inline MPNXC} * \text{crossline MPNXC}}$$

This process is then repeated on all the traces to form a coherence volume

The cross-correlation is ran on the data where the splay fault is highlighted (red arrow) (**Figure 4.6**).

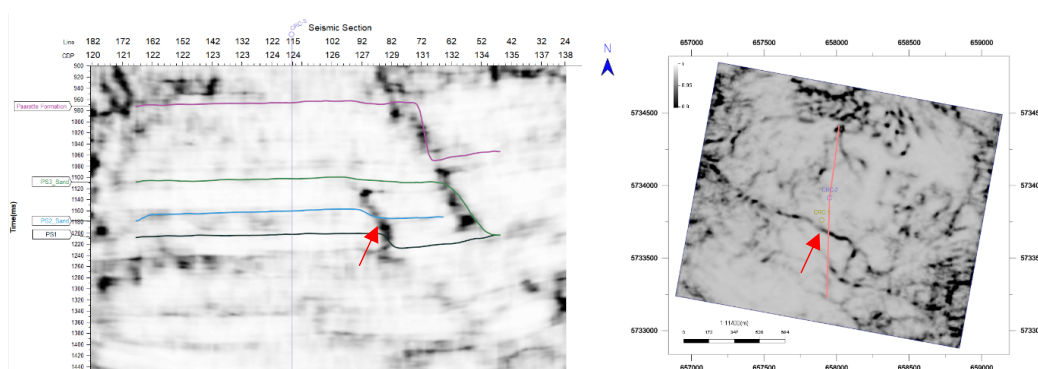


**Figure 4.6** A seismic section taken from a coherence volume calculated using cross-correlation (to the left) and a time slice across the same coherence volume (to the right).

To observe any stratigraphic discontinuity within the area where the plume was injected, a horizon slice is extracted from the coherence volume to eliminate any

structural footprint (**Figure 4.7**). In this figure, there is no clear stratigraphic features that explain the CO<sub>2</sub> migration we observe from the TL signal.

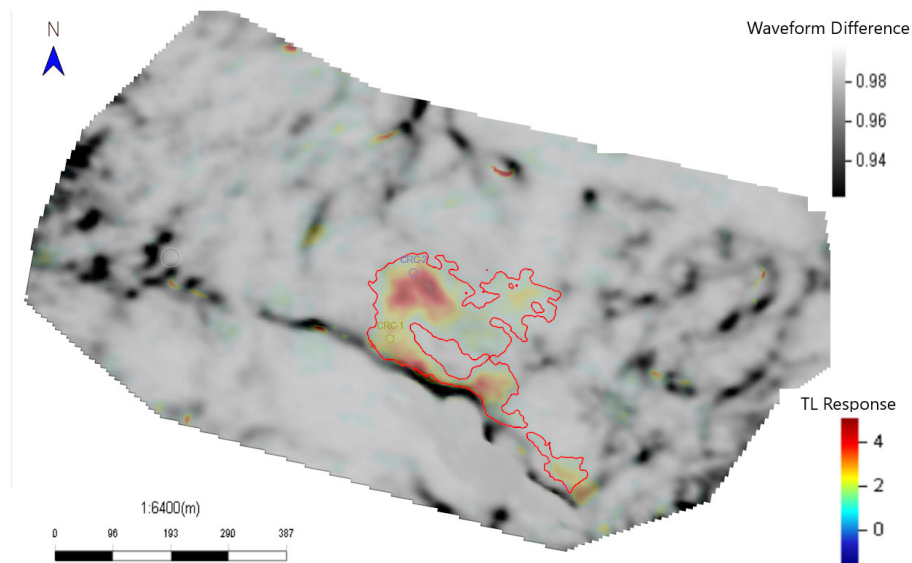


**Figure 4.7** Horizon slice extracted at PS1 from the Cross-correlation method to eliminate any structural footprint overlaid by the detected plume to find any correlation.

### 4.2.3.2 *Semblance*

Semblance is another measure of coherency in the seismic. This method calculates the coherence by estimating the ratio of the energy of the average trace within a specific 3D window to the average energy of all the traces within this window (Chopra and Marfurt, 2007). The semblance-based coherence at the top of the reservoir is also extracted to detect any stratigraphic features that may explain the observed behaviour of CO<sub>2</sub> migration(**Figure 4.8**). There is a weak signal near the red arrow that highlights a minor stratigraphic barrier that may prevent CO<sub>2</sub> migration.

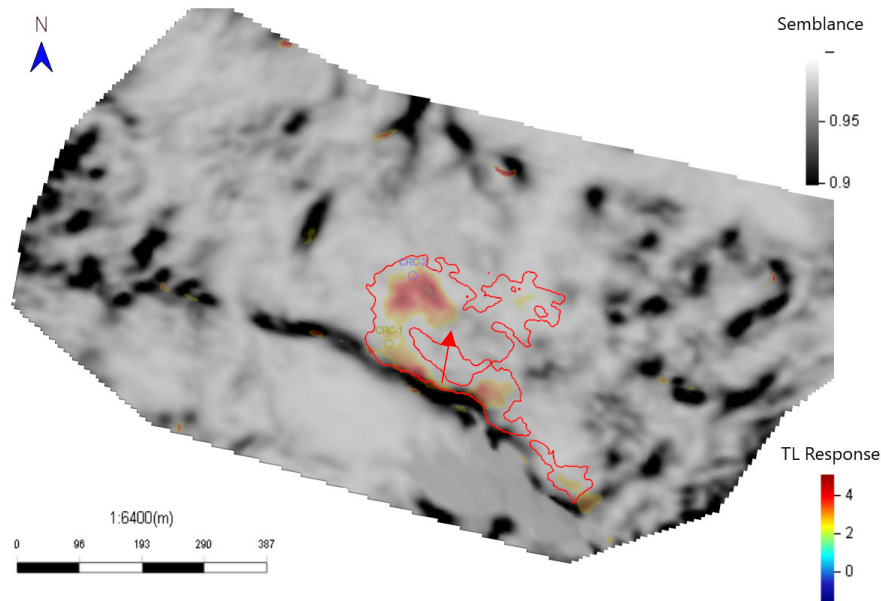


**Figure 4.8** Horizon slice extracted at PS1 from the semblance method to eliminate any structural footprint overlaid by the detected plume to find any correlation.

### 4.2.3.3 Eigenstructure

The eigenstructure method is similar to the semblance method. The first step is to calculate the trace energy in the input window. The second step is to estimate a waveform that represents all the traces in the input window. All the traces in the input window are then replaced by a new trace that has the estimated waveform and the amplitude of the real trace. This step eliminates the influence of the lateral change in the seismic amplitude. The final step is to calculate the ratio of the energy of the modelled traces to the energy of the real traces. This process is repeated on all the traces to create the coherency of the traces (Chopra and Marfurt, 2007). the same process is repeated on the eigenstructure-based coherence, and a minor stratigraphic barrier is also observed at the same location (red arrow) in **Figure 4.9**.

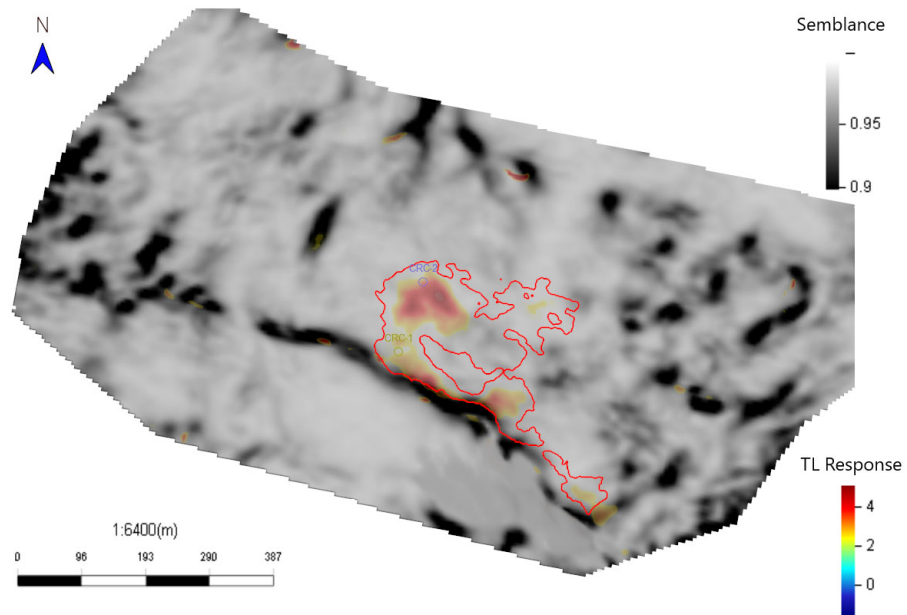


**Figure 4.9** Horizon slice extracted at PS1 from the eigenstructure method to eliminate any structural footprint overlaid by the detected plume to find any correlation.

A weak signal in both semblance and eigenstructure based coherence is observed, which might explain the way the CO<sub>2</sub> has evolved. To exploit this observation, the fault likelihood attribute is constructed which uses a fault-ordinated semblance to detect faults (Hale, 2013) (**Figure 4.10**). This attribute explains the way CO<sub>2</sub> migrates as it stops at the observed barriers.

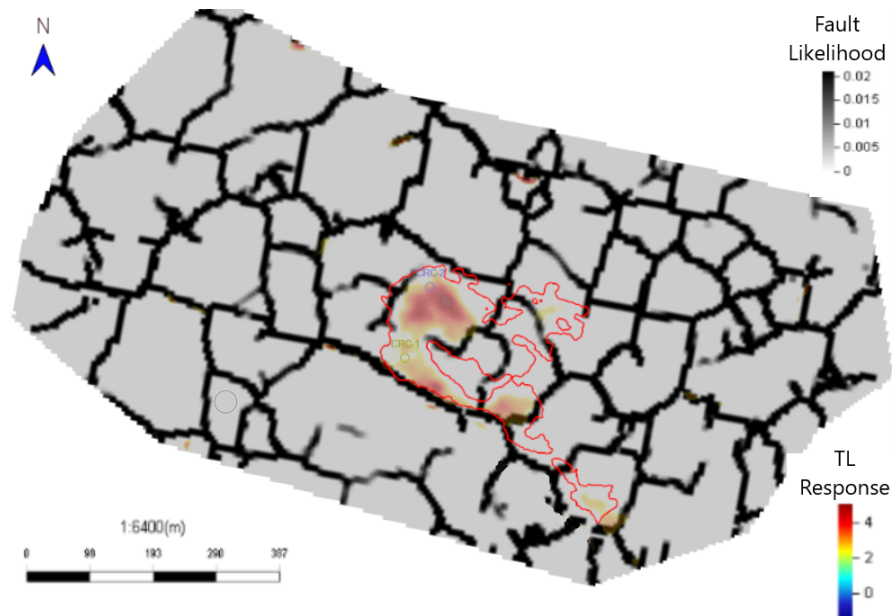


**Figure 4.10** Horizon slice extracted at PS1 from the fault likelihood method to eliminate any structural footprint overlaid by the detected plume to find any correlation.



#### 4.2.3.4 Fault transmissivity attribute

Figure 4.11a is a map of the fault likelihood in the injection interval, which is detected using the algorithm by Hale (2013). The CO<sub>2</sub> plume is likely to be affected by these barriers in the proximity of CRC-2. However, the fault likelihood is independent of the position of the injection well. While CO<sub>2</sub> flow is a directional process, the fault transmissivity attribute (Figure 4.11b) is a transformation of the fault likelihood that also considers the mutual position of the injection well and a fault. This attribute calculates the probability of the CO<sub>2</sub> plume to exist across the minor faults detected using the fault likelihood attribute.

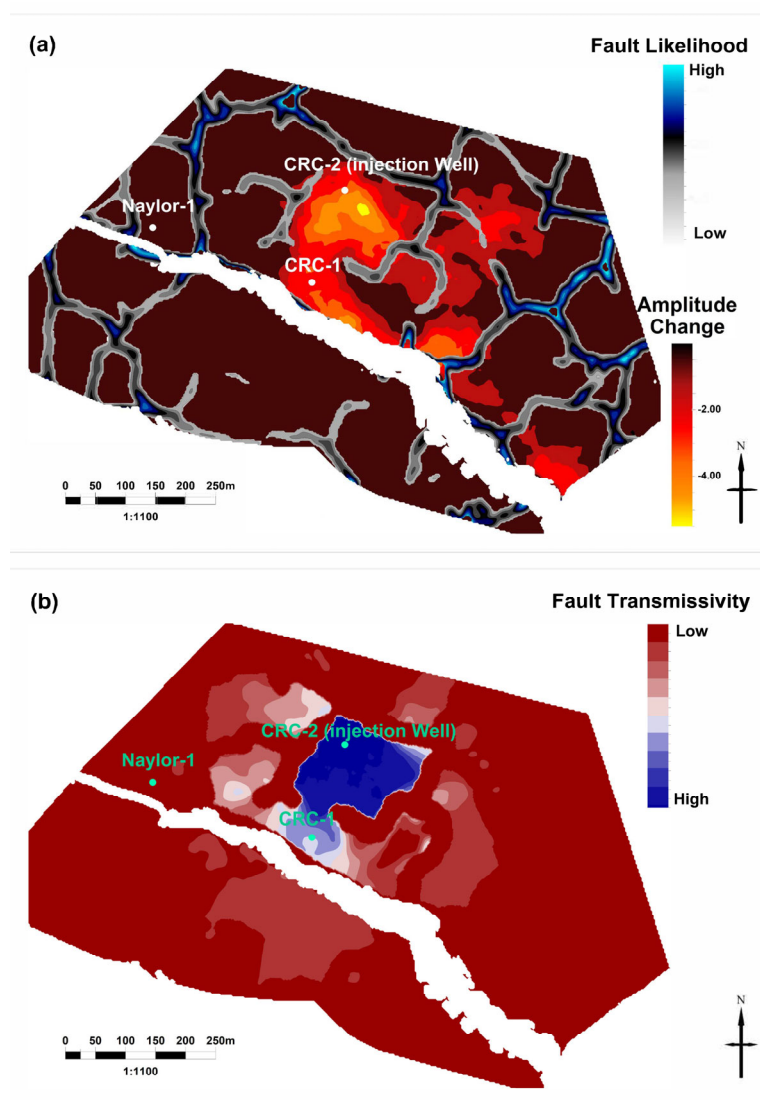
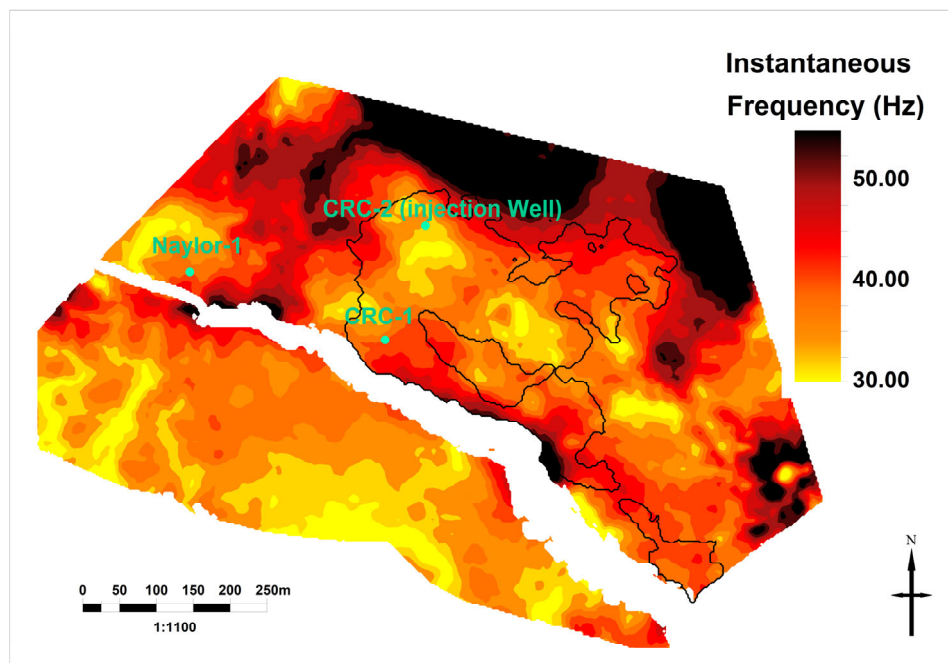


Figure 4.11 Maps of the discontinuities in the seismic data obtained using the Fault Likelihood attribute (a). The underlying map in (a) corresponds to the time-lapse amplitude change at the reservoir top 23 months after the end of injection, and the fault transmissivity attribute (b) (Aldakheel et al., 2021).

## 4.3 Frequency-based attributes

### 4.3.1 Instantaneous frequency

Instantaneous attributes are obtained through Hilbert transform. This transform augments a signal by the imaginary part so that the resulting signal is a complex-valued analytical signal with the real part equal to the recorded data. The instantaneous frequency is the time derivative of the instantaneous phase of the analytical signal (Zeng, 2010). The instantaneous frequency has proven to be a good indicator of sand bodies where lower instantaneous frequency response represents sandy lithology (Ogiesoba et al., 2018). To test this attribute, the instantaneous frequency across PS1 is extracted. **Figure 4.12** shows a map of the instantaneous frequency at the top of PS1 overlaid by the border of the mapped CO<sub>2</sub> plume. The plume appears to be bound to the north where the instantaneous frequency value is high despite the structural high in that area. It seems that the high instantaneous frequency to the north represents an impermeable unit. This attribute is indicative of interference between reflectors; hence, it is not purely diagnostic of lithology.



**Figure 4.12** An instantaneous frequency map extracted at the top of PS1 overlaid by the border of the mapped CO<sub>2</sub> plume.

### 4.3.2 Reflector isochrons

Careful examination of the PS1 reflector shows that the shape of the reflector varies in the injection area. As shown in **Figure 4.13b**, the trough at the top of PS1 gets broader where the CO<sub>2</sub> injection is detected. One way to investigate this change in the reflector shape away from CRC-2 is to change the acoustic impedance in PS1 to match a similar response where the reflector is narrow. A simple feasibility study using convolutional modelling was performed, where soft PS1 sand was gradually replaced by shale with increased acoustic impedance. After mapping the upper and lower zero crossings to track the thickness of the PS1 reflector (**Figure 4.13a**), this attribute appears to be highlighting a similar anomaly observed in the map of the instantaneous frequency.

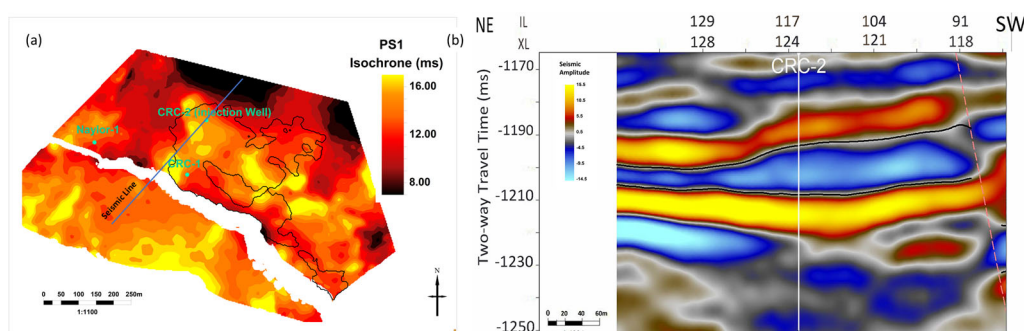


**Figure 4.13** Isochrons thickness map from the upper the lower zero crossing of PS1 reflector (a), Seismic section across to show the thinning of the reflector.

### 4.3.3 Spectral decomposition

Spectral decomposition is a powerful tool capable of characterising thin geological beds. The method relies on equation (4) to analyse the amplitudes of spectral components in the source wavelet. Many transformation methods are available to transform the data into the frequency domain. This study focuses on their application rather than the computational aspects. Red-green-blue (RGB) blending is commonly used to visualise multiple spectral components at once (Chopra and Marfurt, 2007). Each component is assigned a colour where the intensity of each colour corresponds to the amplitude of the assigned spectral component. When all the components are at their highest intensity, the RGB blend will show a white colour, and if the red and green components are high, for example, this mixture will show as yellow. **Figure 4.14** compares a horizon slice within PS1 using RGB blend of multiple frequency cubes and horizon slice of the amplitude. Those frequencies were chosen based on

blending many frequencies combinations. this combination showed the best image of the reservoir that highlight the heterogeneity.

The uplift in the resolution can be easily recognised. The difference in temporal thickness causes the variation of the obtained colour, and hence channel features and internal structure of the interval become clearer. These images will be used qualitatively to understand the complexity of this reservoir.

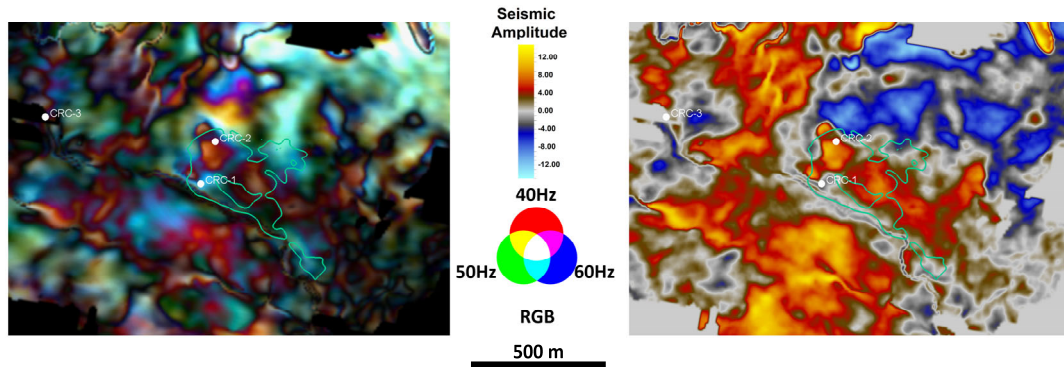


**Figure 4.14** A horizon slice across PS1 using an RGB blend volume of 40, 50, 60 Hz tuning cubes (to the left) and a horizon slice across PS1 using amplitude volume (to the right).

### 4.4 Seismic amplitude

The top and the base of the reservoir depends on the contrast of the seismic properties of reservoir rocks and surrounding mudstones, as indicated in equation (2). Extracting the seismic amplitude at the top and the base of the reservoir (**Figure 4.15**) should highlight changes in the acoustic impedance within the reservoir if both the overlaying and underlying rocks are homogeneous. Normally, the reservoir intervals are the most lethargically heterogenous, hence, this assumption can be made. In the study area, 14 wells have confirmed the homogeneity of the mudstone enclosing the reservoir. The acoustic impedance is the product of density and velocity which can be affected by porosity, lithology and fluid content The seismic attribute can also be an indication of the reservoir thickness due to tuning (Khare and Martinez, 2008)

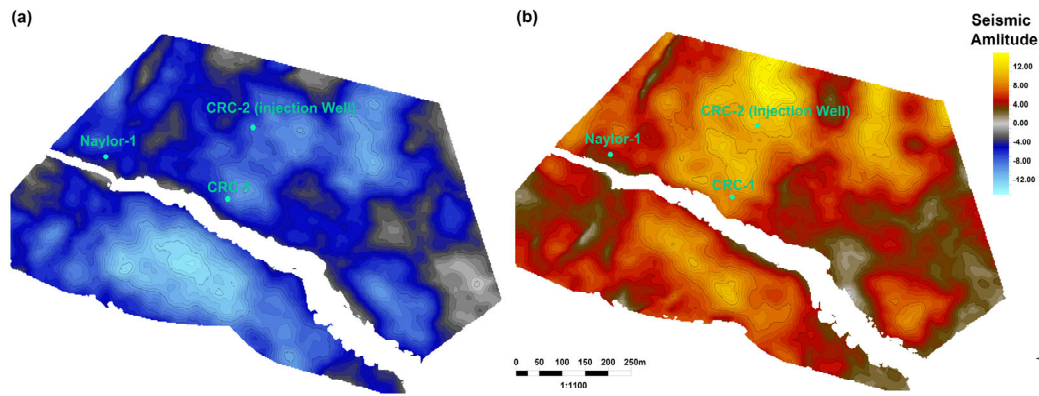


**Figure 4.15** Amplitude maps extracted from the Stage 2C baseline seismic vintage at the top (a) and the base (b) of the injection interval (Aldakheel et al., 2021).

### 4.5 Summary

In this chapter, several seismic attributes were highlighted which may represent the geological features which control the CO<sub>2</sub> migration process based on their standard interpretation as outlined in literature. These attributes will be part of the input of the ANN model to reconstruct the TL response due to the CO<sub>2</sub> injection.

The main findings in this chapter are:

1. Horizon slicing can be a powerful tool to highlight stratigraphic features.
2. Coherence attributes can detect subtle discontinuities within the reservoir which may constrain the migration process. Moreover, anomalies can be an indication of minor faults which may create secondary porosity.
3. Frequency based attributes may be used to map the sandstone bodies within the reservoir interval.
4. Seismic amplitude may highlight variation porosity, thickness or both.

## **Chapter 5**

# **Neural network model building for CO<sub>2</sub> plume characterisation**

The aim of this chapter is to infer which baseline features (expressed quantitatively through seismic attributes measured on baseline data) control CO<sub>2</sub> migration using CO<sub>2</sub> plume geometry evolution obtained from 4D data. More specifically, a monitoring data set from Stage 2C is used to establish a subset of the most informative seismic attributes, the attributes that have a strong link to geological features that control CO<sub>2</sub> migration in the Paaratte Formation. First, the baseline seismic volume is used to generate a large set of seismic attributes that may conceivably be related to the CO<sub>2</sub> plume shape. Then, an artificial neural network (ANN) is trained with all the attributes as an input to reconstruct the observed CO<sub>2</sub> plume. Glubokovskikh et al. (2016) examined the accuracy of the time imaging. The analysis of full-elastic 3D simulations showed that the time images provide an adequate structure of the subsurface, although not ideal. In reality, when a precise velocity model is unavailable, depth images may even have lower accuracy than the time images.

## 5.1 Artificial Neural Network

ANN is a term that refers to a structured function where relationships between input and observed response are represented through a series of sequential relatively simple transformations (layers). Such an approach has been proved effective in learning complex relationships between phenomena of various nature. Complicated geophysical interpretation can also benefit from using this tool (Poulton, 2001). Due to the complexity of the CO<sub>2</sub> migration process where many factors compete to alter the way the CO<sub>2</sub> propagate in the subsurface, Artificial neural network was implemented. In this exercise, the Neural Network Pattern Recognition application in MATLAB is utilized which uses a two-layer feed-forward Network (**Figure 5.1**). This method undergoes two phases: feed-forward phase and error backpropagation phase. The feed-forward phase is used to arrive to the desired solution. This phase contains a hidden Layer and an output layer. The hidden layer contains numerous of segments (neurons) that can be set by the user. Each attribute in the input matrix is assigned to a weighting component (W) for each neuron and each neuron is assigned to a bias component (B) to predict the output. The weighted sum of all the components in each neuron is inserted into an activation function which is the sigmoid function in this case to simplify the calculation in the backpropagation phase. The output of this layer is inserted into the output layer where a summation of all the components is performed and another weighting component to this summation is assigned. Another activation function is introduced which is the SoftMax function in this case to derive the desired output (CO<sub>2</sub> presence). The second phase is the backpropagation phase where the error between the modelled output and the training dataset is calculated. Using the scaled conjugate gradient method (Møller, 1993), all the weighting and bias components can be recalculated to decrease the error in the output. Those phases are repeated until one of these conditions is met (The Math Works, 2006):

- A) The maximum number of iterations is reached.
- B) The maximum time is reached.
- C) The desired performance is met.
- D) The minimum rate of improvement is reached.
- E) When validation test continues to improve multiple times in row.

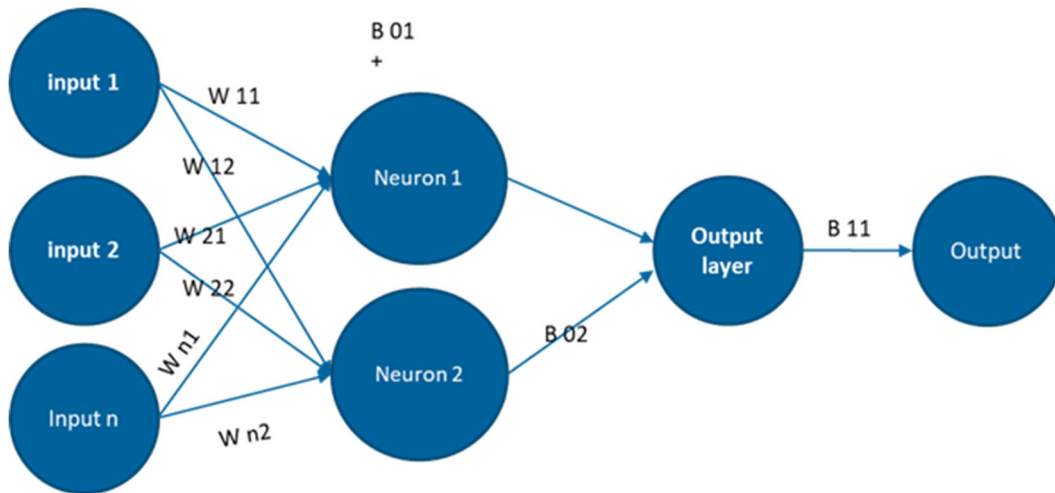


**Figure 5.1** Two-layer feed-forward Network used in this study.

To estimate the prediction accuracy for a trained ANN, a methodology is developed that accounts for a spatial correlation of the seismic data and geological features. The importance of an input predictive feature is then to be evaluated by the accuracy reduction when this feature can be excluded from the input. Spatial distribution of the area with a substantial accuracy reduction provides an insight into the geological features underlying the investigated attributes. The proposed workflow can be used to refine a geological model before performing costly physics-based simulations. Moreover, the trained ANN can then be used as proxy for fluid flow simulator to predict a stabilised CO<sub>2</sub> plume for Stage 3.

ANN algorithms may be used to effectively process the rich Stage 2C dataset to establish a set of seismic attributes that should guide post-injection reservoir modelling. Ideally, such a tool would quantify an information value of various pieces of the available data based on their relationships with the observed TL seismic image of the injection. To formalise this concept into an effective algorithm, one needs to specify what is the input data (predictive features) and the desired output (ground truth). These choices will guide the selection of an adequate ANN architecture, and how it should be optimised and trained.

## 5.2 Ground truth: the seismic image of the Stage 2C plume

The first task is to introduce the ground truth. For our study, the ground truth is the seismic image of the Stage 2C injection. Quantitative interpretation of the seismic data that provides the basis for the current geological model of the Otway site relies on four wells: Naylor-1, CRC-1, CRC-2 and CRC-3 (Dance et al., 2019;



Glubokovskikh et al., 2020). The data acquired in these wells has allowed the seismic features to be attributed reliably to geological boundaries as well as the seismic response corresponding to variations of the reservoir properties and fluid composition.

Lebedev et al. (2013) measured the elastic properties of core samples from the Lower Paaratte Formation versus pore pressure and CO<sub>2</sub> saturation. These measurements show that the injection pressure is likely to be too small to cause any noticeable seismic response, while even small CO<sub>2</sub> saturation can quickly reduce the acoustic impedance according to the Gassmann's fluid substitution and therefore causes pronounced change in the reflection coefficient (Caspari et al., 2015; Pevzner et al., 2017a). Glubokovskikh et al. (2020) showed that the Stage 2C CO<sub>2</sub> plume should be detectable once its thickness exceeds 4 m, hence it is assumed that the plume's extent may be reliably determined by the TL amplitude anomaly at the top of the injection interval - PS1 horizon extracted in the previous chapter.

Over time, the plume is growing towards south-east from the injection well (CRC-2) along the major fault: the Naylor South splay fault (the splay fault) (Pevzner et al., 2017a). The plume thickness and lateral dimensions are comparable with the seismic resolution. Furthermore, the observed TL amplitude may be affected by the imperfect seismic repeatability and uneven spatial distribution of the seismic coverage. In the following, the binarized Monitor 5 TL anomaly - plume/no-plume according to a certain amplitude threshold is used as ground truth (see **Figure 5.2**). It is expected that this classification approach should be more robust than a regression of the continuous distribution of the TL amplitude.

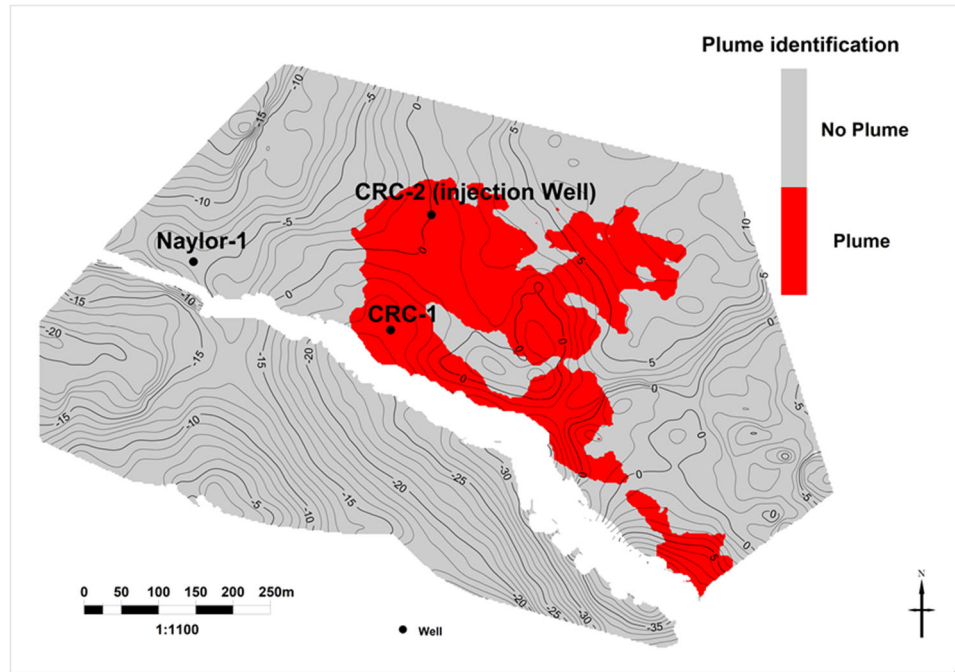


**Figure 5.2** CO<sub>2</sub> plume shape in the last monitoring seismic survey, 23 months after the end of injection. The binary image is obtained by using a threshold for the time-lapse amplitude change at the reservoir top. Contours represent the relative top-seal elevation to the injection well.

### 5.3 Input data: a set of predictive features

After the ground truth plume image is defined, we need to choose the input attributes for ANN. The number of such attributes needs to be reasonably small to avoid overfitting. Prior to running a formal ANN, this choice of attributes should reflect our intuitive understanding of the features that control the fluid flow. Our set of attributes may be divided into four groups, each group characterising a different aspect of the injection process: (1) structural framework of the reservoir (faults, top and bottom of the injection reservoir); (2) amplitude-based attributes strongly related to the reservoir properties (porosity and permeability) as well as lithology; (3) seismic frequency-based attributes controlled by reservoir thickness, scale of heterogeneity and seismic velocity. The fourth group of attributes is non-geophysical but accounts for some basic features of CO<sub>2</sub> flow through rocks: distance from the well.

#### 5.3.1 Structural attributes

The two-way travel time from the top of the injection interval is picked in the baseline seismic vintage. Since supercritical CO<sub>2</sub> is ~30% lighter than brine, the CO<sub>2</sub>

migration follows the structural dip to fill in the top of the storage formation. Due to its high mobility, injected CO<sub>2</sub> infiltrates through the reservoir rocks if its amount i.e. saturation is sufficient, unless the contiguous CO<sub>2</sub> plume hits structural boundaries: sealing faults or abrupt changes in lithology. According to the TL seismic and history-matched reservoir simulations, the Stage 2C plume stabilised one year after the injection stopped. Hence, it is assumed that the top seal topography along with the splay fault (**Figure 5.3**) control the plume shape revealed in the Monitor 5 seismic survey.

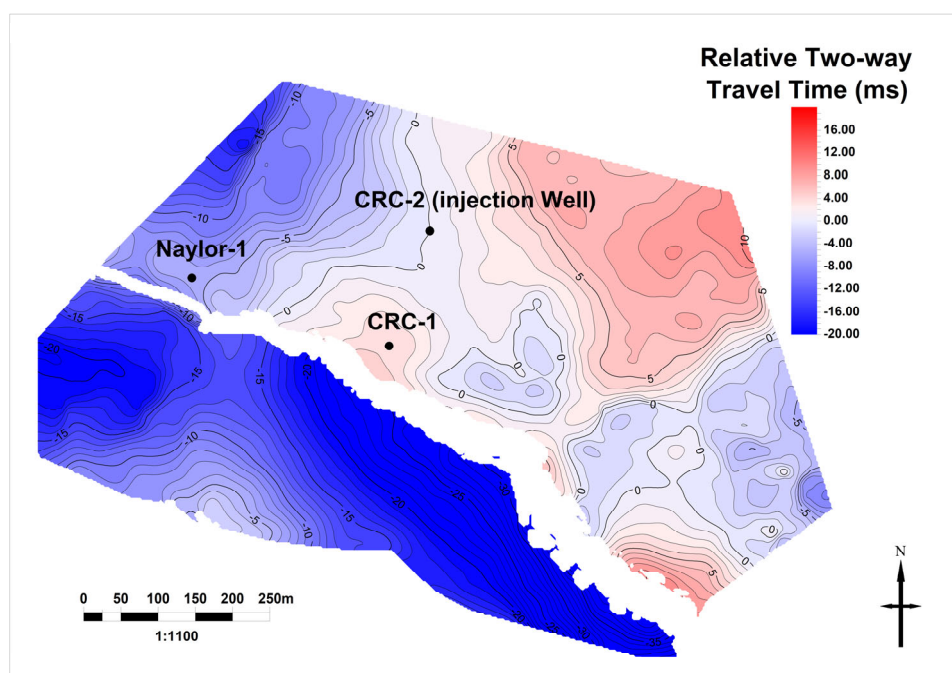


**Figure 5.3** Relative two-way travel time (relative to the injection point at the injection well) of the top seal TWT topography.

The CO<sub>2</sub> plume is also likely to be affected by the small faults in the proximity of CRC-2, and thus another input attribute is the likelihood of a small-amplitude fault (in the injection interval) obtained by using the algorithm of Hale (2013) (**Figure 4.11a**). A relatively aggressive version of this algorithm is applied to delineate subtle discontinuities in the seismic image, because major faults have been already picked by the structural interpretation. This attribute was transformed to the fault transmissivity attribute to account for the mutual location of the injection well and the minor faults (**Figure 4.11b**) (see Fault transmissivity attribute).

The fault detect attribute was also considered to highlight any sudden change in the curvature of top of the reservoir. This curvature can be an indication of curvature

induced fractures which may contribute to the creation of secondary porosity in the reservoir (**Figure 4.5**).

### **5.3.2 Amplitude-based attributes**

The seismic properties of mudstones, which enclose the reservoir, change only slightly between the well logs from fourteen boreholes in and surrounding the Otway Project site, and thus the spatial variations in the amplitude are likely due to the reservoir properties: porosity, clay fraction, etc. **Figure 4.15** shows the amplitude map extracted from the baseline seismic survey at the top and the base of PS1 sand where CO<sub>2</sub> was injected.

### **5.3.3 Seismic frequency-based attributes**

Another group of useful attributes are frequency-based attributes, which can be good indicators of sand bodies and interbedding. A shift towards lower frequencies corresponds to sandstone bodies embedded into clay-rich rocks (Ogiesoba et al., 2018). **Figure 5.4a-c** shows the instantaneous frequency, maximum frequency and isochrons of the reservoir reflector maps. All of these characterise the temporal thickness of the reservoir, and hence the maps exhibit similar spatial patterns. The trough at the top of the reservoir gets broader in the vicinity of the injector and pinches out in the north (**Figure 5.4d**). Reflector isochron has been chosen to represent this group of attributes as it was the most stable one.

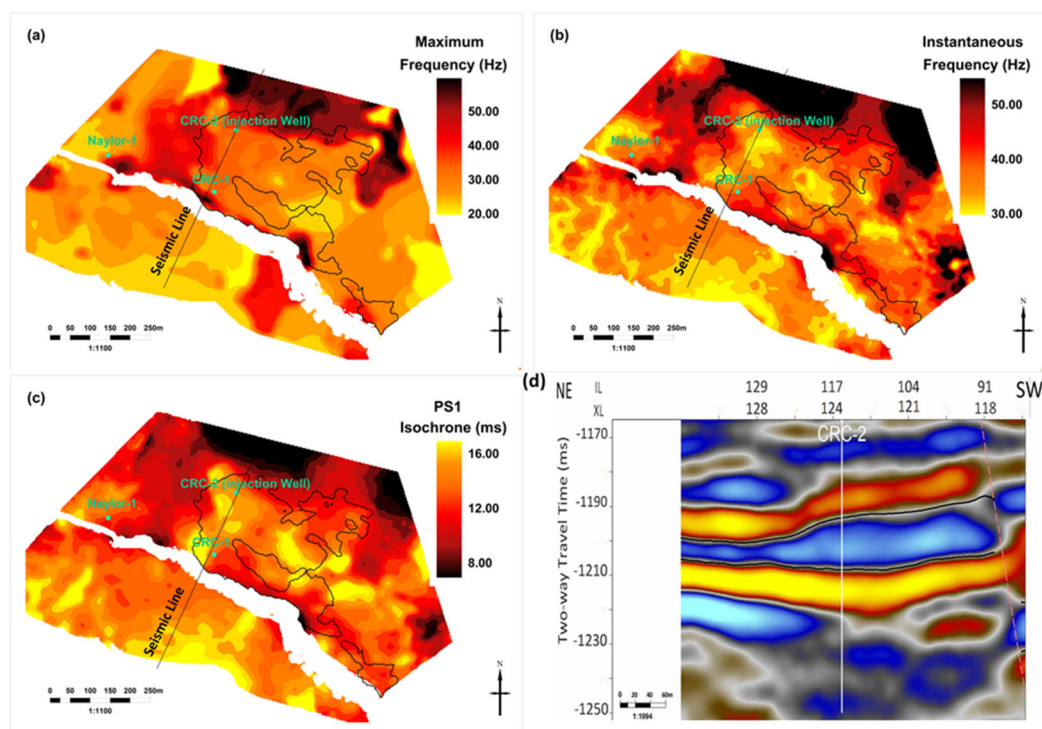


**Figure 5.4** Seismic attributes controlled by the thickness of the injection interval show similar spatial patterns. The example attributes are Maximum Frequency (a), Instantaneous Frequency (b), and PS1 Isochrone (c). The seismic section through the injection well (d) shows the injection interval pinching out to the north (Aldakheel et al., 2021).

### 5.3.4 Non-seismic attributes

In the area shown as a white stripe (referred to as fault shadow) in **Figure 5.5**, the seismic amplitudes are severely distorted due to the presence of the splay fault (see also **Figure 5.5b**). Usually, this area belongs to the footwall of the fault where all the seismic rays that contribute to the image must penetrate through the fault prior to reflection. There are two problems in that zone: first, incorrect kinematic estimates lead to pull-ups and sags. Second, seismic amplitudes are affected by the interaction with the faulted rocks and inaccurate velocity model for the imaging (Fagin, 1996). Hence, all seismic attributes are affected for the part of the CO<sub>2</sub> plume lying in the footwall of the splay fault (**Figure 5.5b**). This issue is related to the abrupt change in the velocity across the fault. As the effect of the fault diminishes away from the fault, we mitigate this issue by considering the distance from the splay fault as an attribute in the input data.

Several non-seismic attributes are also used to incorporate some general understanding of the basic physics of CO<sub>2</sub> migration through reservoir rocks. Distance from the injection well, for instance, reflects the fact that the amount of

CO<sub>2</sub> is limited, and hence the likelihood of CO<sub>2</sub> presence decreases away from the well. Distance from the splay fault was not only considered to correct for the fault shadow zone but it was also considered because faults can create fracture zones, and hence enhance the porosity of the reservoir.

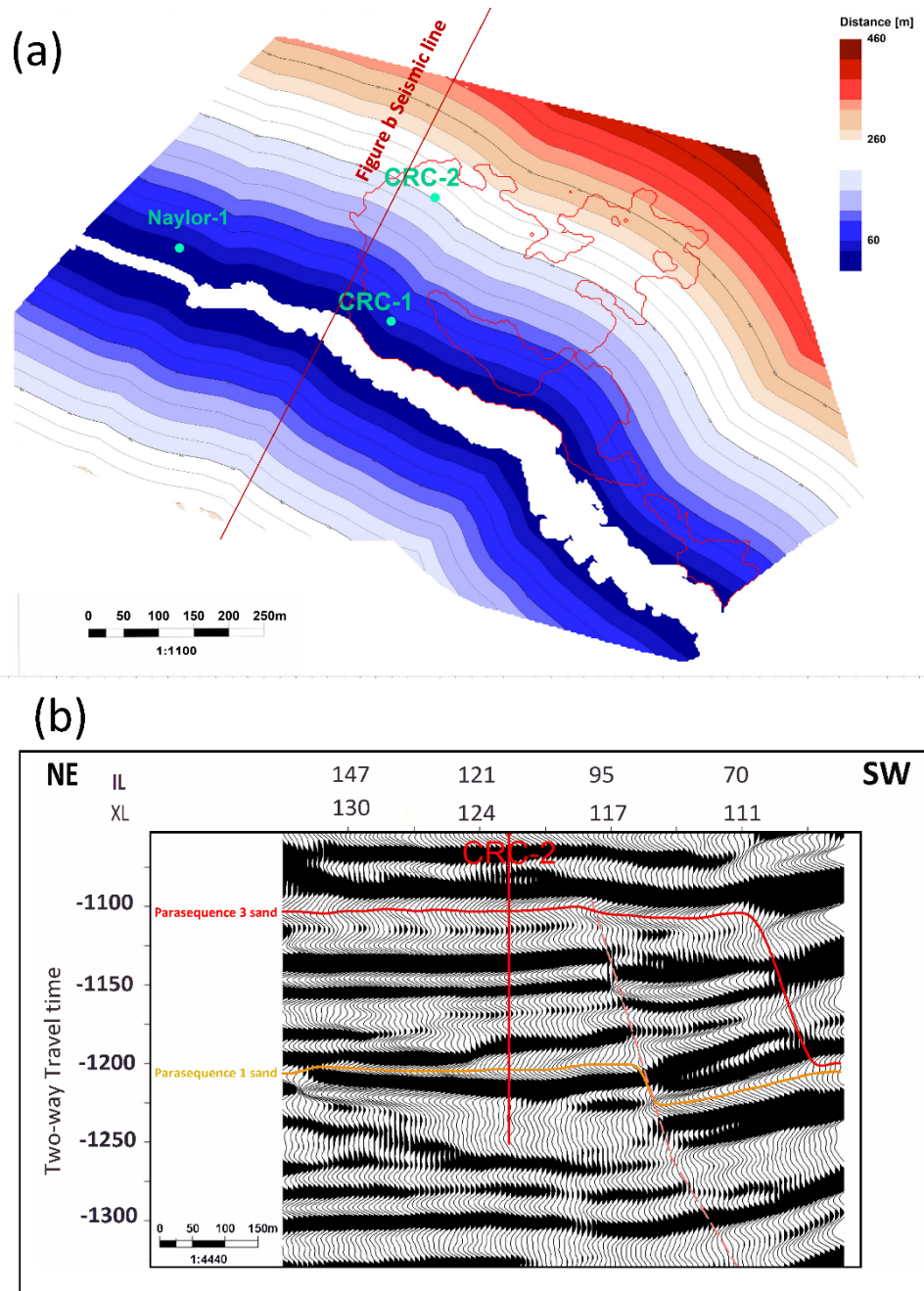


**Figure 5.5** Distance from the splay fault (a) aims to compensate the seismic imaging issues closer to the fault and potentially capture higher permeability of the fractured rocks adjacent to the fault. Blank gap corresponds to a part of the seismic image distorted by the interaction of seismic waves with the splay fault - fault shadow (b) (Aldakheel et al., 2021).

### 5.3.5 Input data selection

Some of the computed attributes are controlled by the same subsurface parameters, and hence their maps look similar. An abundance of closely related features in the training set may lead to a bias in the ANN prediction, and thus, the highly correlated predictive features are removed (**Table 1**) (Aldakheel et al., 2021).

Only one attribute represents any group of highly correlated features, a set of nine distinctive attributes is selected (**Figure 5.6**):

- Injection distance: finite plume.
- Fault distance: fracture intensity and seismic imaging artefacts.
- Top seal topography (TST): buoyancy-driven CO<sub>2</sub> filtration.
- Seismic amplitudes at the top and the base of the reservoir: reservoir properties.
- Fault detect: minor fractured zones.
- Fault transmissivity: configuration of the minor faults that may bound the plume.
- Reflector isochrone: thickness of the reservoir sandstones.
- Fault block: transmissibility of the splay fault.

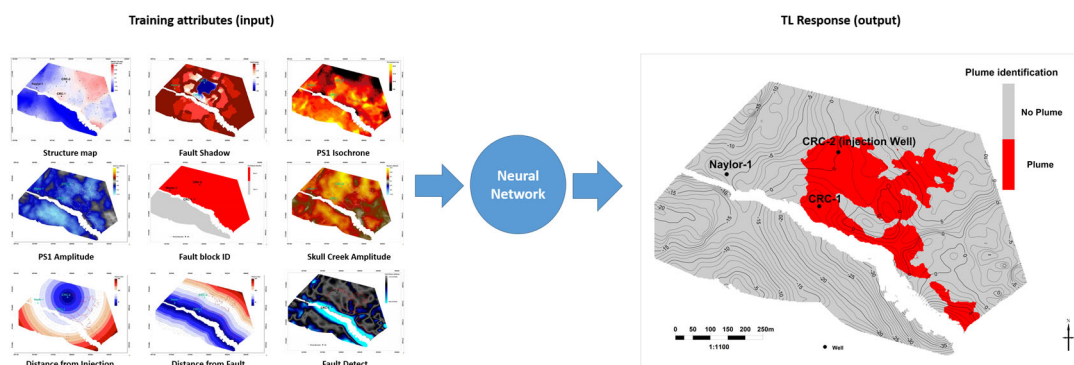


**Figure 5.6** Nine attribute maps that are used as predictive features in the neural network, which is trained to reconstruct the plume shape (Aldakheel et al., 2021).

## Chapter 5: Neural network model building for CO<sub>2</sub> plume characterisation

	Top seal topography	seismic amp reservoir base	PS1 amp	Evelope	[Org.Ampl]	[RmsAmpl]	[Sweet]	[RelAclmp]	Distance from Injction	Fault Transmissivity	Instantaneous frequency	PS1_Isochrone	Maximum Value Frequency	[DomFreq]	Distance from fault	Fault Block identifier	Fault Detect	[Phase]	Time-lapse Response
Top seal topography	1.00	0.23	0.19	0.19	0.19	0.10	0.28	0.26	0.39	0.19	0.43	0.39	0.46	0.43	0.46	0.81	0.28	0.08	0.39
seismic amp reservoir base	0.23	1.00	0.44	0.46	0.44	0.63	0.39	0.50	0.57	0.37	0.24	0.23	0.38	0.26	0.25	0.18	0.31	0.26	0.15
seismic amp reservoir top	0.19	0.44	1.00	1.00	1.00	0.89	0.97	0.82	0.11	0.17	0.26	0.21	0.20	0.30	0.04	0.38	0.19	0.02	0.08
Evelope	0.19	0.46	1.00	1.00	0.99	0.90	0.98	0.84	0.13	0.19	0.25	0.20	0.19	0.29	0.04	0.37	0.19	0.04	0.08
[Org.Ampl]	0.19	0.44	1.00	0.99	1.00	0.89	0.97	0.82	0.11	0.17	0.25	0.21	0.20	0.30	0.04	0.38	0.19	0.02	0.08
[RmsAmpl]	0.10	0.63	0.89	0.90	0.89	1.00	0.86	0.72	0.24	0.18	0.00	0.00	0.05	0.00	0.14	0.32	0.23	0.02	0.03
[Sweet]	0.28	0.39	0.97	0.98	0.97	0.86	1.00	0.89	0.04	0.19	0.43	0.37	0.32	0.45	0.12	0.46	0.16	0.05	0.07
[RelAclmp]	0.26	0.50	0.82	0.84	0.82	0.72	0.89	1.00	0.12	0.27	0.53	0.45	0.35	0.53	0.20	0.37	0.21	0.24	0.07
Distance from Injction	0.39	0.57	0.11	0.13	0.11	0.24	0.04	0.12	1.00	0.54	0.34	0.36	0.42	0.36	0.13	0.46	0.21	0.14	0.38
Fault Transmissivity	0.19	0.37	0.17	0.19	0.17	0.18	0.19	0.27	0.54	1.00	0.10	0.10	0.08	0.08	0.07	0.21	0.09	0.18	0.51
Instantaneous frequency	0.43	0.24	0.26	0.25	0.25	0.00	0.43	0.53	0.34	0.10	1.00	0.91	0.76	0.97	0.44	0.43	0.06	0.11	0.08
PS1_Isochrone	0.39	0.23	0.21	0.20	0.21	0.00	0.37	0.45	0.36	0.10	0.91	1.00	0.72	0.90	0.37	0.43	0.06	0.05	0.08
(Maximum Value Frequency)	0.46	0.38	0.20	0.19	0.20	0.05	0.32	0.35	0.42	0.08	0.76	0.72	1.00	0.77	0.36	0.42	0.01	0.00	0.04
[DomFreq]	0.43	0.26	0.30	0.29	0.30	0.00	0.45	0.53	0.36	0.08	0.97	0.90	0.77	1.00	0.43	0.43	0.05	0.08	0.08
Distance from fault	0.46	0.25	0.04	0.04	0.04	0.14	0.12	0.20	0.13	0.07	0.44	0.37	0.36	0.43	1.00	0.30	0.44	0.08	0.10
Fault Block identifier	0.81	0.18	0.38	0.37	0.38	0.32	0.46	0.37	0.46	0.21	0.43	0.43	0.42	0.43	0.30	1.00	0.16	0.11	0.35
Fault Detect	0.28	0.31	0.19	0.19	0.19	0.23	0.16	0.21	0.21	0.09	0.06	0.06	0.01	0.05	0.44	0.16	1.00	0.06	0.04
[Phase]	0.08	0.26	0.02	0.04	0.02	0.02	0.05	0.24	0.14	0.18	0.11	0.05	0.00	0.08	0.08	0.11	0.06	1.00	0.09
Time-lapse Response	0.39	0.15	0.08	0.08	0.08	0.03	0.07	0.07	0.38	0.51	0.08	0.08	0.04	0.08	0.10	0.35	0.04	0.09	1.00

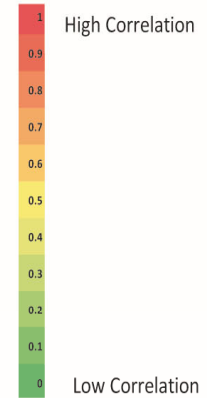


**Table 1** Correlation matrix for a set of the potential attributes (Aldakheel et al., 2021).



## **5.4 The architecture of the prediction algorithm**

ANN has two fundamental parameters that control its performance: number of neurons in the hidden layer and number of iterations during training. A naïve approach to the optimisation of an ANN design may rely on the training error only, but this metric may be misleading because it shows how well ANN can memorize the data. In this case, the network would likely suffer from overfitting as it attempts to capture every subtle feature in the observed CO<sub>2</sub> plume that may be due to noise in the data. To reduce the sensitivity of an ANN to the noise, one needs to choose the number of iterations and the number of neurons that provide both sufficiently low training error and high prediction accuracy. A common approach to estimate the prediction error is cross-validation, which involves randomly removing a test set – a subset of the input data - from the training process. Traditionally, the test set is picked randomly based on the assumption that each sample represents a realisation of identical but independent distributions. This assumption fails for the maps of a seismic attribute because seismic amplitudes are smeared due to the limited lateral resolution and continuity of geological features. As a result, test samples could be easily predicted by the values in the adjacent training points.

Hence, at each iteration of training, a set of extended patches with dimensions comparable with the correlation radius must be removed from the seismic maps. To make the test sets independent, the test patches are spaced by at least two Fresnel zones. We performed ten test runs of the ANN training with approximately 20% of the reservoir used for the test error estimation.

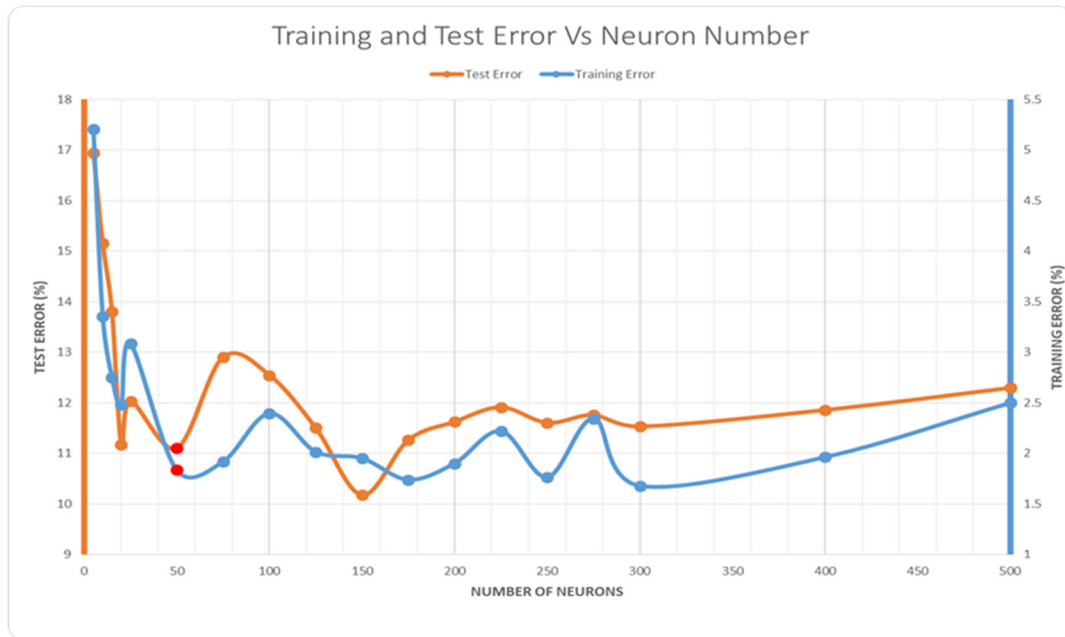


**Figure 5.7** Optimisation of the neural network algorithm. Average training (blue) and test error (orange) for ten tests allows finding a balance between the complexity of the prediction algorithm and its tendency to overfit the noise (Aldakheel et al., 2021).

**Figure 5.7** shows the average training and test errors of the ten tests against the number of neurons used in each model. A dramatic decrease in both the training and test errors can be observed from 5-50 neurons. Increasing the number past 50 neurons appears to have only a minor effect on the accuracy of the model. Using 50 neurons is thus an optimal choice. The ANN with 50 neurons reconstructs the CO<sub>2</sub> plume with an average training error of  $1.85 \pm 0.50$  % and average test error of  $11.1 \pm 3.43$  % with the error concentrated at the edge of the plume (see **Figure 5.8a&b**). The misclassified samples during the training are located within 12 m with a standard deviation of 2.25 m. In the test set, these values are 44 m and 7.86 m, respectively (**Figure 5.9**).

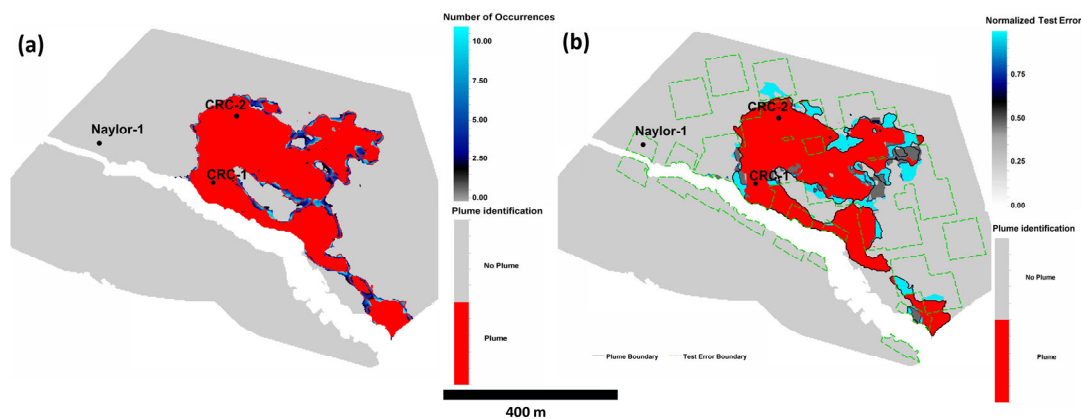


**Figure 5.8** Spatial distribution of the prediction errors by the neural network. The CO<sub>2</sub> plume overlaid by the number of misclassified samples on the training set (a) and ten test patches (b) (Aldakheel et al., 2021).

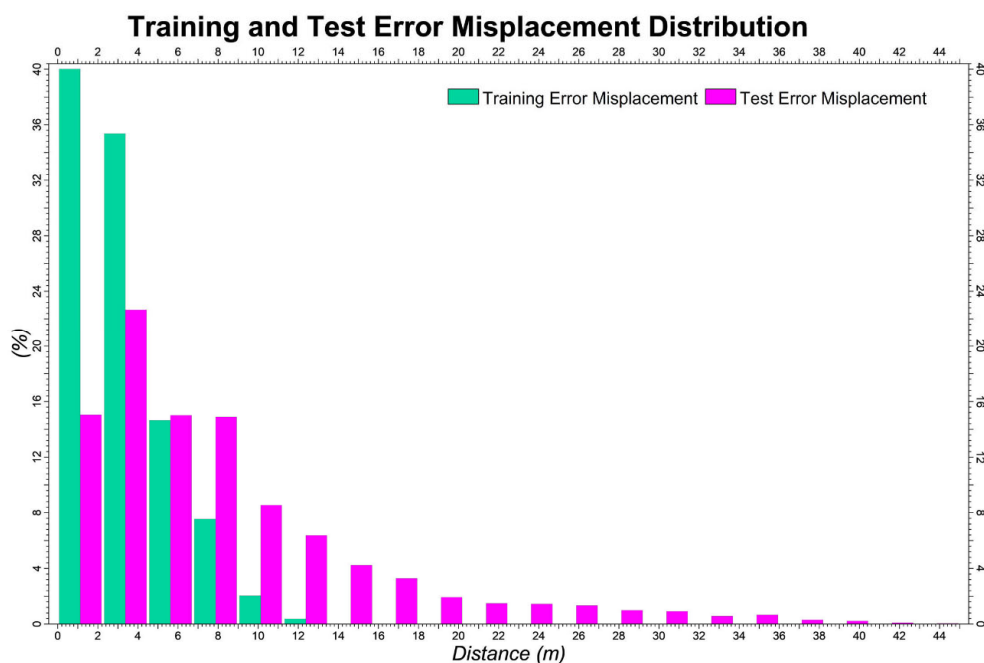


**Figure 5.9** Distribution of the prediction error relative to the distance to the CO<sub>2</sub> plume edge (Aldakheel et al., 2021).

## 5.5 Summary

In this chapter, an attempt was made to quantify the seismic attributes that can represent the geological features which control the CO<sub>2</sub> migration process in Stage 2C. The ANN was used to form a direct link between all the potential attributes and the observed TL response due to the injection. This ANN model will be used in the next chapter to highlight the importance of each attribute in the migration process, and it will be used to predict the behaviour of the CO<sub>2</sub> migration in Stage 3.

The main findings in this chapter are:

1. Nine attributes were chosen to represent the CO<sub>2</sub> migration process.
2. To measure the ability of this model to predict unseen data, a number of test areas were excluded from the input data during training of the ANN model.
3. The ANN model was able to reconstruct the TL response due to the CO<sub>2</sub> injection with an average training error of  $1.85 \pm 0.50$  % and average test error of  $11.1 \pm 3.43$  % with the error concentrated at the edge of the plume.
4. The optimal complexity of the ANN model was 50 neurons as higher complexity models show only minor improvement in the reconstruction of the plume. Complex models have a risk of overfitting to the training data set.

## **Chapter 6**

# **Artificial Neural Network model analysis and application**

This chapter will analyse the results of the ANN model created in the previous chapter. The fact that the model can reconstruct the CO<sub>2</sub> plume with decent accuracy suggests that the input data is able to predict the final distribution of the CO<sub>2</sub> plume. Here, a series of tests were performed to quantify the importance of each attribute for characterising the CO<sub>2</sub> migration process. possible application for this model is also discussed (Aldakheel et al., 2021).

### **6.1 Information value of the attributes**

The optimised ANN can provide a quantitative estimate of the importance of a particular attribute for the accurate reconstruction of the CO<sub>2</sub> plume. A general approach to the problem is to compare the accuracy changes when a particular attribute is taken in/out of the set of predictive features. There are two commonly-used approaches to this problem: leave-one-out cross-validation and permutation test (James et al., 2013).

### 6.1.1 Leave-one-out

This approach starts with a full set of predictive features and then compares the prediction accuracy for ANN trained with and without one of the features. The higher the error increases, the more important this attribute is. In **Figure 6.1a**, the highest impact belongs to the distance from the injector, the distance from the splay fault and the top seal topography. At the same time, the least important features are the fault block, the amplitude at the bottom of the reservoir and the fault detect attribute.

### 6.1.2 Permutation test

Instead of excluding a particular attribute, in the permutation test spatial distribution of values for an attribute - value locations - is randomised across the area to quantify by how much this randomisation affects the prediction error. Unlike the leave-one-out approach, the training relies on all the attributes. So, the permutation test aims to show how well an ANN can predict the plume when an attribute is available. While the leave-one-out cross-validation indicates to which extent a network can compensate for the absence of the attribute. **Figure 6.1** shows that the two methods provided similar results: the most and least important features are the same. This was to be expected since the two methods are closely related.

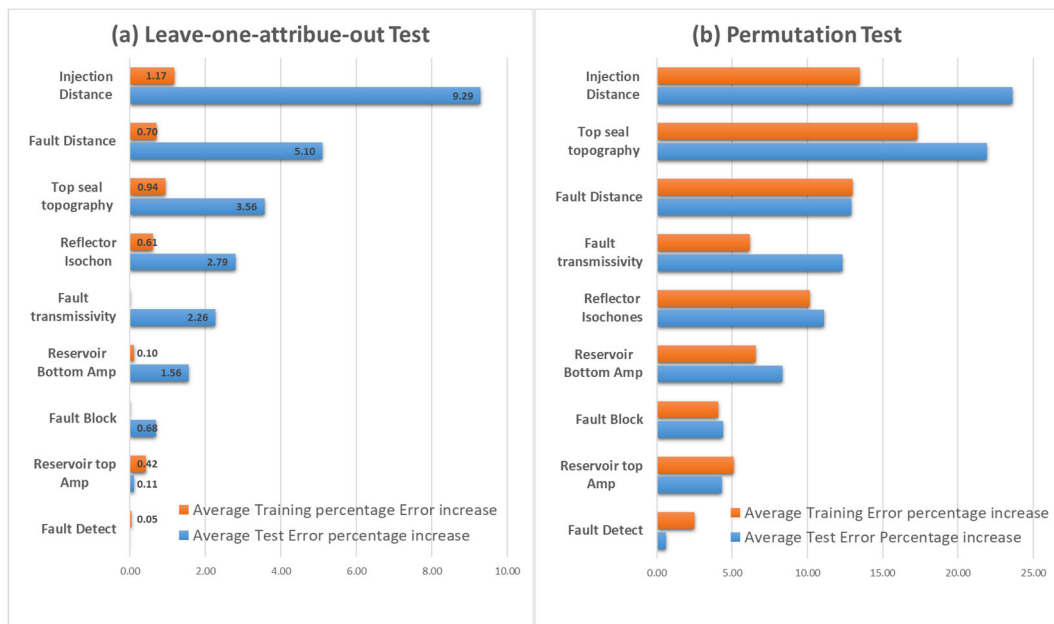


**Figure 6.1** Predictive feature importance. Training and test error variation when one attribute is excluded from training the ANN model (a) Predictive feature importance. Training and test error variation when one attribute is shuffled in the reconstruction (b) (Aldakheel et al., 2021).

### 6.1.3 Input data categories

According to the spatial distribution of the permutation test error, the attributes are divided into two categories: global and local. For instance, **Figure 6.2a** shows the CO<sub>2</sub> plume reconstruction when the top seal topography is randomised. The misclassified samples are evenly distributed over the entire reservoir. On the other hand, randomising the amplitude at the base of the reservoir leads to only small streaks of misclassified samples at the eastern and western edges of the plume (**Figure 6.2b**). **Figure 6.2c** shows the distribution of these errors versus the strength of the TL seismic response. We see that the global attribute has high values everywhere, while the local attribute is high only in the vicinity of the threshold that separates the plume/no-plume samples. This observation indicates that the local attributes become important where the time-lapse signal is low. Even though for some attributes the overall area of misclassified samples is small, this area may be localised in specific parts of the plume, and hence it is essential to keep these attributes in the input.

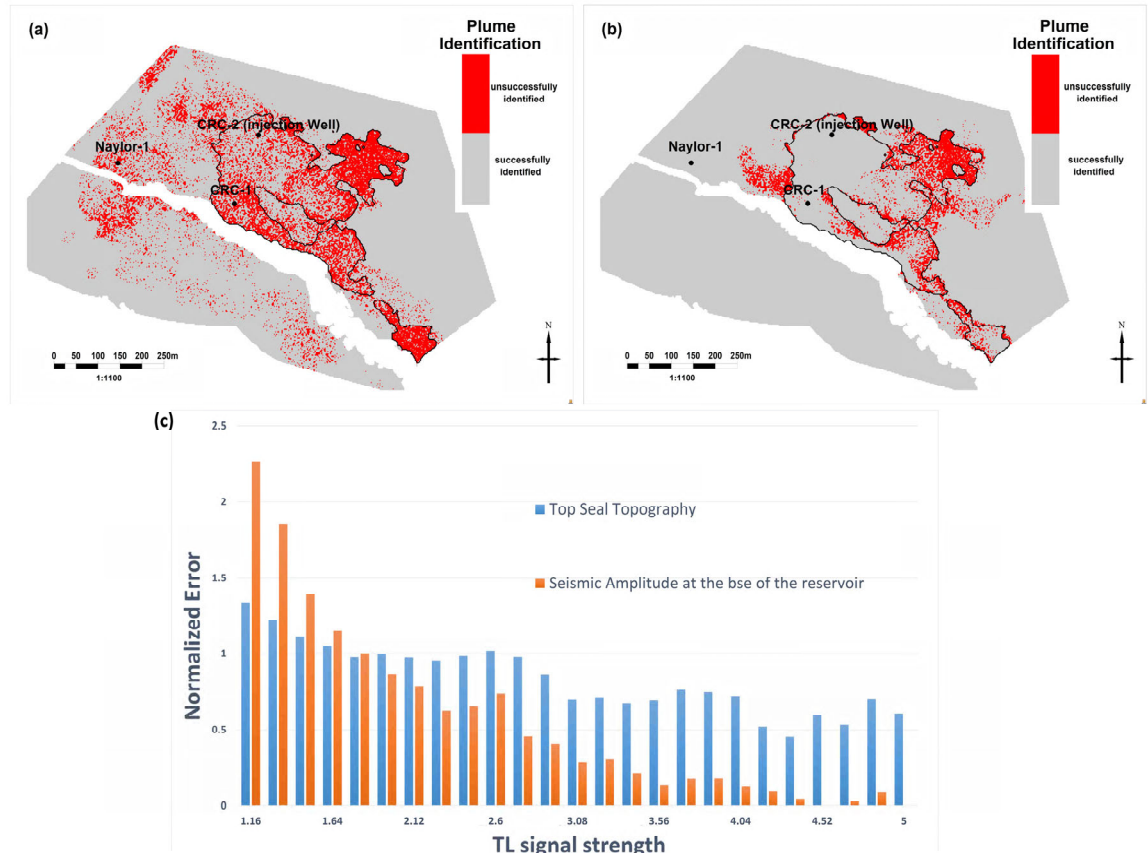


**Figure 6.2** Spatial error distribution for the permutation test. When the top seal topography is perturbed, the error is evenly distributed throughout the map (a), which indicates that this attribute is important everywhere at the injection interval. When the amplitude of the reflection from the bottom of the reservoir is perturbed (b), the error concentrates in a few areas. The relationship of the error distribution to the strength of the time-lapse signal (c) confirms the general/localised importance of these attributes (Aldakheel et al., 2021).

### 6.1.4 Capturing the CO<sub>2</sub> migration process

An advantage of the permutation test is its ability to analyse the spatial distribution of the plume after randomisation. The map of the reconstructed plume after the randomisation of a certain attribute can highlight where within the plume this attribute is contributing to the reconstruction and whether the attribute is tackling the migration process that it was intended to tackle. This section will review all the migration process components that the input data is capturing.

#### 6.1.4.1 Buoyancy driven migration

As established earlier, the CO<sub>2</sub> migration process is driven by buoyancy. The dramatic increase in the error when either the topography of the reservoir is excluded or randomised supports migration mechanism. Since it is tricky to randomise the top reservoir topography because the model is assuming that the topography is



independent attribute where in reality it is not as it depends on the location of any given point, the distance from the injection is considered to mitigate this issue.

**Figure 6.3** shows a reconstructed plume after randomising the reservoir topography.

The way the plume appears in this map has the following implications:

1. The likelihood of the plume to exist outside the imaged plume boundary after randomisation is high which is supporting the fact that the plume is driven by buoyancy.
2. The absence of the plume in Zone 1 (**Figure 6.3**) indicates that the reservoir cannot accommodate the CO<sub>2</sub> due to changing lithology since this zone was populated with CO<sub>2</sub> when PS1 isochrone was shuffled which was used as a proxy for sand bodies (**Figure 6.4**).
3. The absence of plume in Zone 2 is probably because of its long distance from the injection well.

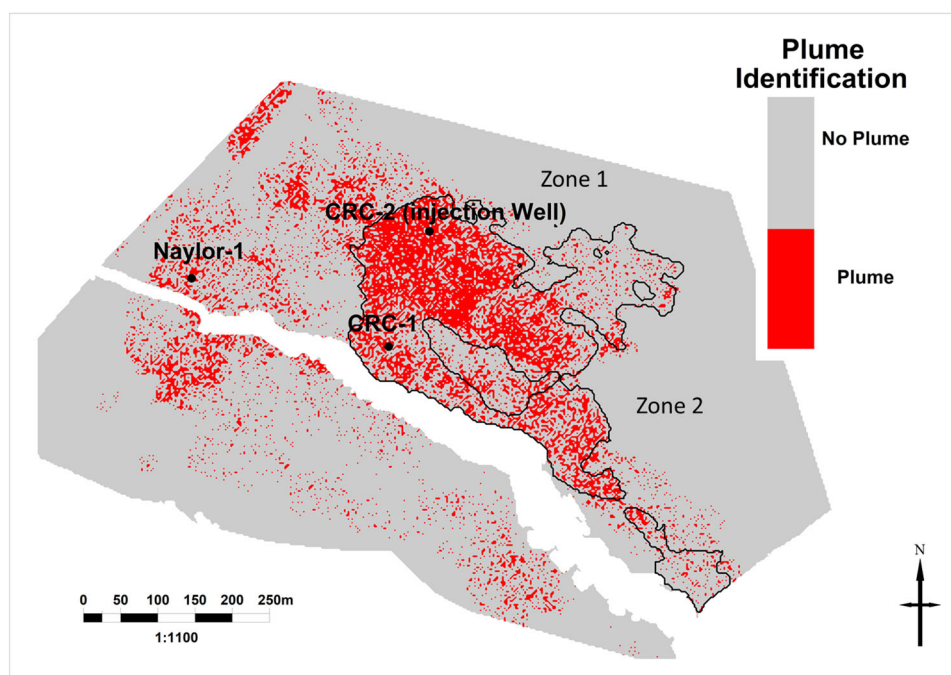


**Figure 6.3** CO<sub>2</sub> reconstruction after the randomisation of the top topography.

### 6.1.4.2 Reservoir quality (lithology)

Frequency-based attributes can be indicative of sand bodies and lithological heterogeneity. The reliance of the model on the PS1 reflector isochron as illustrated in **Figure 6.1** was high, which supports the ability of this attribute to predict the lithology of PS1. In **Figure 6.3**, when the reservoir topography was randomised,

Zone 1 has no predicted CO<sub>2</sub>. This zone is structurally higher than the injection well. hence, CO<sub>2</sub> can migrate in that direction, but it has not. A possible reason is the lack of reservoir rock in that area. To validate this scenario, the plume was reconstructed with randomized PS1 isochron attribute (**Figure 6.4**). Zone 1 seems to have reconstructed much of CO<sub>2</sub> plume after the randomization process, which indicates that this area is a shaly zone. The randomization is also affecting other parts of the plume, which indicates that the frequency-based attribute is very crucial in predicting the lithology of PS1.

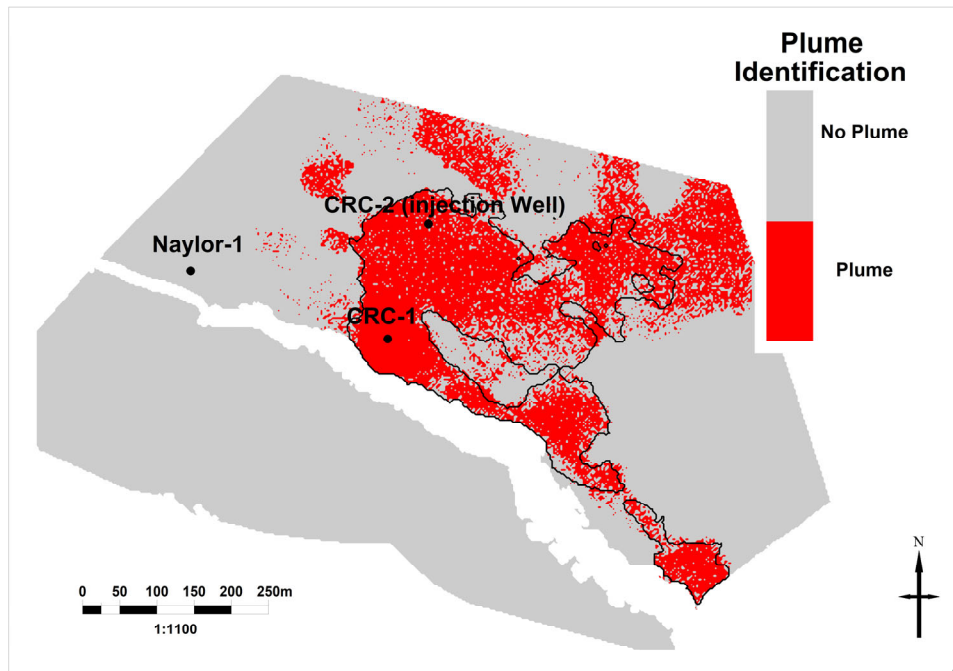


**Figure 6.4** CO<sub>2</sub> reconstruction after the randomisation of the frequency-based attribute (PS1 reflector isochron).

### 6.1.4.3 Reservoir quality (porosity)

Both the amplitudes at the top and the base of the reservoir were part of the input data to account for the changes in porosity and thickness. Those attributes are only activated if the reservoir rock exists as indicated by frequency-based attributes (PS1 reflector isochrone). Since this model is constructed to predict the existence of the plume rather than the time-lapse response after introducing the cut-off, their contribution became limited as illustrated in **Figure 6.1**. **Figure 6.5** shows the reconstructed plume after randomizing the top and the base amplitudes. Within the boundary of the imaged plume, the effect of the randomization appears to take place away from the injection well as the likelihood of the existence of the plume

diminishes and minor changes in the porosity become more important. There are some areas where reconstructed CO<sub>2</sub> appears outside the imaged boundary where this attribute indicates contrast in acoustic impedance, which could be caused by changes in porosity within the reservoir rock as both the overlaying and underlaying layers are considered to be homogenous. Hence, this attribute is likely predicting low porosity, which prevented the migration of CO<sub>2</sub> in those areas.

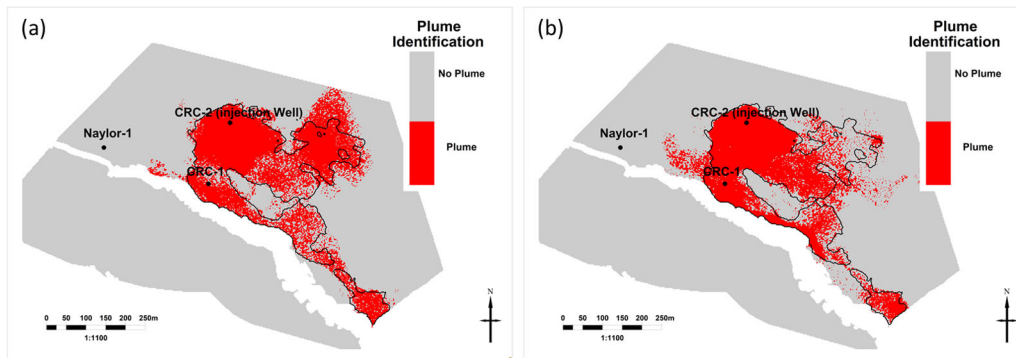


**Figure 6.5** CO<sub>2</sub> reconstruction after the randomisation of the seismic amplitude at the top of the reservoir (a) and the base (b).

### 6.1.4.4 Faulting as a flow barrier

To account for the effect of faulting as flow barriers in the CO<sub>2</sub> migration process, two attributes were considered. First, the fault block identifier, which separates the area into two: footwall and hanging wall. This attribute accounts for the possibility of the CO<sub>2</sub> to migrate across the splay fault. In **Figure 6.3**, CO<sub>2</sub> was reconstructed in the hanging wall to the south after randomizing the reservoir topography. This indicates that the fault identifier is not preventing CO<sub>2</sub> from migrating across the fault. To validate this conclusion, we perform the same randomisation process on the fault identifier attribute in **Figure 6.6**, where CO<sub>2</sub> is not observed across the fault.

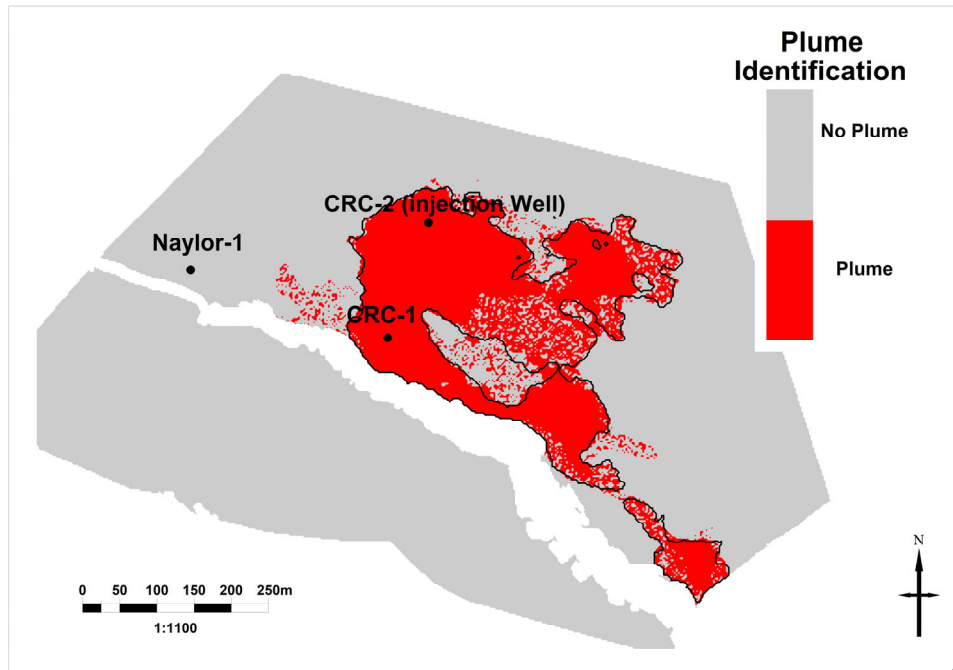


**Figure 6.6** CO<sub>2</sub> reconstruction after the randomisation of fault-block identifier.

The second attribute that was considered to account for faults as flow barriers is the fault transmissivity attribute. **Figure 6.7** shows the prediction of CO<sub>2</sub> when the fault transmissivity attribute is randomised. This attribute seems to control the high concentration of CO<sub>2</sub> around the plume (zone 1) as the prediction error seems to be high. In Zone 2, there are some reconstructed CO<sub>2</sub> where the imaged plume indicates the absence of CO<sub>2</sub> in this area. This finding suggests that the absence of the plume in this area is due to minor faulting within PS1.

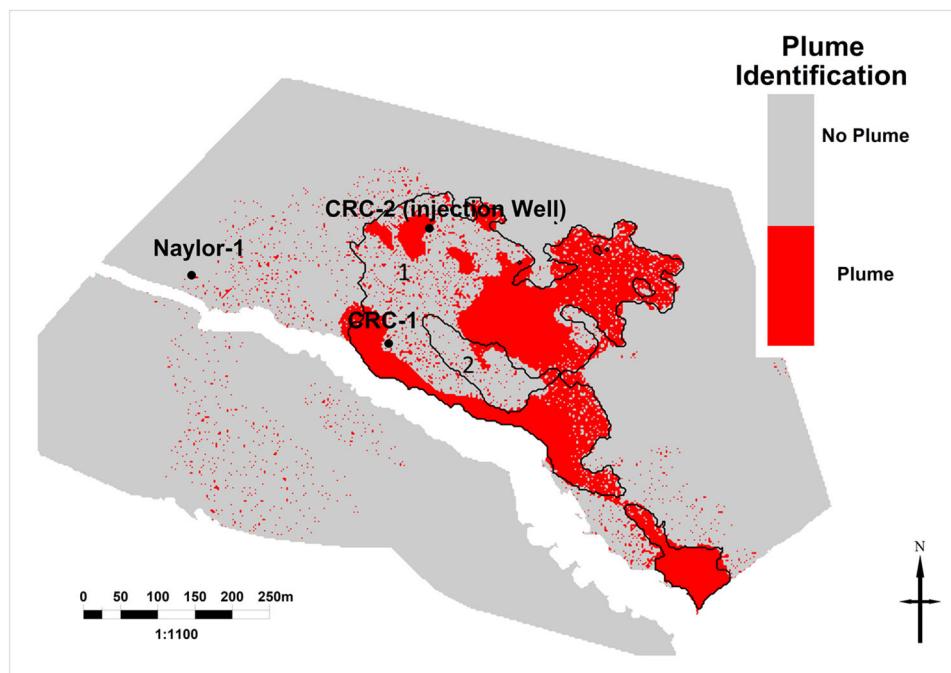


**Figure 6.7** CO<sub>2</sub> reconstruction after the randomisation of the fault transmissivity attribute.

### 6.1.5 ANN model implications and geological interpretation

The importance of the features has a clear geological interpretation:

- CO<sub>2</sub> movement is driven by buoyancy as the top seal topography (TST attribute) contribution to the model is high.
- As we move away from the injection, the likelihood of CO<sub>2</sub> presence decreases.
- The distance from the splay fault attribute 'corrects' all the attributes due to deterioration of the seismic signal near faults.
- The reservoir reflector isochrons attribute is a good proxy for the lithology of reservoir rocks.
- The fault transmissivity attribute predicts the likelihood of the CO<sub>2</sub> existence across minor faults.

## 6.2 Application to reservoir simulations

As discussed earlier, post-injection fluid flow simulations were unable to reproduce the extent of the CO<sub>2</sub> plume in several areas. However, the ANN prediction matches the seismic plume reasonably well. Thus, the permutation tests can be a tool to examine what geological features or attributes may be responsible for the mismatch between flow simulations and the seismic plume.

**Figure 6.8** compares the simulated and observed plumes and indicates where the attribute are controlling the reconstruction of the plume in the areas with poor history match. These attributes have a clear geological interpretation, so the geological modelling may be guided by these results. For example, the seismic plume appears to be bounded to the north-east from CRC-2, where the isochrone attribute (corresponding to the temporal thickness of the reservoir) is low despite structural high in that area. This may indicate a sandstone transition into a shaly unit with very low permeability.

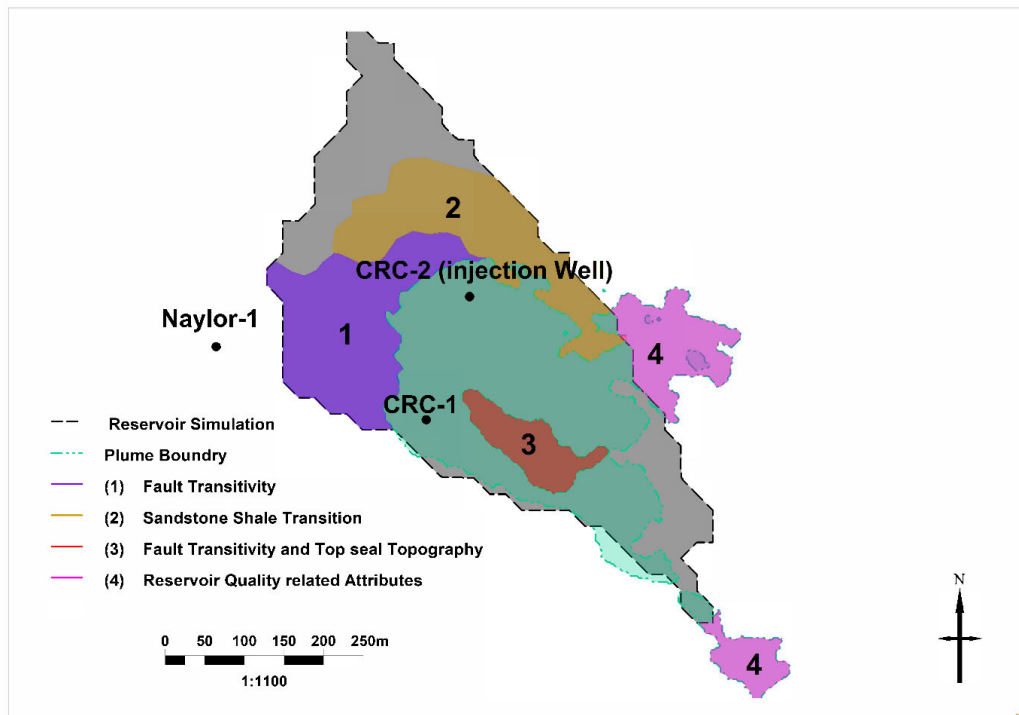


**Figure 6.8** Spatial distribution of the attribute importance. Areas, where the physics-based reservoir simulation deviate from the actual plume shape, are named/coloured according to the controlling geological feature as highlighted by the neural network analysis (Aldakheel et al., 2021).

Another useful application of the trained ANN model is the prediction of the shape of the Stage 3 injection. The Stage 3 injection well, CRC-3, is located in the area where the Stage 2C seismic vintages have a low fold. Therefore, the developed ANN architecture was applied to the Extended M5 and Nirranda 3D regional surveys. The fully trained ANN may be directly applied to the predictive features computed for the Extended M5 because this vintage is very similar to the original Stage 2C seismic in the areas with similar seismic fold. Conversely, for the Nirranda 3D vintage, differences in acquisition and processing parameters affected not only the

amplitudes but also the structural framework. Hence, the ANN algorithm was we trained afresh using the seismic plume shape from 2C vintages but the predictive features from the Nirranda 3D vintage. Training and testing errors for Nirranda 3D are relatively close to the values for the Stage 2C seismic, 1.6% and 16%, respectively; hence ANN is applicable to the larger seismic.

**Figure 6.9a** shows the map of the likelihood of CO<sub>2</sub> presence in the Stage 3 injection predicted from the Extended M5 survey. This map is obtained from ten training runs with different random seeds for the initialisation of the ANN parameters. **Figure 6.9b** presents a similar map applied to attributes computed from the regional seismic (Nirranda 3D). The results from the analysis based on the two surveys are somewhat different. One source of the differences is that the Extended M5 survey images the subsurface containing the Stage 2C plume. Yet, despite these differences, the predicted plumes share some important features: a prominent up-dip migration along the fault and an across-the-fault leakage in the vicinity of the Naylor-1 well. The former finding is consistent with the results of Stage 3 reservoir simulations, while the latter indicates a potential risk that should be assessed by the reservoir modelling team.

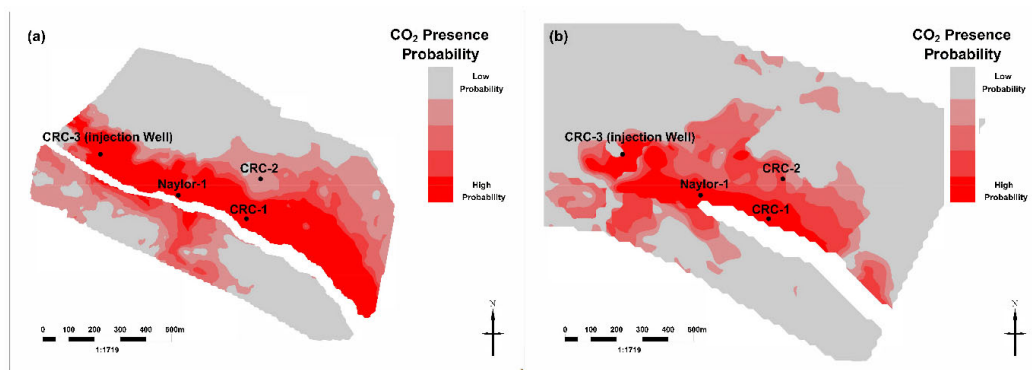


**Figure 6.9** Application of the trained neural network to the prediction of the plume shape in Stage 3 of the Otway Project. The probability of CO<sub>2</sub> occurrence using the Extended Monitor 5 survey and the large regional Nirranda 3D survey (b) (Aldakheel et al., 2021).

### 6.3 Summary

In this chapter, the optimised ANN model from Chapter 5 will be utilized in two different ways: quantified the importance of the geological features in the CO<sub>2</sub> migration process and attempted to forecast the plume migration in Stage 3.

The key findings are:

1. A shallow artificial neural network provides a useful tool for evaluation of the information value in each attribute and its geological representation.
2. The ANN model was able to reconstruct the Stage 2C plumes with high accuracy based on a suite of seismic attributes. Thus, forecasting Stage 3 injection is plausible since both stages are comparable in injection size.
3. This method is not a substitute for a detailed static and simulation modelling; however, it can be used to highlight geological and petrophysical features that such models should consider.



# Chapter 7

## Discussion and conclusion

### 7.1 Discussion

This study uses an ANN of simple pixel-based architecture. Current computer vision technology is mostly based on convolutional ANNs, which demonstrated their remarkable success in the ImageNet challenge (Krizhevsky et al., 2017). A potential benefit of the convolutional networks for this study would be their natural ability to deal with spatially correlated seismic maps. However, the ANN design was kept as simple as possible to reduce the overfitting because convolutional filters require determination of a larger number of coefficients during training – a challenging task with only one set of training images (Stage 2C seismic vintages). The proposed simple ANN can be replaced by another relatively unsophisticated classifier, such as logistic regression, random forest (Hastie et al., 2013).

With a more extensive data set, more advanced models can be used, such as generative adversarial networks (Goodfellow et al., 2014). Such a data set may be obtained from extensive reservoir simulations. Another option is to compile the seismic monitoring data from various CO<sub>2</sub> storage sites, which may become possible if CCS data are shared, following the example set by Sleipner (<https://co2datashare.org/dataset/sleipner-4d-seismic-dataset>), provided that the number of training datasets is greater than the number of geological settings.

## Chapter 7: Discussion and conclusion

---

A more promising approach may be implemented for large commercial CO<sub>2</sub> storages. Prior to the commencement of an industrial scale injection operation, several trial injections may help the site operator to calibrate the reservoir models and hence de-risk the project. The proposed ANN-based workflow applied to the monitoring data from these trial injections may significantly contribute to the safety of long-term CO<sub>2</sub> storage.

There are more than fifty distinct seismic attributes that can characterise the subsurface (Chopra and Marfurt, 2005). However, there is a risk of overfitting the input data when utilizing machine learning algorithms, especially when the input data pool of attributes is large (Hall, 1999). For this reason, the input data selection relied on our understanding of the migration process to limit the number of potential input features.

Although impedance-derived porosity derivation is a common practice in seismic characterisation workflows (Avseth et al., 2005), utilising this method was for several reasons. First, this method is proposed as a pre-screening workflow to improve the simulation models in a timely manner. Seismic attribute extraction from post-stack volumes is a fast way to characterise the reservoir in contrasting to seismic inversion and rock physics modelling building. Secondly, the presence of highly reflective cemented sandstone affects the rock physics model ability to derive porosity from seismic properties (Caspari et al., 2015; Dance and Glubokovskikh, 2017). Instead, the direct measurement of the seismic amplitude from the top and the base of the reservoir to infer porosity was incorporated which can also account for the effect of tuning.

An extension of this study would incorporate the time and the injection volume components of the injection process by considering the progression of the time-lapse images. This can be achieved by training the ANN model with each time-lapse image, with each model represents the response of the time-lapse at each injection volume/time. Moreover, the plume/no-plume TL seismic response cut-off can be manipulated to see if it has a relationship with the injected volume. If such a relationship exists, multiple time/volume steps can be generated to train the model which will make it capable of predicting the volume and the timeline Those models

## Chapter 7: Discussion and conclusion

---

can be used to determine the time needed for a future injection to be stabilized or an injection with different injection size

Many attributes were used to capture the migration process within the Parratte Formation where the analysis showed high contribution to certain attributes and low for the rest. The distance from the injection along with the top seal topography seems to dictate the chance of occurrence of CO<sub>2</sub> within the reservoir. The Distance from the fault was also a dominant contributor which was considered in the ANN model for two reasons. (1) to account for the possibility of secondary porosity created by faults-induced fractures and (2) to account for the deterioration of the seismic quality near the fault. This attribute seems to be correcting all the attributes near the fault as the effect of porosity seems to be limited because TL response was categorized to either plume or no plume which means the TL response from thick column of CO<sub>2</sub> or highly saturated interval is equivalent to thin column or low saturation interval as long as the TL response generated is above the cut-off. The contribution from porosity related attributes such as amplitude which may quantify the potential saturation or thickness of the CO<sub>2</sub> column is limited to only distinguish between reservoir and no-reservoir reservoir. Two attributes (Fault block identifier and fault transmittivity) were used to characterize the Naylor south fault ability to trap the CO<sub>2</sub>. When the top topography of the reservoir was randomised, some CO<sub>2</sub> can be observed across the fault. This is an indication of the inability of this fault to trap the injected CO<sub>2</sub>. However, you can argue that the reason of the occurrence of CO<sub>2</sub> across the fault is the fact that there is a great offset created by this fault. The ability of the fault to trap the CO<sub>2</sub> remains inconclusive. Frequency-based attributes seem to perform well in highlighting non-reservoir internals (shale) based on their contribution in the over-all increase in the error when they were discarded from the ANN model. This conclusion is alighting with the finding found in literature.

In this thesis, two methods were used to gauge the contribution of attributes in the migration process. The first method was the leave-one-out and the second method was the permutation method. Although both methods highlight the contribution of each attribute in a similar manner, the leave-one-out method differs fundamentally because the ANN model tries to adapt the model to reconstruct the CO<sub>2</sub> response without a certain attribute. The utilization of both methods elevates the confidence in drawing conclusions.

Seismic imaging will always have resolution limitations. Hence, using seismic techniques to characterise the subsurface will fail to detect some subtle geological or dynamic features. Although seismic attributes are used to highlight such abnormalities, it will still inherit the limitations in the imaging resolution.

### 7.2 Conclusions

A workflow has been developed for identification of reservoir features that control CO<sub>2</sub> plume shape (using the time-lapse seismic data as a calibration). While any history-matching procedure aims to build a reservoir model that matches both baseline seismic images and observed time-lapse seismic anomalies, existing workflows often rely on subjective judgement and intuition of a reservoir modelling team. Using a monitoring data set from a real injection of supercritical CO<sub>2</sub>, Stage 2C of the CO<sub>2</sub>CRC Otway Project, it has been shown that a simple neural network provides a means for ‘calibration’ of the seismic reservoir characterisation and observed CO<sub>2</sub> plume shapes.

A set of seismic attributes have been identified that are likely to control the migration process of CO<sub>2</sub> using the time-lapse seismic survey. First, a set of potentially useful predictive features were generated: candidate attributes that may highlight reservoir extent (temporal thickness, reservoir topography, distribution of minor faults etc.), quality of the seismic data (distance from a major fault) and capture some basic features of the fluid flow (distance from the injection well). Second, a shallow artificial neural network was used to create a link between those attributes and the final shape of the CO<sub>2</sub> plume obtained from the last time-lapse image. Once the network was able to reconstruct the observed plume with sufficient accuracy, it was used to gauge the importance of each attribute. It was assumed that the most important attribute has the highest contribution to the accuracy of the prediction. Two methods to quantify the contribution of each attribute were utilized: (1) leave one out and (2) permutation test method. Both methods give similar results. The permutation test method was also used to identify a set of attributes that should drive the geological modelling to match the observed and simulated CO<sub>2</sub> plume.

## Chapter 7: Discussion and conclusion

---

Since the neural network was able to accurately reconstruct the Stage 2C plume, an attempt was made to forecast the plume arising from a future Stage 3 injection, which will occur into the same formation 700 m away from Stage 2C injection. In general, the predicted map of the probability of the occurrence of CO<sub>2</sub> after the Stage 3 injection looks reasonable and agrees with existing reservoir simulations.

However, the neural network predicts some potential risks (e.g., across the fault migration) that were not considered in the fluid flow simulations. Although the neural network cannot fully replace high-fidelity fluid flow simulations, it can be used to highlight the geological and petrophysical scenarios that should be simulated. Hence, the proposed workflow may improve significantly both efficiency and accuracy of future history-matching studies.



# References

- Aldakheel, M., R. Pevzner, B. Gurevich, and S. Glubokovskikh, 2021, Seismic Characterization of a CO<sub>2</sub> Storage Driven by Time-Lapse Images of a Prior Injection using Artificial Neural Network: Interpretation, **9**, 1-47.
- Avseth, P., T. Mukerji, and G. Mavko, 2005, Quantitative Seismic Interpretation : Applying Rock Physics Tools to Reduce Interpretation Risk: Cambridge University Press.
- Bagheri, M., R. Pevzner, C. Jenkins, M. Raab, P. Barraclough, M. Watson, and T. Dance, 2020, Technical de-risking of a demonstration CCUS project for final investment decision in Australia: The APPEA Journal, **60**, 282-295.
- Bahorich, M., and S. Farmer, 1995, 3-D seismic discontinuity for faults and stratigraphic features: The coherence cube: The Leading Edge, **14**, 1053-1058.
- Bauer, R. A., R. Will, S. E. Greenberg, and S. G. Whittaker, 2019, Illinois Basin–Decatur Project, *in* Wilson, M., M. Landrø and T. L. Davis, eds., Geophysics and Geosequestration: Cambridge University Press, 339-370.
- Bryant, S. L., S. Lakshminarasimhan, and G. A. Pope, 2006, Buoyancy-Dominated Multiphase Flow and Its Impact on Geological Sequestration of CO<sub>2</sub>: Presented at the SPE/DOE Symposium on Improved Oil Recovery, Society of Petroleum Engineers.
- Caspari, E., R. Pevzner, B. Gurevich, T. Dance, J. Ennis-King, Y. Cinar, and M. Lebedev, 2015, Feasibility of CO<sub>2</sub> plume detection using 4D seismic: CO<sub>2</sub>CRC Otway Project case study — Part 1: Rock-physics modeling: GEOPHYSICS, **80**, B95-B104.
- Chadwick, R., R. Arts, M. Bentham, O. Eiken, S. Holloway, G. Kirby, J. Pearce, J. Williamson, and P. Zweigel, 2009, Review of monitoring issues and technologies associated with the long-term underground storage of carbon dioxide: Geological Society, London, Special Publications, **313**, 257-275.
- Chadwick, R., P. Zweigel, U. Gregersen, G. Kirby, S. Holloway, and P. Johannessen, 2004, Geological reservoir characterization of a CO<sub>2</sub> storage site: The Utsira Sand, Sleipner, northern North Sea: Energy, **29**, 1371-1381.

## References

---

- Chadwick, R. A., and D. J. Noy, 2015, Underground CO<sub>2</sub> storage: demonstrating regulatory conformance by convergence of history-matched modeled and observed CO<sub>2</sub> plume behavior using Sleipner time-lapse seismics: *Greenhouse Gases: Science and Technology*, **5**, 305-322.
- Chopra, S., and K. J. Marfurt, 2005, Seismic attributes—A historical perspective: *GEOPHYSICS*, **70**, 3SO-28SO.
- Chopra, S., and K. J. Marfurt, 2007, *Seismic attributes for prospect identification and reservoir characterization*: Society of Exploration Geophysicists.
- CO2CRC, 2020, *Map of the Otway National Research Facility (ONRF)*.
- Coninck, H., M. Loos, B. Metz, O. Davidson, and L. Meyer, 2005, *IPCC special report on carbon dioxide capture and storage*.
- Cook, P., 2014, *Geologically storing carbon: Learning from the Otway Project experience*: CSIRO PUBLISHING.
- Dance, F. M., 2019, *Geological characterisation of Australia's first carbon dioxide storage site*, University of Adelaide.
- Dance, T., M. Arnot, M. Bunch, R. Daniel, J. Ennis-King, A. Hortle, and M. Lawrence, 2012, *Geocharacterisation and static modelling of the Lower Paaratte Formation: CO2CRC Otway project stage 2: Technical Report RPT12-3481*. CO2CRC, Canberra, Australia.
- Dance, T., and S. Glubokovskikh, 2017, *Geological appraisal and static modelling for the CO2CRC Otway Project Stage 3: Incorporating outcomes from the CRC-3 well*: CO2CRC Limited
- Dance, T., T. LaForce, S. Glubokovskikh, J. Ennis-King, and R. Pevzner, 2019, *Illuminating the geology: Post-injection reservoir characterisation of the CO2CRC Otway site*: *International Journal of Greenhouse Gas Control*, **86**, 146-157.
- Davis, T. L., M. Landro, and M. Wilson, 2019, *Geophysics and Geosequestration*: Cambridge University Press.
- Eiken, O., 2019, *Twenty Years of Monitoring CO<sub>2</sub> Injection at Sleipner*, in Wilson, M., M. Landrø and T. L. Davis, eds., *Geophysics and Geosequestration*: Cambridge University Press, 209-234.
- Evans, B. J., 1997, *A handbook for seismic data acquisition in exploration*: Society of exploration geophysicists.
- Fagin, S., 1996, *The fault shadow problem: Its nature and elimination*: *The Leading Edge*, **15**, 1005-1013.
- Ghasemi, M., A. Ibrahim, and E. Gildin, 2014, *Reduced Order Modeling In Reservoir Simulation Using the Bilinear Approximation Techniques*: Presented at the SPE Latin America and Caribbean Petroleum Engineering Conference, Society of Petroleum Engineers.
- Glubokovskikh, S., R. Pevzner, T. Dance, E. Caspari, D. Popik, V. Shulakova, and B. Gurevich, 2016, *Seismic monitoring of CO<sub>2</sub> geosequestration*: CO2CRC



## References

---

- Otway case study using full 4D FDTD approach: *International Journal of Greenhouse Gas Control*, **49**, 201-216.
- Glubokovskikh, S., R. Pevzner, J. Gunning, T. Dance, V. Shulakova, D. Popik, S. Popik, M. Bagheri, and B. Gurevich, 2020, How well can time-lapse seismic characterize a small CO<sub>2</sub> leakage into a saline aquifer: CO<sub>2</sub>CRC Otway 2C experiment (Victoria, Australia): *International Journal of Greenhouse Gas Control*, **92**, 102854.
- Goodfellow, I., Y. Bengio, and A. Courville, 2016, *Deep Learning*: The MIT Press.
- Goodfellow, I., J. Pouget-Abadie, M. Mirza, B. Xu, D. Warde-Farley, S. Ozair, A. Courville, and Y. Bengio, 2014, Generative Adversarial Networks: Advances in Neural Information Processing Systems, **3**, 2672-2680.
- Hale, D., 2013, Methods to compute fault images, extract fault surfaces, and estimate fault throws from 3D seismic images: *GEOPHYSICS*, **78**, O33-O43.
- Hall, M. A., 1999, Correlation-based feature selection for machine learning: Doctor of Philosophy in f Computer Sciences, The University of Waikato.
- Hastie, T., R. Tibshirani, and J. Friedman, 2013, *The Elements of Statistical Learning: Data Mining, Inference, and Prediction*: Springer New York.
- Isaenkov, R., R. Pevzner, S. Glubokovskikh, S. Yavuz, A. Yurikov, K. Tertysnikov, B. Gurevich, J. Correa, T. Wood, and B. Freifeld, 2021, An automated system for continuous monitoring of CO<sub>2</sub> geosequestration using multi-well offset VSP with permanent seismic sources and receivers: Stage 3 of the CO<sub>2</sub>CRC Otway Project: *International Journal of Greenhouse Gas Control*, **108**, 103317.
- James, G., D. Witten, T. Hastie, and R. Tibshirani, 2013, *An introduction to statistical learning*: Springer.
- Jenkins, C., M. Bagheri, P. Barraclough, T. Dance, J. Ennis-King, B. Freifeld, S. Glubokovskikh, J. Gunning, T. LaForce, and S. Marshall, 2018, Fit for purpose monitoring-a progress report on the CO<sub>2</sub>CRC Otway Stage 3 project: Presented at the 14th Greenhouse Gas Control Technologies Conference Melbourne.
- Jenkins, C., P. Cook, J. Ennis-King, J. Undershultz, C. Boreham, T. Dance, P. de Caritat, D. Etheridge, B. Freifeld, and A. Hortle, 2011, Safe storage of CO<sub>2</sub> in a depleted gas field-the CO<sub>2</sub>CRC Otway Project: *Proc. Natl. Acad. Sci.*, in press.
- Jenkins, C., S. Marshall, T. Dance, J. Ennis-King, S. Glubokovskikh, B. Gurevich, T. La Force, L. Paterson, R. Pevzner, and E. Tenthorey, 2017, Validating subsurface monitoring as an alternative option to Surface M&V-the CO<sub>2</sub>CRC's Otway Stage 3 Injection: *Energy Procedia*, **114**, 3374-3384.
- Jiang, T., L. J. Pekot, L. Jin, W. D. Peck, C. D. Gorecki, and K. Worth, 2017, Numerical modeling of the Aquistore CO<sub>2</sub> storage project: *Energy Procedia*, **114**, 4886-4895.
- Khare, V., and A. Martinez, 2008, Estimation of sub-tuned reservoir thickness from amplitudes at different seismic bandwidths — a time-domain approach, SEG Technical Program Expanded Abstracts 2008, 2968-2972.

## References

---

- Krassay, A., D. Cathro, and D. Ryan, 2004, A regional tectonostratigraphic framework for the Otway Basin, *in* Boulton, P. J., D. R. Johns and S. C. Land, eds.: The Petroleum Exploration Society of Australia, Special Publication, 97-116.
- Krizhevsky, A., I. Sutskever, and G. E. Hinton, 2017, ImageNet Classification with Deep Convolutional Neural Networks: Communications of the ACM, **60**, 84-90.
- Lebedev, M., and V. Mikhaltsevitch, 2017, Testing acoustic response of partially CO<sub>2</sub> saturated reservoir rocks.: CO2CRC Limited.
- Lebedev, M., M. Pervukhina, V. Mikhaltsevitch, T. Dance, O. Bilenko, and B. Gurevich, 2013, An experimental study of acoustic responses on the injection of supercritical CO<sub>2</sub> into sandstones from the Otway Basin: GEOPHYSICS, **78**, D293-D306.
- Lumley, D., 2019, The Role of Geophysics in Carbon Capture and Storage, *in* Wilson, M., M. Landrø and T. L. Davis, eds., Geophysics and Geosequestration: Cambridge University Press, 11-53.
- Lumley, D. E., 2001, Time-lapse seismic reservoir monitoring: GEOPHYSICS, **66**, 50-53.
- Lüth, S., A. Ivanova, and T. Kempka, 2015, Conformity assessment of monitoring and simulation of CO<sub>2</sub> storage: A case study from the Ketzin pilot site: International Journal of Greenhouse Gas Control, **42**, 329-339.
- Ma, W., B. Jafarpour, and J. Qin, 2019, Dynamic characterization of geologic CO<sub>2</sub> storage aquifers from monitoring data with ensemble Kalman filter: International Journal of Greenhouse Gas Control, **81**, 199-215.
- Martinius, A. W., J. Hegner, I. Kaas, C. Bejarano, X. Mathieu, and R. Mjos, 2013, Geologic reservoir characterization and evaluation of the Petrocedeno field, early Miocene Oficina Formation, Orinoco heavy oil belt, Venezuela: AAPG Studies in Geology, **64**, 103-131.
- Mavko, G., T. Mukerji, and J. Dvorkin, 2020, The rock physics handbook: Cambridge university press.
- Metz, B., 2006, Carbon Dioxide Capture and Storage: IPCC Special Report. Summary for policymakers, a report of Working Group III of the IPCC; and, Technical summary, a report accepted by Working Group III of the IPCC but not approved in detail: World Meteorological Organization.
- Møller, M. F., 1993, A scaled conjugate gradient algorithm for fast supervised learning: Neural Networks, **6**, 525-533.
- Ogiesoba, O. C., W. A. Ambrose, and R. G. Loucks, 2018, Application of instantaneous-frequency attribute and gamma-ray wireline logs in the delineation of lithology in Serbin field, Southeast Texas: A case study: Interpretation, **6**, T1023-T1043.
- Oldenburg, C. M., S. Mukhopadhyay, and A. Cihan, 2016, On the use of Darcy's law and invasion-percolation approaches for modeling large-scale geologic carbon sequestration: Greenhouse Gases: Science and Technology, **6**, 19-33.

## References

---

- Oliver, D. S., A. C. Reynolds, and N. Liu, 2008, *Inverse Theory for Petroleum Reservoir Characterization and History Matching*: Cambridge University Press.
- Partridge, A. D., 2011, Palynological analysis of core and cuttings samples from the Paaratte Formation in the CRC No.2 well, Otway Basin: Biostrata Pty Ltd.
- Paterson, L., C. Boreham, M. Bunch, T. Dance, J. Ennis-King, B. Freifeld, R. Haese, C. Jenkins, T. LaForce, and M. Raab, 2013, Overview of the CO2CRC Otway residual saturation and dissolution test: *Energy Procedia*, **37**, 6140-6148.
- Pevzner, R., E. Caspari, B. Gurevich, T. Dance, and Y. Cinar, 2015, Feasibility of CO<sub>2</sub> plume detection using 4D seismic: CO2CRC Otway Project case study—Part 2: Detectability analysis: *GEOPHYSICS*, **80**, B105-B114.
- Pevzner, R., K. Tertyshnikov, E. Sidenko, and S. Yavuz, 2020a, Effects of Cable Deployment Method on DAS VSP Data Quality: Study at CO2CRC Otway in-situ Laboratory: Presented at the 82nd EAGE Annual Conference & Exhibition, European Association of Geoscientists & Engineers.
- Pevzner, R., M. Urosevic, E. Caspari, R. J. Galvin, M. Madadi, T. Dance, V. Shulakova, B. Gurevich, V. Tcheverda, and Y. Cinar, 2013, Feasibility of Time-lapse Seismic Methodology for Monitoring the Injection of Small Quantities of CO<sub>2</sub> into a Saline Formation, CO2CRC Otway Project: *Energy Procedia*, **37**, 4336-4343.
- Pevzner, R., M. Urosevic, D. Popik, V. Shulakova, K. Tertyshnikov, E. Caspari, J. Correa, T. Dance, A. Kepic, S. Glubokovskikh, S. Ziramov, B. Gurevich, R. Singh, M. Raab, M. Watson, T. Daley, M. Robertson, and B. Freifeld, 2017a, 4D surface seismic tracks small supercritical CO<sub>2</sub> injection into the subsurface: CO2CRC Otway Project: *International Journal of Greenhouse Gas Control*, **63**, 150-157.
- Pevzner, R., M. Urosevic, K. Tertyshnikov, H. AlNasser, E. Caspari, J. Correa, T. Daley, T. Dance, B. Freifeld, S. Glubokovskikh, A. Greenwood, A. Kepic, D. Popik, S. Popik, M. Raab, M. Robertson, V. Shulakova, R. Singh, M. Watson, S. Yavuz, S. Ziramov, and B. Gurevich, 2020b, Chapter 6.1 - Active surface and borehole seismic monitoring of a small supercritical CO<sub>2</sub> injection into the subsurface: experience from the CO2CRC Otway Project, *in* Kasahara, J., M. S. Zhdanov and H. Mikada, eds., *Active Geophysical Monitoring (Second Edition)*: Elsevier, 497-522.
- Pevzner, R., M. Urosevic, K. Tertyshnikov, B. Gurevich, V. Shulakova, S. Glubokovskikh, D. Popik, J. Correa, A. Kepic, and B. Freifeld, 2017b, Stage 2C of the CO2CRC Otway Project: Seismic monitoring operations and preliminary results: *Energy Procedia*, **114**, 3997-4007.
- Popik, S., R. Pevzner, K. Tertyshnikov, D. Popik, M. Urosevic, V. Shulakova, S. Glubokovskikh, and B. Gurevich, 2020, 4D surface seismic monitoring the evolution of a small CO<sub>2</sub> plume during and after injection: CO2CRC Otway Project study: *Exploration Geophysics*, 570-580.
- Poulton, M. M., 2001, *Computational neural networks for geophysical data processing*: Elsevier.

## References

---

- Roberts, A., 2001, Curvature attributes and their application to 3 D interpreted horizons: First break, **19**, 85-100.
- Russell, B. H., 1988, Introduction to seismic inversion methods: Society of Exploration Geophysicists.
- Schenck, C., and D. Fox, 2018, Spnets: Differentiable fluid dynamics for deep neural networks: arXiv preprint arXiv:1806.06094.
- Schlumberger, 2020, ECLIPSE Industry Reference Reservoir Simulator.
- Sharma, S., P. Cook, T. Berly, and M. Lees, 2009, The CO2CRC Otway Project: Overcoming challenges from planning to execution of Australia's first CCS project: Energy Procedia, **1**, 1965-1972.
- Simm, R., and M. Bacon, 2014, Seismic Amplitude: An Interpreter's Handbook: Cambridge University Press.
- Smith, T. M., C. H. Sondergeld, and C. S. Rai, 2003, Gassmann fluid substitutions: A tutorial: GEOPHYSICS, **68**, 430-440.
- Tenthorey, E., T. Dance, Y. Cinar, J. Ennis-King, and J. Strand, 2014, Fault modelling and geomechanical integrity associated with the CO2CRC Otway 2C injection experiment: International Journal of Greenhouse Gas Control, **30**, 72-85.
- The Math Works, I. M., 2006, Scaled conjugate gradient backpropagation: The Math Works, Inc. MATLAB.
- Underschultz, J., C. Boreham, T. Dance, L. Stalker, B. Freifeld, D. Kirste, and J. Ennis-King, 2011, CO<sub>2</sub> storage in a depleted gas field: An overview of the CO2CRC Otway Project and initial results: International Journal of Greenhouse Gas Control, **5**, 922-932.
- Walden, A. T., and R. E. White, 1998, Seismic wavelet estimation: A frequency domain solution to a geophysical noisy input-output problem: IEEE transactions on Geoscience and Remote Sensing, **36**, 287-297.
- White, D., 2019, Integrated Geophysical Characterization and Monitoring at the Aquistore CO<sub>2</sub> Storage Site, *in* Wilson, M., M. Landrø and T. L. Davis, eds., Geophysics and Geosequestration: Cambridge University Press, 257-279.
- Widess, M., 1973, How thin is a thin bed?: GEOPHYSICS, **38**, 1176-1180.
- Wildenborg, T., G. de Bruin, A. Kronimus, F. Neele, J. Wollenweber, and A. Chadwick, 2014, Transferring responsibility of CO<sub>2</sub> storage sites to the competent authority following site closure: Energy Procedia, **63**, 6705-6716.
- Woollands, M., and D. Wong, 2001, Petroleum Atlas of Victoria, Australia.
- Yoon, H., 2019, Physics-informed machine learning of permeability estimation and reactive transport in porous media: Sandia National Lab.(SNL-NM), Albuquerque, NM (United States).
- Zeng, H., 2010, Geologic significance of anomalous instantaneous frequency: GEOPHYSICS, **75**, P23-P30.

## References

---

Zhu, C., G. Zhang, P. Lu, L. Meng, and X. Ji, 2015, Benchmark modeling of the Sleipner CO<sub>2</sub> plume: Calibration to seismic data for the uppermost layer and model sensitivity analysis: *International Journal of Greenhouse Gas Control*, **43**, 233-246.

*Every reasonable effort has been made to acknowledge the owners of copyright material. I would be pleased to hear from any copyright owner who has been omitted or incorrectly acknowledged.*

# Appendix:

## Copyright Clearance

Permission is obtained to use the following figures:



1. **Figure 9.1** Location map of CO2CRC project (CO2CRC, 2020)

**Source:** CO2CRC website

**Copyright Clearance:**

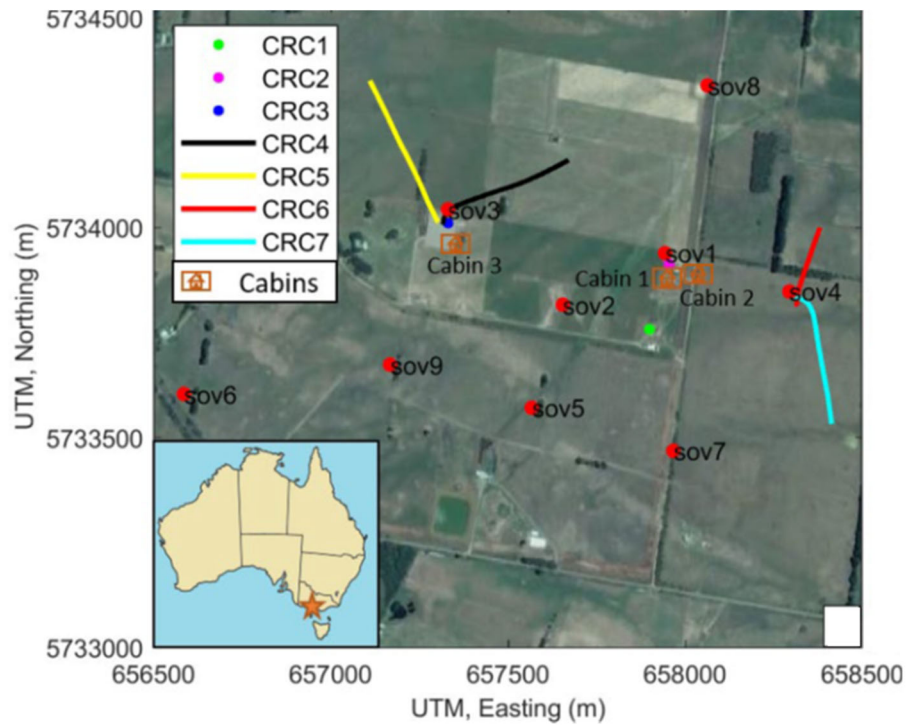


[Home](#) / [Resources](#) / [Images](#)

If you would like to use or reproduce the images on our website, please retain the 'CO2CRC' watermark or add the text 'Courtesy of CO2CRC Ltd' against the image.

## Appendix

2. **Figure 9.2** The SOV and the downhole DAS receivers intended to continuously monitor the Stage 3 injection modified after (Isaenkov et al., 2021).



**Source:** Isaenkov, R., R. Pevzner, S. Glubokovskikh, S. Yavuz, A. Yurikov, K. Tertysnikov, B. Gurevich, J. Correa, T. Wood, and B. Freifeld, 2021, An automated system for continuous monitoring of CO<sub>2</sub> geosequestration using multi-well offset VSP with permanent seismic sources and receivers: Stage 3 of the CO<sub>2</sub>CRC Otway Project: International Journal of Greenhouse Gas Control, **108**, 103317.

**Copyright Clearence:**

6/18/2021

RightsLink Printable License

## ELSEVIER LICENSE TERMS AND CONDITIONS

Jun 18, 2021

---

---

This Agreement between Mr. Mohammed Aldakheel ("You") and Elsevier ("Elsevier") consists of your license details and the terms and conditions provided by Elsevier and Copyright Clearance Center.

License Number	5091870609485
License date	Jun 18, 2021
Licensed Content Publisher	Elsevier
Licensed Content Publication	International Journal of Greenhouse Gas Control
Licensed Content Title	An automated system for continuous monitoring of CO2 geosequestration using multi-well offset VSP with permanent seismic sources and receivers: Stage 3 of the CO2CRC Otway Project
Licensed Content Author	Roman Isaenkov,Roman Pevzner,Stanislav Glubokovskikh,Sinem Yavuz,Alexey Yurikov,Konstantin Tertysnikov,Boris Gurevich,Julia Correa,Todd Wood,Barry Freifeld,Michael Mondanos,Stoyan Nikolov,Paul Barraclough
Licensed Content Date	Jun 1, 2021
Licensed Content Volume	108
Licensed Content Issue	n/a
Licensed Content Pages	1
Start Page	103317
End Page	0

<https://s100.copyright.com/AppDispatchServlet>

1/7



6/18/2021

RightsLink Printable License

Type of Use	reuse in a thesis/dissertation
Portion	figures/tables/illustrations
Number of figures/tables/illustrations	1
Format	both print and electronic
Are you the author of this Elsevier article?	No
Will you be translating?	No
Title	CO2 Storage Characterization Driven by Images of a Prior Injection: CO2CRC's Otway Project
Institution name	Curtin University
Expected presentation date	Sep 2021
Portions	figure 1 page 3
Requestor Location	Mr. Mohammed Aldakheel Dammam  Dammam, 31311 Saudi Arabia Attn: Mr. Mohammed Aldakheel
Publisher Tax ID	GB 494 6272 12
Total	0.00 USD
Terms and Conditions	

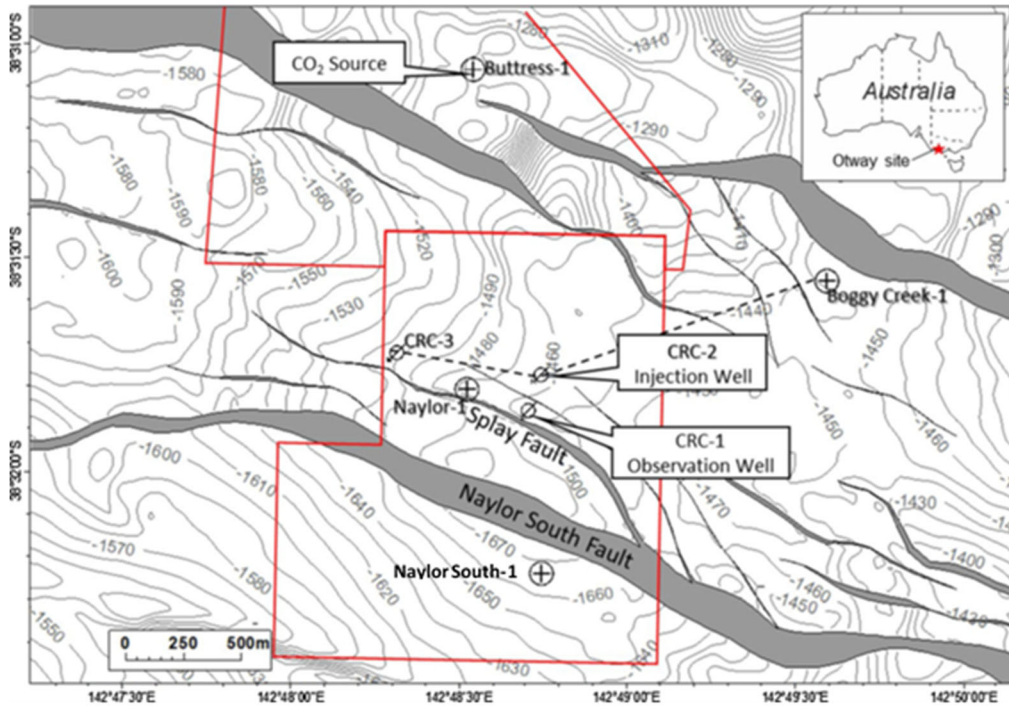
## INTRODUCTION

1. The publisher for this copyrighted material is Elsevier. By clicking "accept" in connection with completing this licensing transaction, you agree that the following terms and conditions

<https://s100.copyright.com/AppDispatchServlet>

2/7

3. **Figure 9.3** A depth map of the target reservoir ( PS1) with the regionally detected faults (Dance et al., 2019).



**Source:** Dance, T., T. LaForce, S. Glubokovskikh, J. Ennis-King, and R. Pevzner, 2019, Illuminating the geology: ---Greenhouse Gas Control, **86**, 146-157.

**Copyright Clearance:**

6/17/2021

RightsLink Printable License

## ELSEVIER LICENSE TERMS AND CONDITIONS

Jun 16, 2021

---

---

This Agreement between Mr. Mohammed Aldakheel ("You") and Elsevier ("Elsevier") consists of your license details and the terms and conditions provided by Elsevier and Copyright Clearance Center.

License Number	5090961261436
License date	Jun 16, 2021
Licensed Content Publisher	Elsevier
Licensed Content Publication	International Journal of Greenhouse Gas Control
Licensed Content Title	Illuminating the geology: Post-injection reservoir characterisation of the CO2CRC Otway site
Licensed Content Author	Tess Dance, Tara LaForce, Stanislav Glubokovskikh, Jonathan Ennis-King, Roman Pevzner
Licensed Content Date	Jul 1, 2019
Licensed Content Volume	86
Licensed Content Issue	n/a
Licensed Content Pages	12
Start Page	146
End Page	157
Type of Use	reuse in a thesis/dissertation

## Appendix

---

6/17/2021	RightsLink Printable License
Portion	figures/tables/illustrations
Number of figures/tables/illustrations	2
Format	both print and electronic
Are you the author of this Elsevier article?	No
Will you be translating?	No
Title	CO2 Storage Characterization Driven by Images of a Prior Injection: CO2CRC's Otway Project
Institution name	Curtin University
Expected presentation date	Sep 2021
Portions	figure 1 page 148 figure 10 page 155
Requestor Location	Mr. Mohammed Aldakheel Dammam  Dammam, 31311 Saudi Arabia Attn: Mr. Mohammed Aldakheel
Publisher Tax ID	GB 494 6272 12
Total	0.00 USD
Terms and Conditions	

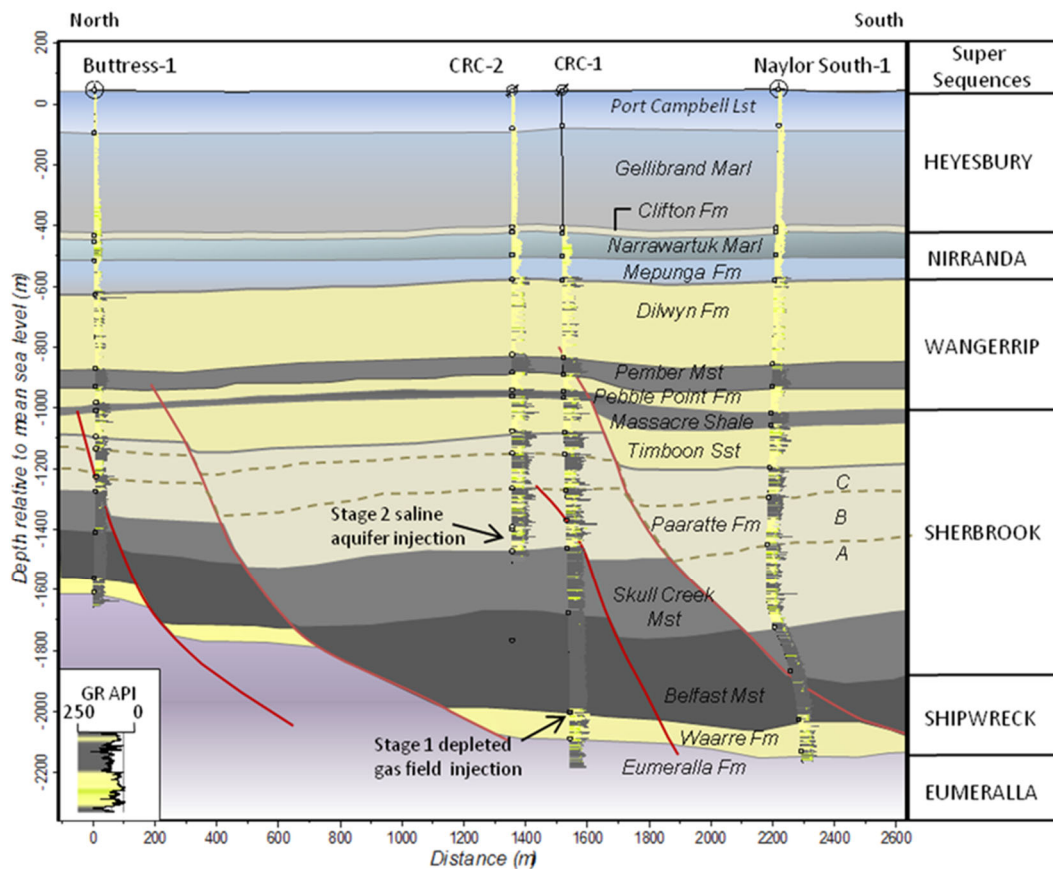
### INTRODUCTION

1. The publisher for this copyrighted material is Elsevier. By clicking "accept" in connection with completing this licensing transaction, you agree that the following terms and conditions apply to this transaction (along with the Billing and Payment terms and conditions established by Copyright Clearance Center, Inc. ("CCC"), at the time that you opened your Rightslink account and that are available at any time at <http://myaccount.copyright.com>).

### GENERAL TERMS

## Appendix

4. **Figure 9.4** A geological cross-section with the main wells in this project (Glubokovskikh et al., 2016).



**Source:** Glubokovskikh, S., R. Pevzner, T. Dance, E. Caspari, D. Popik, V. Shulakova, and B. Gurevich, 2016, Seismic monitoring of CO<sub>2</sub> geosequestration: CO<sub>2</sub>CRC Otway case study using full 4D FDTD approach: International Journal of Greenhouse Gas Control, **49**, 201-216.

**Copyright Clearance:**

6/18/2021

RightsLink Printable License

### ELSEVIER LICENSE TERMS AND CONDITIONS

Jun 18, 2021

---

---

This Agreement between Mr. Mohammed Aldakheel ("You") and Elsevier ("Elsevier") consists of your license details and the terms and conditions provided by Elsevier and Copyright Clearance Center.

License Number	5091870951533
License date	Jun 18, 2021
Licensed Content Publisher	Elsevier
Licensed Content Publication	International Journal of Greenhouse Gas Control
Licensed Content Title	Seismic monitoring of CO2 geosequestration: CO2CRC Otway case study using full 4D FDTD approach
Licensed Content Author	Stas Glubokovskikh,Roman Pevzner,Tess Dance,Eva Caspari,Dmitry Popik,Valeriya Shulakova,Boris Gurevich
Licensed Content Date	Jun 1, 2016
Licensed Content Volume	49
Licensed Content Issue	n/a
Licensed Content Pages	16
Start Page	201
End Page	216
Type of Use	reuse in a thesis/dissertation

<https://s100.copyright.com/AppDispatchServlet>

1/7

## Appendix

---

6/18/2021

RightsLink Printable License

Portion	figures/tables/illustrations
Number of figures/tables/illustrations	1
Format	both print and electronic
Are you the author of this Elsevier article?	No
Will you be translating?	No
Title	CO2 Storage Characterization Driven by Images of a Prior Injection: CO2CRC's Otway Project
Institution name	Curtin University
Expected presentation date	Sep 2021
Portions	figure 3 page 205
Requestor Location	Mr. Mohammed Aldakheel Dammam  Dammam, 31311 Saudi Arabia Attn: Mr. Mohammed Aldakheel
Publisher Tax ID	GB 494 6272 12
Total	0.00 USD

Terms and Conditions

### INTRODUCTION

1. The publisher for this copyrighted material is Elsevier. By clicking "accept" in connection with completing this licensing transaction, you agree that the following terms and conditions apply to this transaction (along with the Billing and Payment terms and conditions established by Copyright Clearance Center, Inc. ("CCC"), at the time that you opened your Rightslink account and that are available at <http://myaccount.copyright.com>).

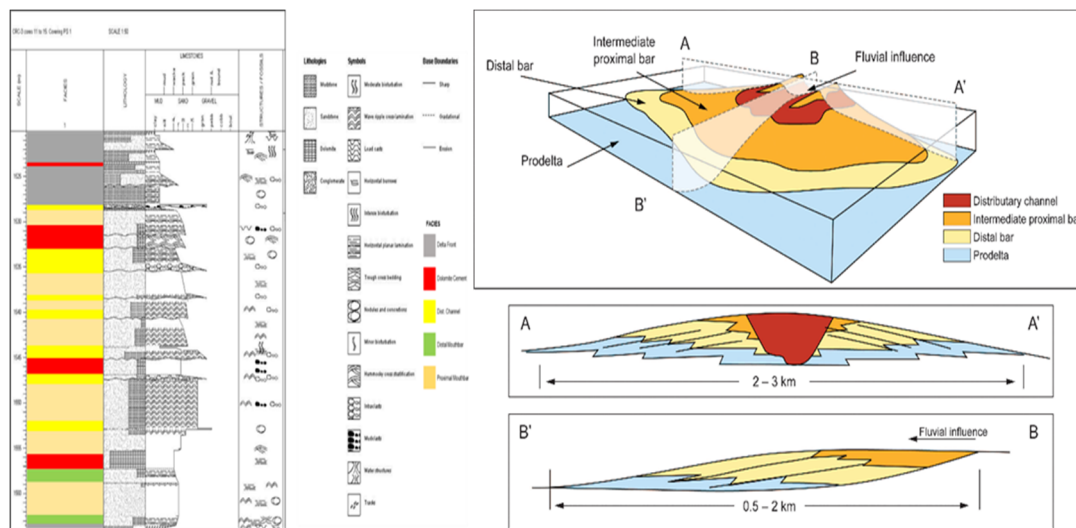
### GENERAL TERMS

<https://s100.copyright.com/AppDispatchServlet>

2/7

## Appendix

5. **Figure 9.5** Sedimentological discription of a core taken from the injection interval at CRC-3 and the facies associated with each interval (Dance, 2019) (to the left) and the geometry of a shallow marine/delta environment Longitudinal section (AA0) and a transverse section (BB0) (to the right) (Martinius et al., 2013)



**Sources:** 1. Dance, F. M., 2019, Geological characterisation of Australia’s first carbon dioxide storage site, University of Adelaide.

### Copyright Clearance:

From: "Dance, Tess (Energy, Kensington WA)" <[Tess.Dance@csiro.au](mailto:Tess.Dance@csiro.au)>  
 Date: 24 June 2021 at 09:05:36 GMT+3  
 To: "Gurevich, Boris (Curtin Uni) - Contact" <[B.Gurevich@curtin.edu.au](mailto:B.Gurevich@curtin.edu.au)>  
 Cc: Mohammed aldakheel <[aldakheel990@gmail.com](mailto:aldakheel990@gmail.com)>  
 Subject: RE: figure

Dear Boris,

The figure is in a paper under review with the Journal of Petroleum Geology... I'm sure it will be fine to publish it in Mohammad's Thesis. Just reference My Thesis if you like 😊

GEOLOGICAL CHARACTERISATION OF AUSTRALIA'S FIRST CARBON DIOXIDE STORAGE SITE

by

Francesca (Tess) Dance  
 The Australian School of Petroleum

This thesis is submitted in fulfilment of the requirements for the degree of Doctor of Philosophy in the Faculty of Engineering, Computer & Mathematical Sciences.  
 January, 2019

Dr Tess Dance

Senior Research Scientist | CSIRO  
[tess.dance@csiro.au](mailto:tess.dance@csiro.au) | 08 6436 8718

2. **Source** : Martinius, A. W., J. Hegner, I. Kaas, C. Bejarano, X. Mathieu, and R. Mjos, 2013, Geologic reservoir characterization and evaluation of the Petrocedeno field, early Miocene Oficina Formation, Orinoco heavy oil belt, Venezuela: AAPG Studies in Geology, **64**, 103–131.

**Copyright Clearance:** Fair usage policy



# BULLETIN SUBMISSION GUIDE

## Permission/Copyright

### Permissions

The author(s) is responsible for obtaining permission to use previously published illustrations. A letter of permission from the copyright holder must be submitted with the manuscript before editing begins.

For a form to assist you in getting permission to use illustrations or data from another publisher, download the [Permissions Template \(PDF\)](#).

### Copyright

AAPG obtains copyright of both print and digital/electronic ownership from most authors of articles and books published by AAPG. If any material requested was reprinted by AAPG with the permission of another publisher, it is the responsibility of those requesting permission to obtain permission from that original publisher.

Authors wishing to use AAPG copyrighted material within work being published by AAPG are not subject to fees nor do they need to seek permission from AAPG; however, it is the responsibility of authors to provide proper citation. Permission without a fee is granted to AAPG authors who wish to republish portions of their own work as long as AAPG copyright credit is given. For both instances please refer below to "Condition of Grant of Permission."

If you want to use a single figure, a brief paragraph, or a single table from an AAPG publication in a paper in another publication, AAPG considers this to be fair usage, and you need no formal permission. In that case, you should print a copy of this web page and present it to your publisher. You are, however, required to provide proper citation.

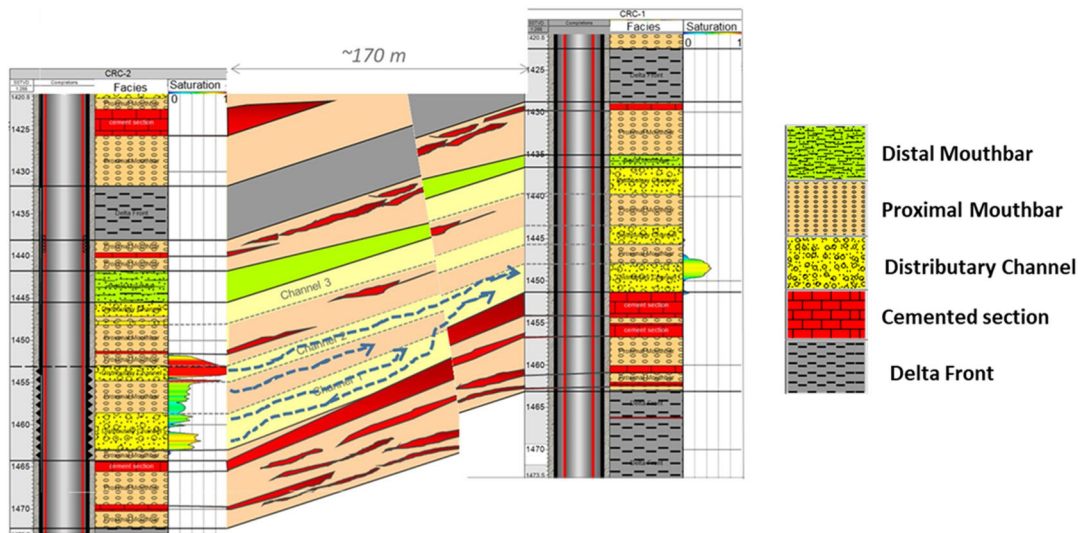
Authorization for additional copies of items copyrighted by AAPG in any form, hardcopy, digital/electronic scanning or other digital transformation into computer-readable and/or transmittable form, for personal or corporate use is granted provided the appropriate fee is paid directly to the Copyright Clearance Center, 222 Rosewood Drive, Danvers, Massachusetts 01923 / <http://www.copyright.com>. For circumstances occurring outside authorization of Copyright Clearance Center, contact AAPG Permissions at [permissions@aapg.org](mailto:permissions@aapg.org).

CONDITION OF GRANT OF PERMISSION: As a condition of the grant of permission contained under the single use only or multiple item usage, AAPG requires

1. a full citation in your bibliography for each AAPG publication from which a table or figure of text is taken;

## Appendix

6. **Figure 9.6** Cross-section of the target reservoir to demonstrate the CO<sub>2</sub> migration between the injection well and an observation well (Dance et al., 2019).



**Source:** Dance, T., T. LaForce, S. Glubokovskikh, J. Ennis-King, and R. Pevzner, 2019, Illuminating the geology: ---Greenhouse Gas Control, **86**, 146-157.

**Copyright Clearance:**

6/17/2021

RightsLink Printable License

## ELSEVIER LICENSE TERMS AND CONDITIONS

Jun 16, 2021

---

---

This Agreement between Mr. Mohammed Aldakheel ("You") and Elsevier ("Elsevier") consists of your license details and the terms and conditions provided by Elsevier and Copyright Clearance Center.

License Number	5090961261436
License date	Jun 16, 2021
Licensed Content Publisher	Elsevier
Licensed Content Publication	International Journal of Greenhouse Gas Control
Licensed Content Title	Illuminating the geology: Post-injection reservoir characterisation of the CO <sub>2</sub> CRC Otway site
Licensed Content Author	Tess Dance, Tara LaForce, Stanislav Glubokovskikh, Jonathan Ennis-King, Roman Pevzner
Licensed Content Date	Jul 1, 2019
Licensed Content Volume	86
Licensed Content Issue	n/a
Licensed Content Pages	12
Start Page	146
End Page	157
Type of Use	reuse in a thesis/dissertation

## Appendix

---

6/17/2021	RightsLink Printable License
Portion	figures/tables/illustrations
Number of figures/tables/illustrations	2
Format	both print and electronic
Are you the author of this Elsevier article?	No
Will you be translating?	No
Title	CO2 Storage Characterization Driven by Images of a Prior Injection: CO2CRC's Otway Project
Institution name	Curtin University
Expected presentation date	Sep 2021
Portions	figure 1 page 148 figure 10 page 155
Requestor Location	Mr. Mohammed Aldakheel Dammam
Publisher Tax ID	GB 494 6272 12
Total	0.00 USD
Terms and Conditions	

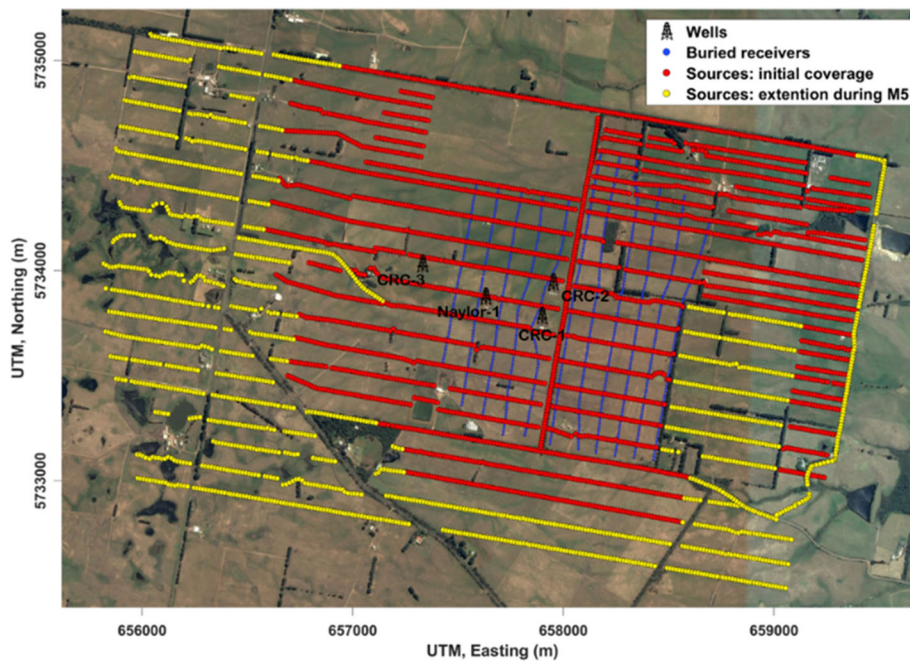
### INTRODUCTION

1. The publisher for this copyrighted material is Elsevier. By clicking "accept" in connection with completing this licensing transaction, you agree that the following terms and conditions apply to this transaction (along with the Billing and Payment terms and conditions established by Copyright Clearance Center, Inc. ("CCC"), at the time that you opened your Rightslink account and that are available at <http://myaccount.copyright.com>).

### GENERAL TERMS

## Appendix

7. **Figure 9.7** Acquisition geometry for the Stage 2C baseline survey and the Extended M5 survey (Popik et al., 2020).



**Source:** Popik, S., R. Pevzner, K. Tertyshnikov, D. Popik, M. Urosevic, V. Shulakova, S. Glubokovskikh, and B. Gurevich, 2020, 4D surface seismic monitoring the evolution of a small CO<sub>2</sub> plume during and after injection: CO<sub>2</sub>CRC Otway Project study: *Exploration Geophysics*, 570-580.

### Copyright Clearance:

4D surface seismic monitoring the evolution of a small CO<sub>2</sub> plume during and after injection: CO<sub>2</sub>CRC Otway Project study

Author: Sofya Popik, Roman Pevzner, et al  
Publication: *Exploration Geophysics*  
Publisher: Taylor & Francis  
Date: Sep 2, 2020  
*Rights managed by Taylor & Francis*

Thesis/Dissertation Reuse Request

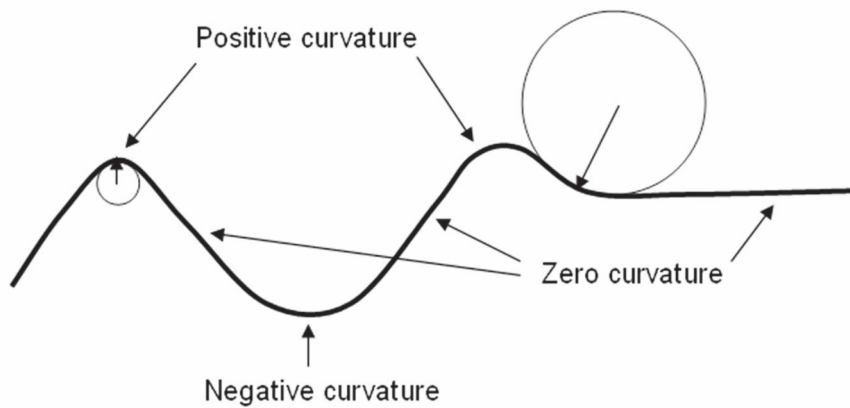
Taylor & Francis is pleased to offer reuses of its content for a thesis or dissertation free of charge contingent on resubmission of permission request if work is published.

[BACK](#) [CLOSE](#)

## Appendix

---

8. **Figure 9.8** Explanatory graph to show the different curvature values (Chopra and Marfurt, 2007).



**Source:** Chopra, S., and K. J. Marfurt, 2007, Seismic attributes for prospect identification and reservoir characterization: Society of Exploration Geophysicists.

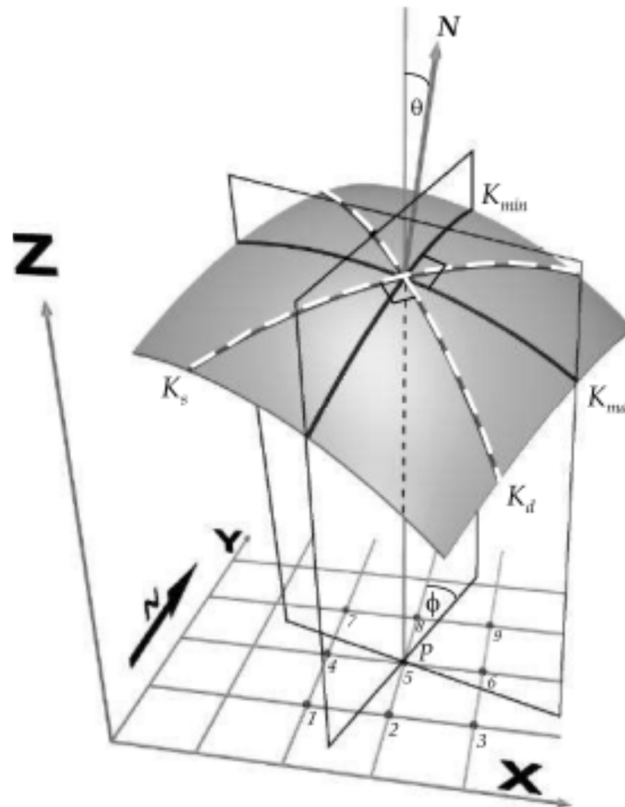
**Copyright Clearance:** fair usege applies

### Fair Use Permission

Use of up to three figures, a brief paragraph (up to 300 words), a single table, or the abstract from a single SEG publication is considered to be fair usage, and no formal permission is needed. If formal permission is required, please make your request as indicated below ("Usage Fees"). Fees may be assessed. We expect the SEG publication to be cited with appropriate credit, i.e., fully and prominently.

## Appendix

9. **Figure 9.9** 3D curvatures Calculation plane to highlight the maximum and minimum curvature ( $K_{\min}$  and  $K_{\max}$ ) (Roberts, 2001).



**Source:** Roberts, A., 2001, Curvature attributes and their application to 3 D interpreted horizons: First break, **19**, 85-100.

**Copyright Clearance:**

**From:** Publications EAGE <[publications@eage.org](mailto:publications@eage.org)>

**Date:** 21 June 2021 at 12:44:57 GMT+3

**To:** Mohammed Aldakheel <[mohammed.aldakheel@postgrad.curtin.edu.au](mailto:mohammed.aldakheel@postgrad.curtin.edu.au)>

**Subject:** Re: permission request to use a figure

Hi Mohammed

I hereby grant you copyright permission for the requested:

*Roberts, A., 2001, Curvature attributes and their application to 3 D interpreted horizons: First break, 19, 85-100.*

Please could you use this in the correct way.

Kind regards  
EAGE Publications

## Appendix

---

Part of the thesis was used to publish the following peer-reviewed article.

Aldakheel, M., R. Pevzner, B. Gurevich, and S. Glubokovskikh, 2021, Seismic Characterization of a CO<sub>2</sub> Storage Driven by Time-Lapse Images of a Prior Injection using Artificial Neural Network: Interpretation, **9**, 1-47.

According to copyright transfer agreement, I still retain the right to use all the material in my thesis.



**Interpretation Transfer of Copyright Agreement**

Agreement must be signed by lead or corresponding author and uploaded to ScholarOne Manuscripts before manuscript receives final acceptance.

**Article title:** Seismic Characterization of a CO2 Storage Driven by Time-Lapse Images of a Prior Injection using Artificial Neural Network

**Names of all authors:** Aldakheel, Mohammed; Glubokovskikh, Stanislav; Pevzner, Roman; Gurevich, Boris

For and in consideration of the potential publication of the article listed above (the "Work") by the Society of Exploration Geophysicists ("SEG") and the American Association of Petroleum Geologists ("AAPG"), I, the undersigned, as lead and/or corresponding author and/or rightsholders and acting on behalf of all authors and/or owners of copyright and other rights in the Work ("Authors"), hereby transfer, assign, and convey all right, title, interest, and worldwide copyright in the Work to SEG and AAPG, effective if and when the Work is accepted for publication, subject only to limitations expressed in this Transfer of Copyright (the "Agreement"). I warrant that I am authorized and empowered to represent all Authors with respect to the Agreement, which is executed jointly and severally by Authors if copyright transfer is from multiple individuals or entities. The Work includes the article and all material to be published within and with the article in any and all media, including but not limited to tables, figures, graphs, source code, movies, and other multimedia. Responses to discussions of the Work, errata, and other similar material directly related to the Work that may arise subsequent to publication also are considered part of the Work. In the event the Work incorporates copyrighted material of others, Authors warrant that all required permissions or releases have been secured. Authors agree to indemnify, defend, and hold SEG and AAPG, their directors, officers, employees, and agents harmless against any claims to the contrary.

Authors shall retain the following royalty-free rights:

1. All proprietary rights in the Work that are not transferred to SEG and AAPG in the Agreement, including the right to any patentable subject matter that may be contained in the Work
2. The right to reproduce and distribute part or all of the Work, including figures, drawings, tables, and abstracts of the Work, with proper attribution and copyright acknowledgment, in connection with Authors' teaching and technical collaborations
3. The right to make oral presentation of the same or similar information as that contained in the Work provided acknowledgment is made of SEG and AAPG joint copyright ownership and publication status
4. The right to post a final accepted version of the manuscript or the final SEG-formatted version on Authors' personal Web sites (not including social-network sites used for article sharing such as ResearchGate), employers' Web sites, or in institutional repositories operated and controlled exclusively by Authors' employers provided that (a) the *Interpretation*-accepted or *Interpretation*-published version is presented without modification unless modification is noted and fully described; (b) SEG and AAPG joint copyright notice and a full citation appear with the paper; (c) a live link to the version of record in the SEG Library using a Digital Object Identifier (DOI) permalink is provided; (d) the posting is noncommercial in nature, and the paper is made available to users without charge; (e) notice is provided that use is subject to SEG terms of use and conditions; and (f) a posting of the Work in an institutional repository neither carries nor is implied as carrying a license in conflict with SEG and AAPG joint copyright and terms of use
5. The right to prepare and hold copyright in derivative publications based on the Work provided that the derivative work is published subsequent to the official date of the Work's publication by SEG and AAPG and the Work is cited
6. The right to reuse all or part of the Work in a thesis or dissertation that the Author writes and is required to submit to satisfy criteria of degree-granting institutions, with full citation of the Work, its copyright status, and a DOI permalink to the version of record
7. The nonexclusive right, after publication by *Interpretation*, to republish and distribute print versions of the Work or excerpts therefrom without obtaining permission from SEG and AAPG, provided that (a) the paper is not republished in a journal, book, or collection of conference abstracts or proceedings; and (b) no fee is charged for the printed versions. Permission must be obtained from SEG for other republication of the Work.

SEG and AAPG may republish the Work or portions thereof in any future SEG or AAPG publication or compilation in any form and in any language, and SEG and AAPG retain exclusive right to license third parties to do the same.

This Agreement entitles Authors (or in the case of a Work Made for Hire, the employer) to retain all rights not transferred, assigned, or conveyed to SEG in the Agreement. Authors confirm that the Work has not been published previously elsewhere, nor is it under consideration by any other publisher, that the Work does not infringe any copyright or invade any right of privacy or publicity, and that Authors have the full power to enter into this Agreement and to make the grants contained herein. Authors warrant that they have complied and will comply with Ethical Guidelines for SEG Publications and that they agree to the provisions of these guidelines and all other SEG publications policies applicable to authors. This Agreement shall be binding on Authors' heirs, executors, administrators, and assigns, and shall be construed in accordance with the laws of the State of Oklahoma, United States of America.

IN WITNESS WHEREOF, I have executed this Transfer of Copyright on this 17th day of April, 2021.

**Mohammed Aldakheel**

Name of author (print or type)

**Mohammed Yousif M Aldakheel** Digitally signed by Mohammed Yousif M Aldakheel  
Date: 2021.04.17 19:15:23 +0800

Signature

**Curtin University**

Company for which work was performed (if applicable)

Authorized by/Title

**SIGN HERE IF U.S. GOVERNMENT EMPLOYED ALL  
AUTHORS WHEN WORK WAS PREPARED.**

I certify that the article named above was prepared solely by a U.S. government employee(s) as part of his/her (their) official duties and therefore legally cannot be copyrighted. Authors agree to all other terms of this agreement.

Name (print or type)

Date

Signature

**Paper title:** Seismic Characterization of a CO<sub>2</sub> Storage Driven by Time-Lapse Images of a Prior Injection using Artificial Neural Network

Aldakheel, M., R. Pevzner, B. Gurevich, and S. Glubokovskikh, 2021, Seismic Characterization of a CO<sub>2</sub> Storage Driven by Time-Lapse Images of a Prior Injection using Artificial Neural Network: Interpretation, **9**, 1-47

List of Authors:

Mohammed Aldakheel<sup>1,2</sup>

Roman Pevzner<sup>1</sup>




Boris Gurevich<sup>1</sup>

Stanislav Glubokovskikh<sup>3</sup>

1 Curtin University, Kent Street, Bentley, WA 6151, Australia

2 Saudi Arabian Oil Company, P.O. Box 10925, Dhahran 31311, Kingdom of Saudi Arabia

3 Lawrence Berkeley National Laboratory, 1 Cyclotron Road, MS 74R-316C, Berkeley, CA, USA, 94720

	Conception and Design	Acquisition and Data Method	Data Conditioning and Manipulation	Analysis and Statistical Method	Interpretation and Discussion	Final Approval
<b>Roman Pevzner</b>		√				√
Co Author 1 Acknowledgment: I acknowledge that these represent my contribution to the above research output  Signed:  13 July 2021						
<b>Boris Gurevich</b>					√	√
Co Author 2 Acknowledgment: I acknowledge that these represent my contribution to the above research output  Signed: <b>Boris Gurevich</b>  Digitally signed by Boris Gurevich Date: 2021.07.13 15:19:08 +08'00'						
<b>Stanislav Glubokovskikh</b>	√	√		√	√	√
Co Author 3 Acknowledgment: I acknowledge that these represent my contribution to the above research output  Signed:  12 July 2021						